POLITECNICO
MILANO 1863

SCUOLA DI INGEGNERIA INDUSTRIALE
E DELL'INFORMAZIONE

Executive Summary of the Thesis

Construction and Characterization of a Diode Pumped Yb-Er:glass Laser

Laurea Magistrale in Telecommunication Engineering - Ingegneria delle Telecomunicazioni

Author: Francesco Filippini

Advisor: Prof. Cesare Svelto

Academic year: 2021-2022

---

1. Reasons of Interest

Diode-pumped lasers have become increasingly popular because of their extremely desirable operating characteristics, such as single longitudinal and transverse mode operation, high efficiency, linear polarization, and enhanced stability. Moreover, the combination of this high performance and relatively low cost makes such lasers attractive for a variety of applications, including optical communications, fiber sensors, and spectroscopy [1]. In particular, phase-sensitive optical-time-domain reflectometry (ϕ-OTDR or PS-OTDR) is an effective way to detect vibrations and acoustic waves with high sensitivity, by interrogating coherent Rayleigh backscattering light from a sensing fiber.
A project in progress at the Optical and Electronic Measurements laboratory of the Department of Electronics, Information and Bioengineering of the Politecnico di Milano, in collaboration with the Bauman Moscow State Technical University involves the construction of a Yb-Er:glass laser to be used within an optical fiber measurement system based on phase-sensitive optical-time-domain reflectometry schemes. The aim of this work concentrates on the construction and the characterization of the Yb-Er:glass laser, trying to measure and investigate the stability of the laser through its main characteristics in terms of mode shape, maximum output power, cavity length, beam waist spot size and relative intensity noise (RIN).

2. Laser Design and Components

In designing the laser, a fiber-coupled diode laser, FBG stabilised, with peak power at a wavelength $\lambda_{\text{pump}} = 976$ nm and 300 mW maximum power was used as pump laser. The output fiber of the pump laser was connected to a collimator, with focal length $f_1 = 4.55$ mm, and then the beam was focused in the center of the active medium, thanks to a lens with focal length $f_2 = 75$ mm.
In general, a solid-state bulk laser is based on a bulk piece of doped crystal or glass as the active laser medium. Within a laser, the active laser medium is the material that emits coherent radiation and exhibits gain. The gain results from electronic or molecular transitions to a lower energy state from a higher energy state to which it had been earlier stimulated. In most cases, the gain medium is doped with rare-earth

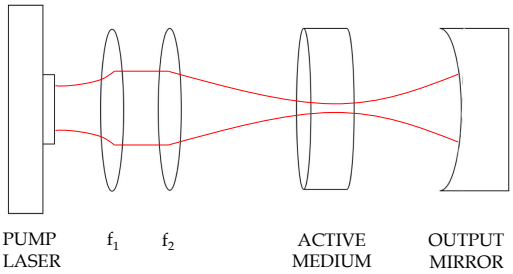

Figure 1: Laser structure scheme. The red line represents the propagation of the beam passing through the components.

ions: these ions replace a small percentage of other ions of similar size in the host medium. Concerning the thesis, the project refers to an Er:Yb phosphate glass where the Yb-to-Er energy transfer efficiency is higher than in other glasses due to the higher phonon energies properties of the glass.
For what concerns the resonant cavity, the active medium was already treated to have a reflective surface, forming a flat mirror with reflectivity $R_1 > 99.9\%$ in the laser wavelength range, from 1525 nm to 1565 nm, and $R_1 < 5\%$ in the pump wavelength range, from 970 nm to 980 nm. In the end a spherical mirror with reflectivity $R_2 > 99.9\%$ (within the range of wavelengths $1525 \div 1565$ nm) and $ROC = 50$ mm was added. The external face of the resonant cavity was treated as an anti-reflective surface at the laser wavelength, being $T_{2,ext} > 99.98$. Usually the cavity length of the resonator between the two mirrors R_1 and R_2 is not fixed, but it can be chosen when the laser is on in order to find the most suitable, depending on various factors or parameters such as the radius of curvature (ROC) of the second mirror, thermal lensing and stability of the cavity. A high-pass filter ($\lambda_{\text{cut}} = 1400$ nm) was positioned immediately after the cavity in order to filter out any pump light that might pass through the cavity and interfere with the measurements on the Yb-Er laser. The structure scheme of the Yb-Er:glass laser is showed in the Figure 1.

3. Optical Power Meters

All the measurements carried out in the laboratory needed an optical power meter, in order to measure the output power of our lasers (laser diode or solid state laser). Therefore, all the optical power meter heads available were characterized measuring and comparing their wavelength sensitivity. The power meter heads available was:

- LM-1 (Coherent) with thermal sensor;
- LM-2 VIS (Coherent) with silicon photodiode;
- S145C Integrating Sphere (Thorlabs) with InGaAs photodiode.

Indirect measurements on responsivity and wavelength sensitivity of the instruments were performed and it was confirmed what we expected. In particular, the LM-1 had wide wavelength range and flat response (i.e. mostly wavelength-independent), since the power meter exploits a thermal receiver inside the head that absorbs all the incoming optical energy and measures the difference between the temperature of the environment and that of the sensor, heated by the incoming and fully absorbed optical beam. The LM-2 VIS (Coherent) had wavelength range $400 \div 1064$ nm and its responsivity diagram followed the typical bell-shaped responsivity curve of silicon photodiodes with a peak around 950 nm. The S145C Integrating Sphere was the best power meter head available since it had better power resolution and range (1 nW resolution 1 µW up to 3 W), wider input aperture diameter and in general it was more advanced with respect to the other power meters. Furthermore, the resposivity diagram followed the typical bell-shaped responsivity curve of InGaAs photodiodes with wavelength range $800 \div 1700$ nm and peak around 1580 nm, hence this was the best power meter head to be used while performing measurements on the Yb-Er:glass laser, which has peak wavelength at 1550 nm.

4. Knife-Edge Technique and Pump Lasers Characteristics

In order to start the characterization of the laser we wanted to measure the spot size and the position of the beam waist. Since the beam waist of our laser was in the cavity, it was not technically accessible, hence we characterized it indirectly using the Knife-Edge technique. This is a simple low-cost design to measure the transverse spatial profile of a laser beam. In this method, a beam-block realized by a sharp edge made from an opaque material (such as a knife or razor-blade)

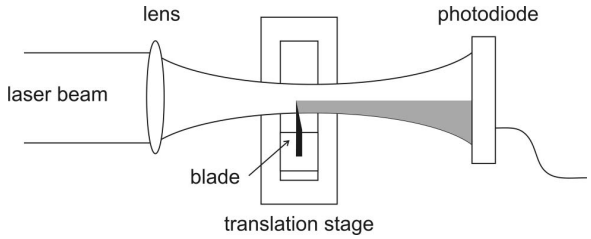

Figure 2: Simplified scheme of a spot size measurement using the Knife-Edge technique. The gray color area represents the shadow caused by the knife edge. From [2].

is line-scanned through the beam perpendicular to its optical axis while the transmitted power is monitored by a detector [3] (a scheme is showed in the Figure 2). Once represented the experimental data on a $P_{\text{out}} - y$ diagram, a Gaussian fitting curve is superimposed on the points (using functions available in Microsoft Excel) in such a way as to confirm the Gaussian shape of the beam or to reveal artifacts and bad measurements. At this stage, calculated a spot size $w(z)$, the procedure is repeated in other positions on the z axis in order to recreate the beam profile diverging from the waist on a $w(z) - z$ diagram. Using optics calculations it is possible to derive the spot size and the position of the beam waist (for this reason these are "indirect" measurements on the beam waist).
Before characterizing the solid state laser, it was important to use this technique on the He-Ne laser (used for the alignment of the laser components) as a training. The red beam of the He-Ne laser was well known, perfectly collimated and stable, hence it was possible to conduct an experiment placing a focusing lens and measuring the exact position and spot size of the beam waist created. In this way we understood how the Knife-Edge technique worked and we were able to confirm its validity.
Considering $z = 0$ mm the output point of the He-Ne laser tube, a lens with focal length equal to 150 mm was placed in $z = 100$ mm and the beam passing through it was focused in a certain position. Using optics calculations and thanks to a program called "Gaussian Beam", the beam profile was simulated and the position and the spot size of the beam waist was derived; the goal was to confirm these theoretical results with those estimated with the Knife-Edge technique. Having the properties of the beam waist, the angle of divergence (θ_{d}) and the Rayleigh distance (z_{R}) were calculated in order to find the position where the far-field started. Then, using the Knife-Edge technique, some spot sizes in far field was measured and a regression line was fitted and superimposed on the points, in order to derive the divergence angle, by which we calculated the spot size and the position of the beam waist created by the lens. Since the results was identical to those calculated before, we was ready to apply the technique to the solid state laser.
Before that, the characterization of the pump laser diodes available was crucial. Power-to-current characteristics were measured and compared to the one measured by the manifacturer (Thorlabs). We expected linear increasing of the output power with respect to the current, after the threshold. The control of the output power happened on the driver of the diode by moving screws clockwise and counterclockwise for increasing and decreasing the current, respectively. A 700 mW and a 300 mW laser diode were analyzed using both the LM-1 and the Integrating Sphere power meter, also changing the collimators connected to the output fibers. The experimental data were represented on a P_{pump} vs. I_{pump} diagram and they were fitted with a linear regression function passing through all the points. The angular coefficient of this line represented the slope efficiency ($\eta_{\text{slope}} = \Delta P/\Delta I$) of the diode laser considered, while, the point on the current axis in which the power became 1 mW was considered as the threshold current (I_{th}). The 300 mW laser diode and the 4.55 mm collimator were selected as pump for the Yb-Er:glass and in this case the characteristic presented $\eta_{\text{slope}} = 0.71$ W/A (a quite good value, compared to the typical one measured by Thorlabs) and $I_{\text{th}} = 48$ mA. The characteristics in all the cases were linear and followed the data measured by the manifacturer.

5. Yb-Er:glass solid state laser

Once aligned all the components (thanks to the He-Ne laser) the laser was on and it was possible to start the measurements on it. Firstly, the cavity of the resonator was studied. The cavity length could be calculated in a geometric way from the ABCD round trip matrix of the laser resonator [4]. A necessary condition for

the correct functioning of the laser is its stability. To this purpose it was necessary to calculate the maximum cavity length, L_C, for the laser to work in stability conditions. These calculations could be carried out by using the ABCD round trip matrix of the resonant cavity and imposing the stability condition, from which resulted $L_C < 50.34$ mm.
Done that, we carried out two measurements of the cavity length range (within which the laser operates) with two different pump currents (and hence at two different pump powers). The first with $I_{pump} = 243$ mA (that corresponds to $P_{pump} \cong 140$ mW), the second with $I_{pump} = 310.5$ mA (that corresponds to $P_{pump} \cong 180$ mW); the latter is represented in the Figure 3. These estimations were carried out measuring the output power of the laser (using the Integrating Sphere) while changing the position of the output mirror, rotating the z screw of its micrometric translator mounted on its mechanical holder. The measurement in

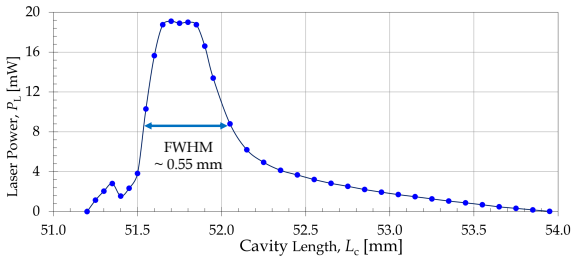

Figure 3: Output power vs. cavity length characteristic of the Yb-Er:glass laser. $I_{pump} = 310.5$ mA.

the case of higher pump power showed higher maximum output power and larger FWHM, together with larger cavity length range. Both the curves showed a peak where the power was at its maximum. On this peak and on the left side of the curve (where the cavity is shorter), observing the beam mode shape with a phosphor card, higher order transverse modes were present. On the right side of the curve, a clean TEM_{00} transverse mode could be seen with the phopshor card, remaining pure until the laser switch off, when the cavity became too long and the resonator was unstable. For this reason, in order to work with a perfect TEM_{00}, it was necessary to remain on the right side of the graph, with a cavity length approximately between 51.8 and 52.5 mm. This cavity length was larger than the theoretical maximum L_C previously calculated ($L_C < 50.34$ mm). Furthermore, the change in pump power modified a lot the output power vs. cavity length graphs, not only regarding the maximum power achievable, but also in relation to the cavity length stability range, that depends on the resonator properties. This was probably due to the effect of thermal lensing.
Thermal lensing is one of the most important effects that occur in propagating a high power laser beam in an absorbing medium. The heat generated by longitudinal laser pumping causes a mostly transverse (but also longitudinal) temperature gradient in a solid material. This can cause two main effects: non-uniform refractive index profile in the active medium and thermal expansion. Both the effects contribute to the bulging of the glass end faces and consequently a lenslike optical element is formed in it. The superposition of the two effects creates a focusing (positive) lens in the active material that generates a second laser beam waist inside the cavity. This modifies a lot the parameters of the resonator, because the new beam waist could be smaller or larger, closer to the first or to the second mirror and hence could change the divergence angle of the output beam. The fact that the cavity length was always larger than the theoretical maximum one was proof of the presence of the thermal lensing effect. This was also confirmed by simulations carried out with the program "reZonator", in which a resonator with $L_C > 50.34$ mm was stable only if a focusing positive lens was placed in the active medium (simulating the heating of the material).
Proceeding with the characterization of the Yb-Er laser, we knew that an important property of every laser is the variation of the output power with respect to the variation of pump power, together with its slope efficiency. We measured the output power vs. pump power of the Yb-Er:glass laser using four different cavity lengths, in order to see how the laser behaved changing one of its most important parameter. The tested cavity lengths were: 52 mm, 51.9 mm, 51.8 mm and 51.7 mm. The first three measurements showed linear characteristic (since with these cavity length, the mode was a clean TEM_{00}) with η_{slope} respectively equal to: 10.7 %, 15.7 % and 15.4 %. The last measurements presented a very strange characteristic: the output power

went up and down, while increasing the pump power, in a non-ideal way. This was due to the fact that with a too short cavity length, higher order modes were excited, presenting large spot sizes, even larger that the power meter sensor area, and resulting in imperfect measurements of the power.
At this stage we carried out measurements on the beam waist of the solid state laser, using the knife-Edge technique. As for the He-Ne laser, spot sizes in far field was measured and thanks to linear regression passing through the points, the angle of divergence was derived, allowing us to calculate the position and the spot size of the beam waist. The measurements was carried out in different laser conditions and the characteristics of the beam waist were always confirmed by simulations of the program "Gaussian Beam" and by calculations. In particular, we tried to detect the thermal lensing effect from the beam waist variations in the cases of low and high pump power (same cavity length). In the case of $I_{\text{pump}} = 100$ mA and $P_{\text{out}} = 2$ mW the beam waist was on the input mirror R_1 and its spot size was equal to 51.1 µm, while in the case of $I_{\text{pump}} = 349$ mA and $P_{\text{out}} = 18.51$ mW the beam waist was 1 mm inside the cavity and its spot size was equal to 49.6 µm. The beam waist became smaller and shifted its position inside the cavity while increasing the pump power, proving the presence of thermal lensing effect. Actually, in order to show more visible effects, the 700 mW pump laser should be used, providing much more power and heating up significantly the active medium.

6. RIN

The characterization of the solid state laser ended with the Relative Intensity Noise (RIN) measurements. The RIN (dB/Hz) describes the time instability in the power level of a laser and it is produced by cavity vibration, fluctuations in the laser gain medium, or simply by transferred intensity noise from the pump source. RIN typically peaks at the relaxation oscillations (RO) frequency (f_{RO}) of the laser and then falls off at higher frequencies where it becomes shot-noise limited. Typical values of relaxation oscillations frequency for solid state lasers are in the range from a few kHz to a few MHz. The relaxation oscillations phenomenon results from the interplay between the population inversion and the intracavity laser intensity. It is present in any class-B laser, i.e. where the population inversion lifetime is longer than the cavity photon lifetime [5], as in the Yb-Er:glass laser.

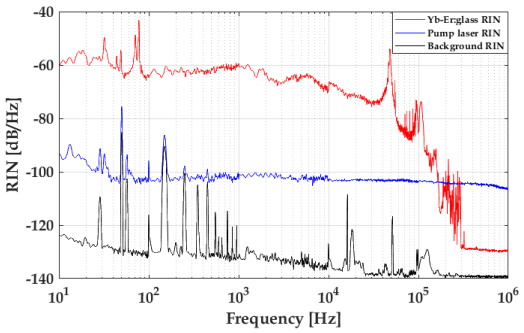

Figure 4: RIN measurements on Yb-Er:glass laser (red), 300 mW pump laser (blue) and background (black). DC block filter compensated.

The RIN measurements were carried out using an electrical spectrum analyzer (ESA) controlled with matlab and connected to a photoreceiver (and a digital oscilloscope). A DC block connected to the input of the ESA was necessary for correct measurements but this element acted as a filter with cutoff frequency equal to 100 Hz (measured in the laboratory). Since the low frequencies were important for our purposes, we tried to compensate the filtering effect thanks to the analysis of the DC block using known input signals (a Function Waveform Generator was used to generate a white noise signal as input of the ESA).
The bandwidth of the RIN measurements was modified in the matlab code and it was divided in decades from 10^1 Hz to 10^6 Hz (601 points equally spaced in frequency for every decade). In this way it was possible to plot the RIN in dB/Hz with respect to frequency, represented in logarithmic scale. Also the number of averages performed by the ESA and the resolution bandwidths for every frequency decade were modified according to our purposes.
Both the RIN of the Yb-Er:glass laser and of the pump laser diode were measured, together with the background (measured by switching off the laser and leaving the photoreceiver on and connected to the ESA), taken into account as a reference (Figure 4). The measurement on the pump laser was carried out placing two Neutral Density filters in series, so as to attenuate the

power entering in the photoreceiver. The pump current was equal to $I_{\text{pump}} = 243$ mA and the average voltage measured with the oscilloscope was equal to 635 mV. From 10 Hz to 10 kHz we performed 50 averages and from 10 kHz to 1 MHz we performed 400 averages. The compensated spectrum (Figure 4) of the pump laser appeared flat and sufficiently good, there were peaks at 50 Hz and 150 Hz but it was clear that they were generated by the background noise of the instruments and/or of the environment. The measurement on the Yb-Er:glass laser needed only one ND filter because the beam was diverging and, at a reasonable distance, the power was distributed on a large area with respect to the one of the photodiode, having lower power entering the photoreceiver than in the case of the pump laser. The average voltage was equal to 384 mV, while the pump current and the averages performed was the same as for the pump laser. The compensated spectrum (Figure 4) presents new peaks at 70 Hz and 78 Hz with very high RIN values that are definitely non-ideal (they were not generated by the background noise). Increasing the frequency, the RIN fluctuates around $\cong -70$ dB/Hz until the relaxation oscillations peak at 48 kHz, where the maximum level is about -55 dB/Hz, a quite high value but lower than the peaks at low frequency. After this peak, the spectrum starts to fall off with slope $\cong -60$ dB/Hz per decade until -130 dB/Hz, as expected, but showing unusual fluctuations and peaks. In general, the compensated spectrum of the Yb-Er laser appeared not so good and it was definitely necessary a solution for the RIN reduction and the relaxation oscillations peak suppression.

7. Conclusions

In this work, the construction and the characterization of a Yb-Er:glass laser are exposed. Firstly, we studied every single component of the laser structure together with the power meters used for the laser measurements. The responsivity of the power meters was measured and presented. Then, experimental estimations on the pump laser diodes available was made, in order to find the best and most stable one. Once investigated and selected the pump laser, we proceeded to the construction of the solid state laser, with the precise alignment of every component thanks to a He-Ne laser. The Yb-Er:glass laser was switched on and its output power was maximized thanks to micrometric translations of its most important components. At this point we estimated the stability of the laser varying its cavity length and pump power, provided by the laser diode. The Knife-Edge technique was presented and used for the spot size of the beam waist measurements, from which we revealed a thermal lensing effect in the active material. In the end, the Relative Intensity Noise of the pump laser diode and the solid state laser was measured, comparing the results and discussing the spectra obtained. A future development for a better stability of the Yb-Er:glass laser could be a monolithic structure, in which the whole laser resonator consists only of some "solid" pieces of crystal or glass without air gaps between optical elements. In this way, the stability could improve together with the peak power and the threshold pump power (that could decrease significantly).

References

[1] T V Choban, A A Zhirnov, A O Chernutsky, K V Stepanov, A B Pniov, G Galzerano, V E Karasik, and C Svelto. ϕ-OTDR based on tunable yb-er:phosphate-glass laser. *Journal of Physics: Conference Series*, 1410(1), dec 2019.

[2] Marcos Araújo, Rubens Silva, Emerson Lima, Daniel Pereira, and Paulo De Oliveira. Measurement of gaussian laser beam radius using the knife-edge technique: Improvement on data analysis. *Applied optics*, 48: 393–6, 02 2009.

[3] Orlov, Sergej, Huber, Christian, Marchenko, Pavel, Banzer, Peter, Leuchs, and Gerd. Toward a corrected knife-edge-based reconstruction of tightly focused higher order beams. *Frontiers in Physics*, 8, 2020.

[4] Orazio Svelto. *Principles of lasers*. Springer Nature, 5th edition, 2010.

[5] D. McCumber. Intensity fluctuations in the output of laser oscillators. *IEEE Journal of Quantum Electronics*, 2(8):219–221, 1966.

POLITECNICO
MILANO 1863

SCUOLA DI INGEGNERIA INDUSTRIALE
E DELL'INFORMAZIONE

Construction and Characterization of a Diode Pumped Yb-Er:glass Laser

Tesi di Laurea Magistrale in
Telecommunications Engineering

Author: **Francesco Filippini**

Student ID: 941094
Advisor: Prof. Cesare Svelto
Academic Year: 2021-22

Contents

List of Figures

Abstract

Diode-pumped lasers have become increasingly popular and attractive for a variety of applications, including optical communications, fiber sensors, and spectroscopy. In particular, Phase-sensitive Optical Time Domain Reflectometers (ϕ-OTDR) are widely used in remote monitoring systems and the Yb-Er:glass solid-state laser presents a great interest for such systems, as this laser has very good short-term wavelength stability and possibility of wavelength tuning.

In this work, the construction and the characterization of an Yb-Er:glass laser are exposed. The single components of the laser structure together with the instruments available for the various measurements were studied. The characteristics of the pump laser diodes were investigated and then all the elements were accurately aligned in order to switch on the solid state laser. The cavity length, the output power vs. pump power characteristics and the RIN were measured and illustrated, showing the main problems and the possible future developments for the Yb-Er:glass laser.

Keywords: Yb-Er:glass Laser, Optical Measurements, Knife-Edge technique, Thermal Lensing Effect, RIN.

Sommario

I laser pompati a diodi sono diventati sempre più popolari e attraenti per una varietà di applicazioni, comprese le comunicazioni ottiche, i sensori a fibra e la spettroscopia. In particolare, i Phase-sensitive Optical Time Domain Reflectometers (ϕ-OTDR) sono ampiamente utilizzati nei sistemi di monitoraggio remoto e il laser a stato solido Yb-Er:glass presenta un grande interesse in questo campo perchè ha un'ottima stabilità a breve termine della lunghezza d'onda e la possibilità di modificare la lunghezza d'onda. In questo lavoro sono esposte la costruzione e la caratterizzazione di un laser Yb-Er:glass. Sono stati studiati singoli componenti della struttura del laser insieme agli strumenti disponibili per le varie misure. Sono state investigate le caratteritiche dei diodi del laser di pompa e in seguito tutti gli elementi sono stati accuratamente allineati per l'accensione del laser a stato solido. Sono state misurate e illustrate la lunghezza di cavità, le caratteristiche potenza di uscita vs. potenza di pompa e il RIN, mostrando i principali problemi e i possibili sviluppi futuri del laser Yb-Er:glass.

Parole chiave: Yb-Er:glass laser, Misure Ottiche, Tecnica Knife-Edge, Effetto di Lente Termica, RIN.

Introduction

Diode-pumped Er,Yb:glass lasers operating at a 1550 nm wavelength have generated great interest for years and are used in various applications, such as Optical Fiber Sensors (OFS), spectroscopy, interferometers and ϕ-OTDR. In particular, phase-sensitive optical-time-domain reflectometry ($\boldsymbol{\phi}$-OTDR or PS-OTDR) is an effective way to detect vibrations and acoustic waves with high sensitivity, by interrogating coherent Rayleigh backscattering light from a sensing fiber.

A project in progress at the Optical and Electronic Measurements laboratory of the Department of Electronics, Information and Bioengineering of the Politecnico di Milano, in collaboration with the Bauman Moscow State Technical University involves the construction of a Yb-Er:glass laser to be used within an optical fiber measurement system based on phase-sensitive optical-time-domain reflectometry schemes.

The scope of this thesis is to develop a single-mode, diode-pumped Yb-Er:glass laser at $\lambda = 1550$ nm and to make measurements on it with the aim of being able to create a high-performance laser that has all the characteristics, in particular of spectral purity and amplitude noise, suitable for making it a valid source for PS-OTDR.

This work is divided into 5 chapters, which are organized as follows:

- **Chapter 1** presents the most general and theoretical concepts of the Yb-Er:glass LASER project. Then the design of the resonant cavity and the choice of the individual elements for the LASER construction is exposed.
- **Chapter 2** presents various types of power meters used in the measurements and illustrates comparisons between them. In particular, measurements are made on the responsivity of the instruments and on the output optical power of the diode laser.
- **Chapter 3** presents the knife-edge technique used for the spot size estimation of Gaussian beams. Using this technique, measurements on the beam of a He-Ne laser are illustrated.
- **Chapter 4** presents measurements made on the Yb-Er laser focusing particularly on beam waist estimation.
- **Chapter 5** presents Relative Intensity Noise measurements on both the pump and the solid state lasers. At the end, future developments are exposed.

1 | Basics of the Yb-Er:Glass Laser

In this chapter the most general and theoretical concepts of the Yb-Er:glass LASER project are presented. The main elements of the set-up are illustrated and depicted. Eventually the alignment process using a He-Ne laser is discussed.

This chapter is divided into the following sections:

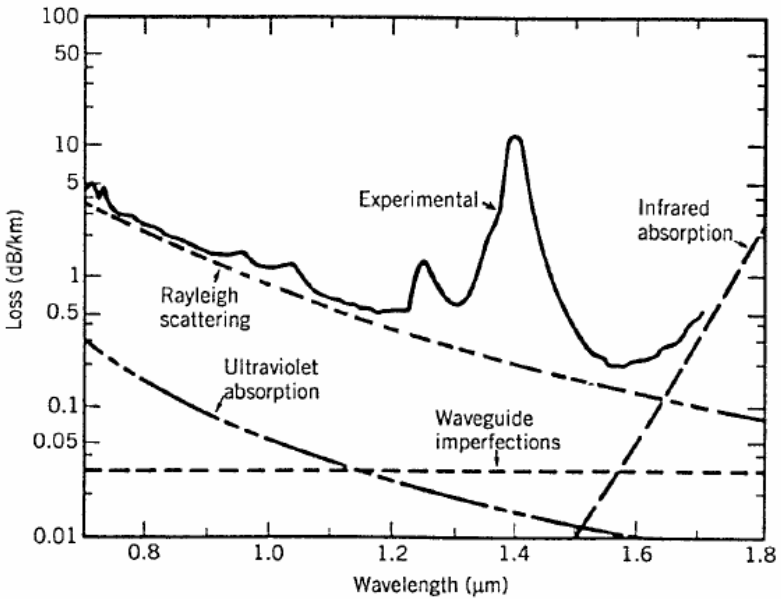

Figure 1.1: Typical attenuation spectrum for silica glass fiber.

1.1. Reasons of Interest

This work aims to realise and study a diode-pumped Yb-Er: glass laser, which works in the single fundamental mode TEM_{00} around the emission wavelength range of 1550 nm. This wavelength range is in the third optical transmission window of optical fibers, where the attenuation of the fiber is very low, $\alpha \leq 2$ dB/km (Figure 1.1), and in the Erbium-Doped Fiber Amplifier (EDFA) the minimum amplitude noise is reached.

1.1.1. Yb-Er Laser as a Source of Φ-OTDR

The output beam of an Yb-Er: glass laser is often said "eye-safe" because light in third window wavelength range is strongly absorbed in the eye's cornea and therefore cannot reach the retina, which is more sensitive and can be damaged [8]. For this, the Yb-Er laser has sev-

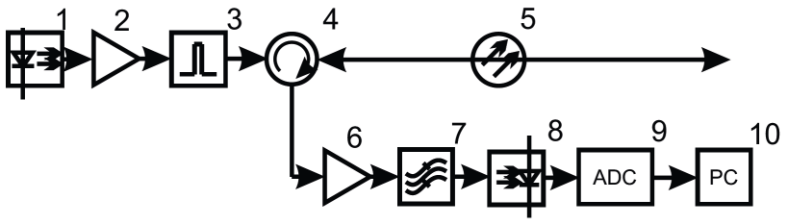

Figure 1.2: ϕ scheme: 1 – laser source, 2 – EDFA-booster, 3 – optical modulator, 4 – optical circulator, 5 – sensing fiber, 6 – EDFA-preamplifier, 7 – optical filter, 8 – photoreceiver, 9 – ADC, 10 – personal computer. From [1].

eral uses such as in telecommunication systems, long-distance telemetry and ranging, spectrometry, microsurgery and ϕ-OTDR. Fiber-optic distributed acoustic sensing (DAS) is based on the ϕ-OTDR with phase demodulation and has been extensively studied and widely used in intrusion detection, borehole seismic acquisition, structure health monitoring, etc., in recent years, with superior advantages such as long sensing range, fast response speed, wide sensing bandwidth, low operation cost and long service lifetime. Comparing to other lasers, the Yb-Er: glass laser has high performance in terms of output power, slope efficiency, single-mode selection, narrow-line-width, tunability, frequency stability, and low amplitude noise. Moreover, this laser has potentials for a low-cost fabrication. On the other hand, the limits imposed by this type of laser lie in the thermal stress and thermal lensing effects on the active medium.

A project in progress at the Optical and Electronic Measurements laboratory of the Department of Electronics, Information and Bioengineering of the Politecnico di Milano, in collaboration with the Bauman Moscow State Technical University involves the construction of a Yb-Er: glass

LASER to be used within an optical fiber measurement system based on phase-sensitive optical-time-domain reflectometry (ϕ-OTDR) schemes (Figure 1.2). The realised laser acts as the source of the ϕ-OTDR and has to meet certain performances:

- coherence length large enough so that coherent sum is obtained in amplitude instead of power (as in commercial OTDRs)[9];
- frequency stability for reflectrogram stability;
- Relative Intensity Noise (RIN) less than -120 dB/Hz below 1 MHz, and less than -150 dB/Hz above 10 MHz;
- output power greater than 10 mW, considering single mode LASER TEM_{00}.

1.2. Laser Design and Components

In designing the laser, a fiber-coupled diode laser is used as pump (in order to solve the typical problems of semiconductor lasers whereby the output beam is strongly astigmatic making it circularly symmetrical), FBG stabilised, with peak power at a wavelength $\lambda_{\text{pump}} = 976$ nm.

The laser beam coming out from the fiber of the diode is perfectly circular and diffraction limited, but it is strongly divergent because of the micrometric diameter of the fiber itself, so it must be collimated and focused. Since it is necessary to collimate the beam within a very small distance (in order to lose as little power as possible at the pump stage) and for easier mounting, a collimator with a very short focal length and

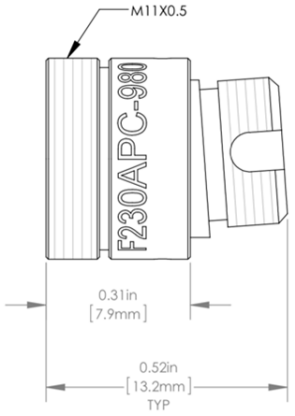

(a)

SPECIFICATIONS

DESIGN WAVELENGTH	980nm
DESIGN MFD	5.8 µm
OUTPUT $1/e^2$ BEAM DIAMETER	0.98 mm
FULL ANGLE BEAM DIVERGENCE	$0.073^{\circ}\ ^{+0.01}_{-0.00}$
AR COATING	Ravg<0.5% FROM 650-1050nm

(b)

Figure 1.3: a) Diameter and length of the collimator. b) Specifications of the focal lens $f_1 = 4.55$ mm. Both from Throlabs datasheets.

with a special mounting for the head of the fiber is used. For the thesis project, the collimator used is built by Thorlabs and the model is F230APC-980 with a focal length $f_1 = 4.55$ mm. The final part of the model name stands for the peak design wavelength at 980 nm and the numerical aperture NA is $0,49$. Its technical characteristics are shown in Figure 1.3.

In general, the collimators must be at the focal length from the beam waist (Figure 1.4 and Figure 1.5) in order to collimate the beam properly; if the beam waist was not at the focal length from the collimator, the beam coming out would present a full angle of divergence greater than 0.073, making collimation useless. Then, for providing a beam focusing after the collimator f_1, a second spherical lens is wanted. The second lens has a long focal length f_2, and, together with the first lens, the magnification is reached. "Magnification" means how many times the pump laser beam is enlarged with respect to its original dimension, so

how large is the beam waist compared to the original fiber spot size (Equation 1.1. Considering the ratio between the two focal lengths, we find the telescopic magnification M according to:

$$M = \frac{f_2}{f_1}\,. \tag{1.1}$$

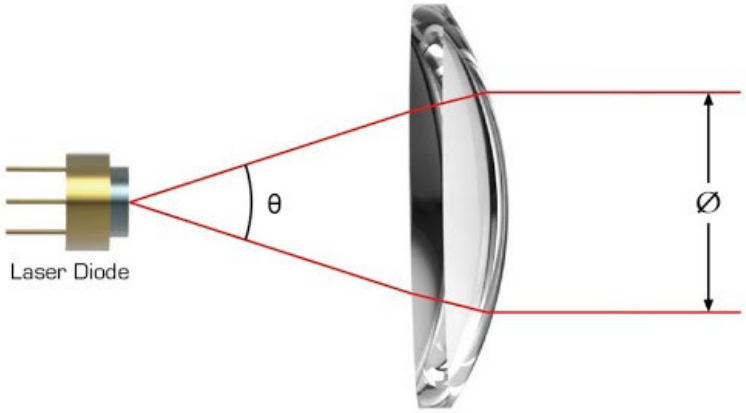

Figure 1.4: Schematic representation of the collimating lens f_1 on a laser beam.

Since the focal length of the first lens, in this case, is fixed ($f_1 = 4.55$ mm) it is possible to change the focal length of the second lens because it is easier and cheaper and so the telescopic magnification can be modified. The objective is to have an M-factor of approximately 15 (achievable with $f_2 = 75$ mm), this value allows to have a spot size not too small, which could break the active medium due to excessive concentration of power in a small area, nor too large because it could lead to a transverse multi-mode beam, as well as significantly increasing the value of the pump power required to obtain the LASER threshold condition.

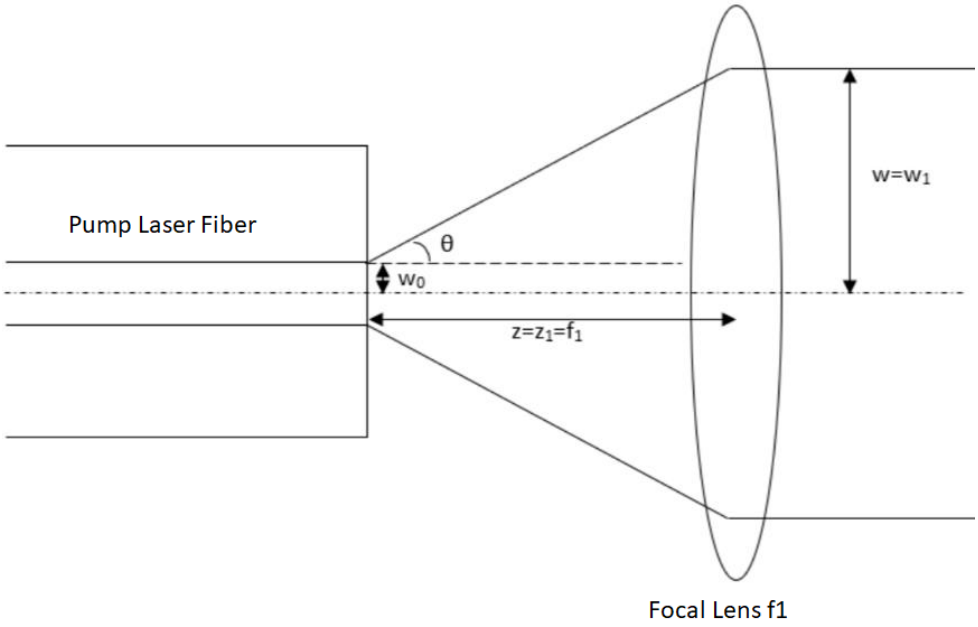

Figure 1.5: Collimation scheme of the pump laser beam. w_0 is the beam waist spot size, θ_d is the divergence angle, $z = z_1 = f_1$ is the distance at which the lens is placed, w_1 is the spot size of the collimated beam.

1.2.1. Resonant Cavity

The active medium made of phosphate glass disk of 1 mm thickness, doped with erbium ions (to achieve lasing action at around 1550 nm) and ytterbium ions (to increase the pump absorption) is placed after the two lenses. The Yb,Er: co-doped phosphate glass has many peculiarities such as wide absorption band, long fluorescence lifetime, high slope efficiency, and high optical quality. The active medium is already treated to have a reflective surface, forming a flat mirror with reflectivity $R_1 > 99.9\%$ in the laser wavelength range from 1525 nm to 1565 nm and $R_1 < 5\%$ in the pump wavelength range from 970 nm to 980 nm. In the end a spherical mirror with reflectivity $R_2 > 99.9\%$ (within the range of

wavelengths $1525 \div 1565$ nm) is added. The external face of the resonant cavity is treated as an anti-reflective surface at the laser wavelength, being $T_{2,ext} > 99.98$. Usually the cavity length of the resonator between the two mirrors R_1 and R_2 is not fixed, but it can be chosen when the laser is on in order to find the most suitable, depending on various factors or parameters such as the radius of curvature (ROC) of the second mirror, thermal lensing and stability of the cavity, as it will be described in Chapter 4. Normally, it is better to have a short resonator cavity length (< 55 mm) because the device is more compact and simpler.

A high-pass filter ($\lambda_{\text{cut}} = 1400$ nm) is positioned immediately after the cavity in order to filter out any pump light that might pass through the cavity and interfere with the measurements on the Yb-Er laser.

In the Figure 1.6 a laser components scheme is depicted. The red line represents the beam exiting the laser diode fiber and passing through the resonant cavity.

1.2.2. Pump Diodes and Optical Fiber Specifications

In the beginning, the laser must be connected to a driver for starting lasing. The driver is called DFU and the model used for this project is DFU043 (Figure 1.7). The driver controls the temperature, to avoid overheating of the driver itself, and the output power. The temperature is indicated as the voltage difference between the TMP and GND pins. The voltage difference is equal to 1250 mV, it means that the working

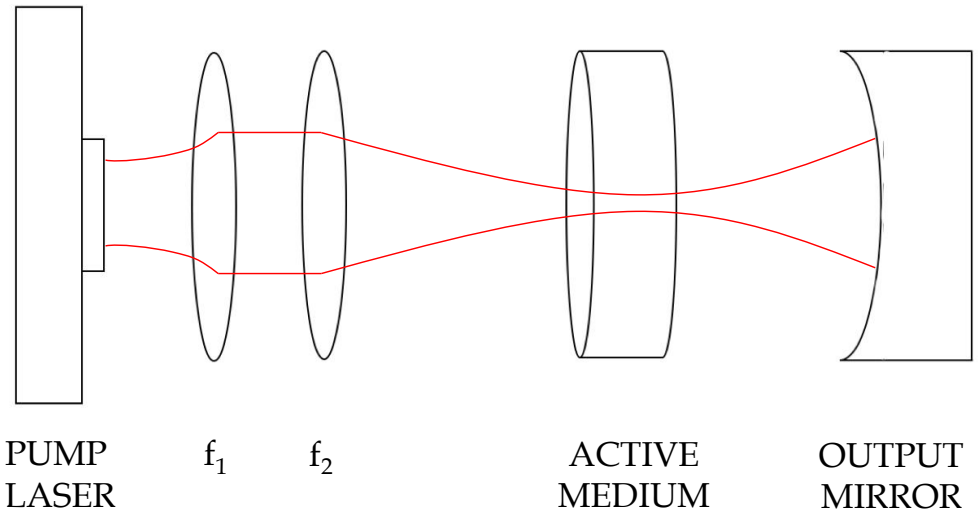

Figure 1.6: Laser components scheme.

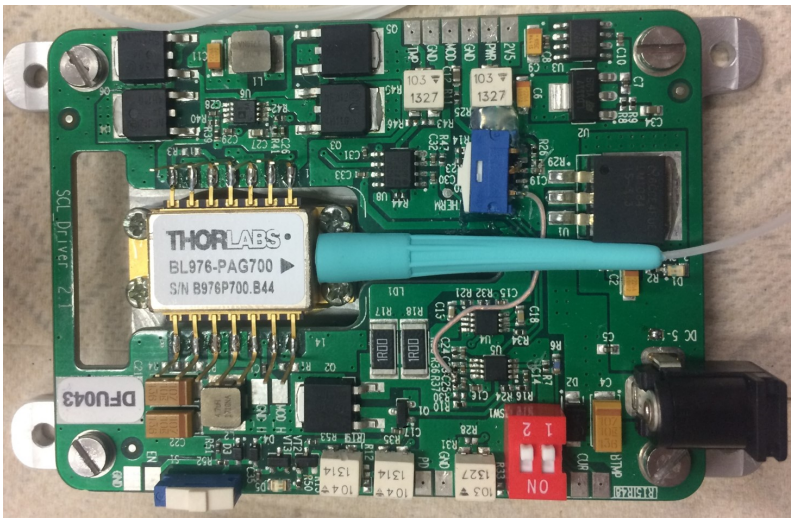

Figure 1.7: Driver DFU043.

temperature of the driver is equal to 25 °C. The control of the output power happens by moving screws clockwise and counterclockwise for increasing and decreasing the current, respectively. Of course, there is a pin also for switch on/off the laser and this is the starting point to work on the laser.

Specifications

LASER RADIATION
AVOID EYE OR SKIN EXPOSURE TO DIRECT OR SCATTERED RADIATION
CLASS 4 LASER PRODUCT

BL976-PAG700 Absolute Max Ratings[a,b]	
LD Reverse Voltage'(Max)	2.0 V
Absolute Max Current	1300 mA
Absolute Max Power	800 mW
PD Reverse Voltage (Max)	15 V
Operating Case Temperature ($T_{Submount}$ = 25 °C)	-5 to +75 °C
Storage Temperature	-40 to 85 °C
Max Tightening Torque	150 mN·m

a. Absolute Maximum Rating specifications should never be exceeded. Operating at or beyond these conditions can permanently damage the laser.
b. T_{chip} = 25 °C, T_{CASE} = -5 °C to 75 °C

BL976-PAG700 Operation Specs				
	Symbol	Min	Typical	Max
Peak Wavelength[a]	λ_p	975.0 nm	976 nm	976.5 nm
Spectral Bandwidth, @ -3 dB	$\Delta\nu$	-	0.6 nm	1.0 nm
Output CW Operating Power	P_{OP}	700 mW	-	-
Kink-Free Power	$P_{Kink-Free}$		770 mW	
Threshold Current	I_{TH}	-	63 mA	85 mA
Forward Current (@ P_{Op})	I_{OP}	-	1090 mA	1150 mA
Slope Efficiency	$\Delta P/\Delta I$	0.64 W/A	0.68 W/A	-
Forward Voltage	V_F	-	1.9 V	2.2 V
Power Stability[b]	P_{stab}	-	< 1%	2%
Temp. Coefficient of FBG (@ P_{OP})	$\Delta\lambda/\Delta T$	-	0.01 nm/°C	0.02 nm/°C
Monitor PD Responsivity[c] (@ I_{OP})	I_{MON}/P	0.5 µA/mW	-	10 A/mW

a. Vacuum Wavelength, @T_{CASE} = T_{FBG} = 25 °C
b. Peak-to-peak operating power, 10 Hz to 50 kHz, over 60 seconds.
c. The monitor diode indicates the power from the Fabry-Perot chip rear facet and is intended to be used as an approximate indicator of power out of the front.

Figure 1.8: 700 mW laser diode specifications.From Thorlabs datasheets.

The pump laser model is BL976-PAG700 made by Thorlabs; it is well suited for low noise core pumping of Erbium-doped fiber. From the specifications sheet, it's shown that the peak wavelength is at 976 nm and the maximum output power is 700 mW. The laser is FBG (Fiber

Bragg-Grating) stabilized and the output laser beam is single mode. In the Figure 1.8 the diode specifications are illustrated.

The fiber of the diode is a PANDA (Polarization-mantaining AND Absorption reducing fibers) type SM98-PS-U25A-H made by Fujikura. From the specifications shown in the Figure 1.9 it is possible to see that the mode field diameter is 6.6 µm, so the output spot size (the radius) at the beam waist is w_0 =3.3 µm. From this value it is possible to calculate the w_0 after the collimator

BL976-PAG700 Fiber Characteristics			
	Min	Typical	Max
Fiber Type	SM98-PS-U25A-H or Equivalent PM Fiber		
Polarization State	Aligned to Slow Axis of Fiber		
Protection Tubing Diameter	900 um		
Fiber Coating Diameter	230 µm	250 µm	270 µm
FBG Coat Diameter	-	-	400 µm
Fiber Termination	FC/APC, 2.0 mm Narrow Key		
Key Alignment	Key Parallel to Slow Axis of Fiber		
PER	-	10 dB	-
F-P Gain Chip to FBG Distance[a]	1.9 m	2.0 m	2.1 m
Fiber Distance after FBG	0.4 m	1.0 m	-
Bend Radius	25 mm	-	-

a. To the center of the FBG, approximate location marked on outside of tubing

(a)

PANDA fiber specifications

Fiber Type	λ_0	MF Dia	Concen-tricity error	Fiber major diameter	Attn	Beat Length	Polari-zation Crosstalk	Cut-off wavelength	Coating Structure	Coating diameter
	Micro-ns	Micro-ns	Max. microns	Microns	Max dB/km	mm	Polari-zation Crosstalk	Max. dB/100m		Microns
SM98-PS-G20A	0.98	6.6(*)	0.7	125+/-1	2.5	1.5- 2.7	-25	0.80 ~ 0.95	UV/Polyester-elastomer(Green) Polyolefin(Gray)	2000+/-200
SM98-PS-H90A									UV/Polyester-elastomer(Green)	900+/-100
SM98-PS-N90A									UV/Polyamide(Green)	
SM98-PS-U40A							-30		UV/UV	400+/-15
SM98-PS-U25A										245+/-15
SM98-PR-U25A-H					3.0	2.8- 4.9	-25			

(b)

Figure 1.9: Fiber specifications: a) from Thorlabs datasheet; b) from Fujikura datasheet.

In this project also another diode laser is used. The pump laser model is BL976-SAG300 made by Thorlabs. The driver has the same functionality as the one previously presented and the model is DFU042. From the specifications sheet, it's shown that the peak wavelength is at 976 nm and the maximum output power is 300 mW. The laser is FBG (Fiber Bragg-Grating) stabilized and the output laser beam is single mode. In the Figure 1.10 the diode specifications are illustrated.

Specifications

BL976-SAG300 Absolute Max Ratings[a]	
LD Reverse Voltage (Max)	2.0 V
Absolute Max Current	600 mA
Absolute Max Power	350 mW
PD Reverse Voltage (Max)	15 V
Operating Case Temperature ($T_{Submount}$ = 25 °C)	-5 to +75 °C
Storage Temperature	-40 to 85 °C
Max Tightening Torque	150 mN•m

a. Absolute Maximum Rating specifications should never be exceeded. Operating beyond these conditions can seriously damage the laser.
b. T_{CHIP} = 25 °C, T_{CASE} = -5 °C to 75 °C

BL976-SAG300 Operation Specs				
	Symbol	Min	Typical	Max
Peak Wavelength[a]	λ_P	975.5 nm	976 nm	976.5 nm
Spectral Bandwidth, @ -3 dB	Δ□	-	-	1 nm
Output CW Operating Power	P_{OP}	300 mW	-	-
Kink-Free Power	$P_{Kink-Free}$		330 mW	
Threshold Current	I_{TH}	-	45 mA	60 mA
Forward Current (@ P_{OP})	I_{OP}	-	470 mA	515 mA
Slope Efficiency	ΔP/ΔI	0.65 W/A	0.76 W/A	-
Forward Voltage	V_F	-	1.8 V	2.0 V
Power Stability[b]	P_{stab}	-	< 1%	2%
Temp. Coefficient of FBG (@ P_{OP})	Δλ/ΔT	-	0.01 nm/°C	0.02 nm/°C
Monitor PD Responsivity[c] (@ I_{OP})	I_{MON}/P	0.5 µA/mW	-	10 µA/mW

a. Vacuum Wavelength, @T_{CASE} = T_{FBG} = 25 °C
b. Peak-to-peak operating power, 10 Hz to 50 kHz, over 60 seconds.
c. The monitor diode indicates the power out of the rear facet and is intended to be used as an approximate indicator of power out of the chip.

Figure 1.10: 300 mW laser diode specifications. From Thorlabs datasheets.

The fiber model of the diode HI 1060 made by Corning. From the specifications shown in the Figure 1.11 it is possible to see that the mode field

diameter is 5.9 µm, so the output spot size (the radius) is w_0 =2.95 µm

1.2.3. Active Medium

A solid-state bulk laser is based on a bulk piece of doped crystal or glass as the active laser medium. Within a laser, the active laser medium (also called gain medium or lasing medium) is the material that emits coherent radiation and exhibits gain. The gain results from electronic or molecular transitions to a lower energy state from a higher energy state to which it had been earlier stimulated. In most cases, the gain medium is doped with rare-earth ions: these ions replace a small percentage of other ions of similar size in the host medium. Concerning the thesis, the project refers to an Er:Yb phosphate glass where the Yb-to-Er energy transfer efficiency is higher than in other glasses due to the higher phonon energies properties of the glass.

Erbium (chemical symbol: Er) is a chemical element belonging to the group of rare earths. It is widely used in the form of the trivalent ion Er^{3+} as the laser-active dopant of gain media based on various host materials, including both crystals and glasses [2]. In the Figure 1.12 the effective gain of the trivalent erbium ion in glass is shown.

In the Figure 1.13 the energy level structure of the trivalent erbium (Er^{3+}) ion and some common optical transitions are shown. The most common laser transition (also widely used in erbium-doped fiber amplifiers) is that from the $^4I_{13/2}$ manifold to the ground-state manifold $^4I_{15/2}$. Depending on the glass composition, the transition wavelength is usually somewhere

BL976-SAG300 Fiber Characteristics			
	Min	Typical	Max
Fiber Type	HI1060 or Equivalent SM Fiber		
Protection Tubing Diameter	900 µm		
Mode Field Diameter[a] @ 980 nm	5.9 ± 0.3 µm		
Numerical Aperture	0.14		
Fiber Coating Diameter	230 µm	250 µm	270 µm
FBG Coat Diameter	-	-	400 µm
Fiber Termination	FC/APC, 2.0 mm Narrow Key		
FP Gain Chip to FBG Distance[b]	1.9 m	2.0 m	2.1 m
Bend Radius	25 mm	-	-

a. Mode Field Diameter (MFD) is specified as a nominal value
b. To the center of the FBG, approximate location marked on outside of tubing

(a)

	HI 1060	RC HI 1060
Key Optical Specifications		
Operating Wavelength (nm)	> 980	
Maximum Attenuation (dB/km)	2.1 @ 980 nm 1.5 @ 1060 nm	
Cutoff Wavelength (nm)	920 ± 50	
Mode-field Diameter (µm)	5.9 ± 0.3 @ 980 nm 6.2 ± 0.3 @ 1060 nm	
Key Geometric, Mechanical and Environmental Specifications		
Cladding Outside Diameter (µm)	125 ± 0.5	80 ± 1
Coating Outside Diameter (µm)	245 ± 10	165 ± 10
Core-to-Cladding Offset (µm)	≤ 0.3	≤ 0.5
Standard Lengths	500 m, 1 km, 2 km, 5 km, 10 km*	
Proof Test (kpsi)	100 or 200	
Operating Temperature (°C)	-60 to 85	
*10 km lengths only available for HI 1060		
Performance Characterizations**		
Nominal Delta (%)	0.48	
Numerical Aperture	0.14	
Refractive Index Value – Core	1.464 @ 651 nm	
Dispersion (ps/nm/km)	-53 @ 980 nm -38 @ 1060 nm	
Bendloss (@ 20 mm O.D.; 1150 nm) (dB/turn)	≤ 0.01	
Core Diameter (µm)	5.3	
** Values in this table are nominal or calculated values		

(b)

Figure 1.11: Fiber specifications: a) from Thorlabs datasheet; b)from Corning datasheet.

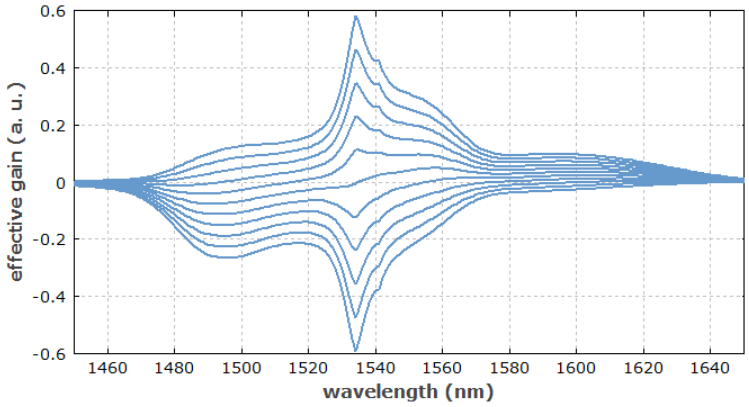

Figure 1.12: Effective gain of the trivalent erbium ion. From [2].

between 1.53 and 1.6 µm.

The most common pump scheme is based on the transition $^4I_{15/2} \rightarrow {}^4I_{11/2}$ with a wavelength around $0.9 \div 1\,\mu m$ (in the project the pump wavelength is 976 nm), although in-band pumping ($^4I_{15/2} \rightarrow {}^4I_{13/2}$, e.g. at 1.45 µm) is also possible. Particularly in bulk crystals, but also in fibers, efficient pump absorption on the $^4I_{15/2} \rightarrow {}^4I_{11/2}$ transition is difficult to achieve, because the absorption cross sections (Figure 1.14) are relatively small, and the doping concentration is limited by the need to avoid excessive quenching processes. A common method to solve this problem is codoping with ytterbium (Yb^{3+}) sensitizer ions, which leads to the erbium-ytterbium-doped laser gain medium. The ytterbium ions can efficiently absorb pump radiation e.g. at 980 nm, and then transfer the energy to erbium ions in the ground-state manifold, bringing them into $^4I_{11/2}$. From that level, the ions are quickly transferred into the upper laser level $^4I_{13/2}$, so that energy transfer back to ytterbium is suppressed.

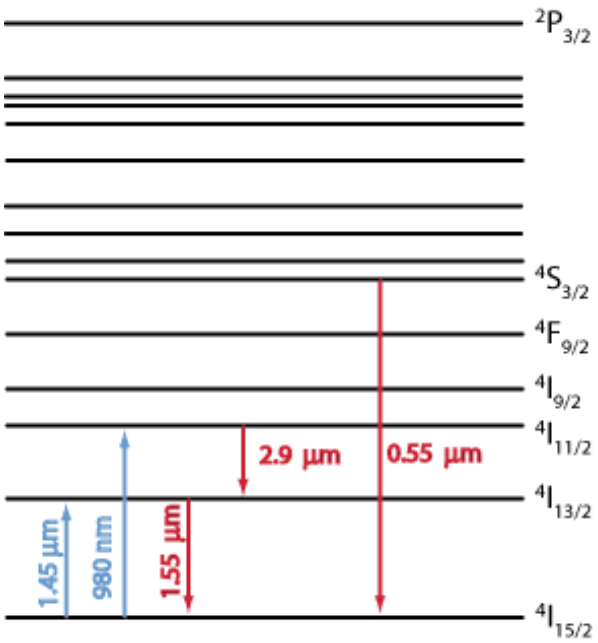

Figure 1.13: Energy level structure of the trivalent erbium ion, and some common optical transitions. From [2].

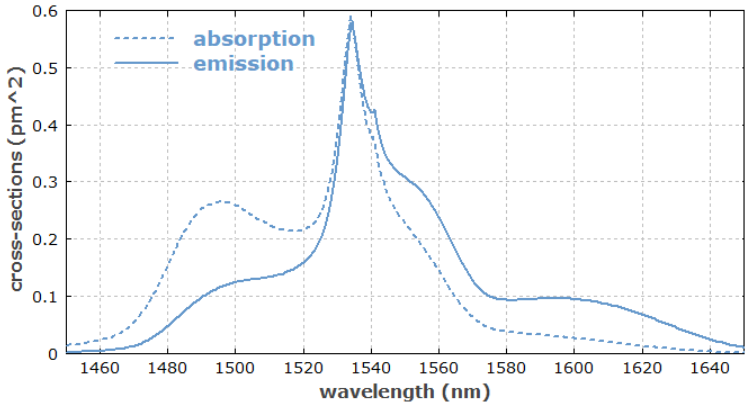

Figure 1.14: Absorption and emission cross sections for erbium ions in Er:Yb-doped phosphate glass, with data from [3]. From [2].

1.2.4. Alignment Process with He-Ne Laser

A He-Ne laser, model NEC GLG5360 (Figure 1.15) made by NEC, operating in continous wave regime, at wavelength equal to 632.8 nm, was used for the optical components alignment process. In the Figure 1.16 the laser specifications are shown. The laser consists of a tube containing the He-Ne mixture, connected directly to the mains with a voltage-boosting transformer. On the opposite side there is a hole which allows the beam output. The structure of the He-Ne laser is depicted in the Figure 1.17.

The He-Ne laser was placed at a fixed height of 20 cm above the plane of the optical table. Two pin holes have been placed at the same height: one at the output beam and one at an arbitrary distance. The laser beam is aligned and perfectly parallel to the plane of the optical table as it passes through the two holes. Then each optical element was placed at a height such that the beam of the He-Ne laser impinged the centre of each element. At this point, lenses and mirrors were tilted and moved in the three directions x, y and z in order to match and line up all possible reflections right at the centre of the pinhole (located at the output of the He-Ne laser). When the alignment is perfect is possible to see the fiber illuminated with a red light due to the red light of He-Ne laser, as shown in Figure 1.18.

Figure 1.15: Photo of the He-Ne laser used in the laboratory.

3. SPECIFICATIONS

3.1 Laser head

TYPE		GLG5260	GLG5360	GLG5270
Minimum Output Power		5.0 mW	5.0 mW	7.0 mW
Polarization		Random	>500:1	Random
Wavelength		632.8 nm		
Transverse Mode		TEM_{00}		Multi mode
Longitudinal Mode Spacing		435 MHz		-
Beam Diameter at $1/e^2$		0.83 mm		0.9 mm(*1)
Beam Divergence		0.96 mrad		4 mrad(*1)
Output Power Stability		<±5 %/24 H		
Warm-up Time		<15 minutes		
Beam Noise and Ripple (10 Hz to 10 MHz)		<1 % rms		-
Static Beam Alignment	Location	<0.1 mm TIR (±0.05 mm)		-
	Angle	<1 mrad		-
Starting Voltage		<10 kV		
Operating Voltage		2350 ± 100 V dc		
Operating Current		6.5 mA		
Operating Temperature		0°C to 50°C		
Storage Temperature		-40°C to 80°C		
Relative Humidity		≦90 %		
Dimensions		44.2 dia. X 396 mm		
Weight		approx. 700 g		

Figure 1.16: Specifications of the He-Ne laser. From NEC datasheets.

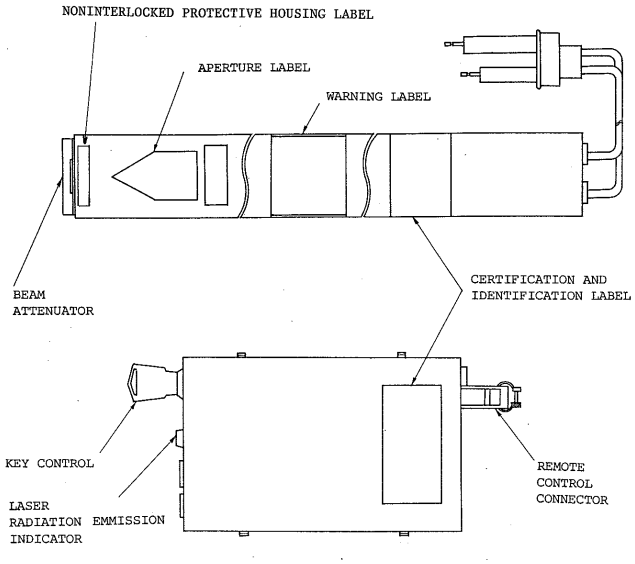

Figure 1.17: He-Ne laser structure. From NEC datasheets.

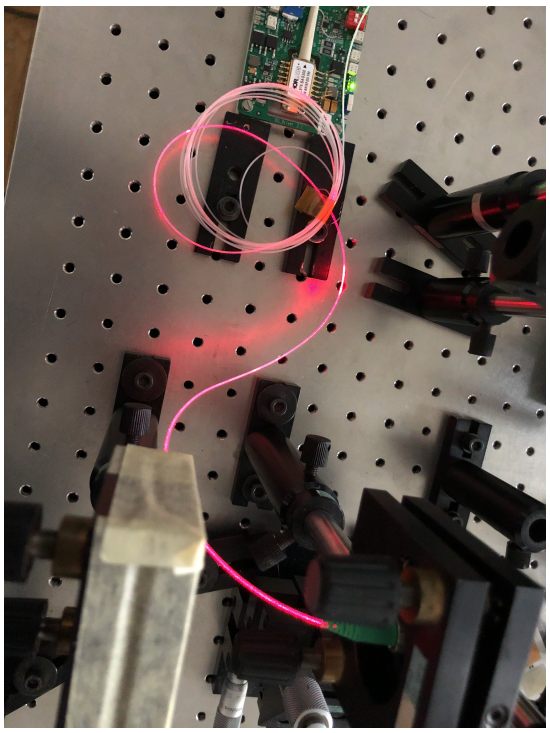

Figure 1.18: Red light illumination of the pump fiber due to perfect alignment between He-Ne laser and optical components.

2 | Optical Power Meters

In this chapter the three types of power meters used for the project are presented. Then a comparison of wavelength sensitivity of the instruments is exposed. In the end a beamsplitter is used in order to further compare the power meters.

This chapter is divided into the following sections:

2.1 Power Meter Heads;

2.1.1 LM-1 (Coherent);

2.1.2 LM-2 VIS (Coherent);

2.1.3 S145C Integrating Sphere (Thorlabs);

2.2 Comparison between Power Meters with respect to Wavelength Sensitivities;

2.2.1 Scale factor Measurements on LM-1;

2.2.2 Responsivity Measurements on S145C.

Figure 2.1: LM-1 Coherent power meter head.

2.1. Power Meter Heads

An optical power meter (OPM) measures the optical power entering the photosensitive area inside the head. It is connected to an electronic device that measures, in a calibrated way, and displays the optical power value.

2.1.1. LM-1 (Coherent)

The LM-1 shown in Figure 2.1 is an optical power meter head made by Coherent. The circular active area diameter is 19 mm, the measurement wavelength range is between 250 and 2500 nm and the maximum power that can be measured is 1 W. This power meter exploits a thermal receiver inside the head that absorbs all the incoming optical energy and measures the difference between the temperature of the environment and that of the sensor, heated by the incoming and fully absorbed optical

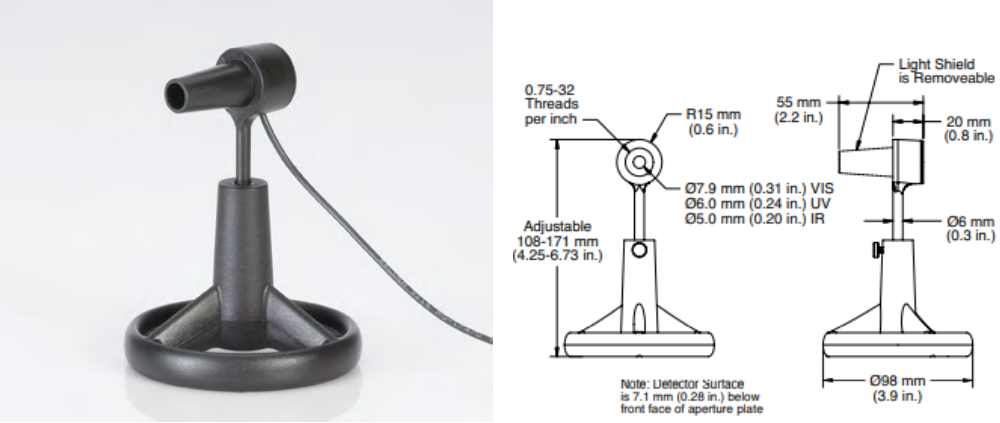

(a) (b)

Figure 2.2: LM-2 VIS OPM from Coherent: a) head; b) scheme.

beam. Thermal receivers have the advantage of a wide wavelength range and a flat (i.e. mostly wavelength-independent) response. In reality, the response is not perfectly flat and the detection has sligthly different responsivity depending on the wavelength so the electronic device connected to the power meter head must be calibrated to the correct wavelength.

2.1.2. LM-2 VIS (Coherent)

The LM2-VIS shown in Figure 2.2 is a silicon power meter head made by Coherent. It is a high-sensitivity semiconductor sensor and it is ideal for CW laser measurements from 10 nW up to 30 mW (the power range is wavelength dependent as shown in Figure 2.3). The best resolution is 1 nW, the circular active area diameter is 7.9 mm and the photodiode material is the silicon (Si). The measurement wavelength range is $400 \div 1064$ nm (coherently to the typical responsivity range of the silicon [10]). The responsivity diagram is not flat and follows the typical bell-shaped

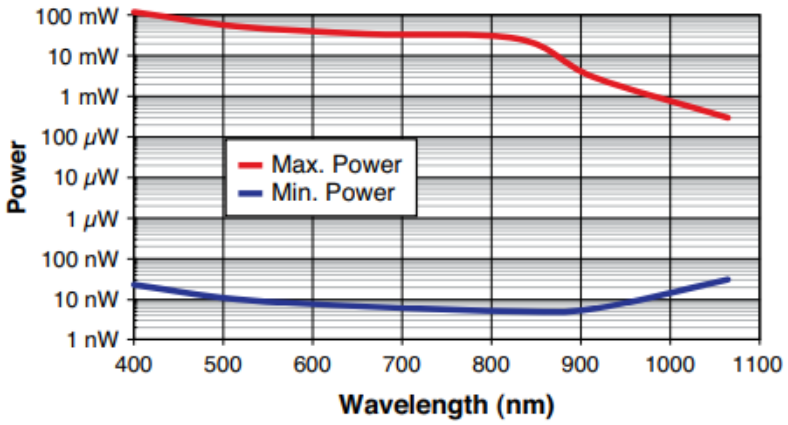

Figure 2.3: LM-2 VIS power range wavelength dependency. From Coherent datasheets

responsivity curve of silicon photodiodes with a peak around 950 nm.

2.1.3. S145C Integrating Sphere (Thorlabs)

The S145C Integrating Sphere shown in Figure 2.4 is a power sensor head made by Thorlabs. It allows measurement of optical power independent from the divergence angle and shape of the incoming beam. The optical power meter head will detect light from 1 µW up to 3 W over different measurement range. The S145C optical power meter head is designed for both fiber-coupled applications and free space. The resolution is 1 nW, the input aperture diameter is 12 mm, the active detector diameter inside the sphere is 2 mm and the detector material is InGaAs. The resposivity diagram shown in Figure 2.5 is not flat and follows the typical bell-shaped responsivity curve of InGaAs photodiodes with wavelength range $800 \div 1700$ nm and peak around 1580 nm. Therefore, the wavelength selected on the electronic device connected to the power meter must be the same as that of the beam being measured in order to correctly

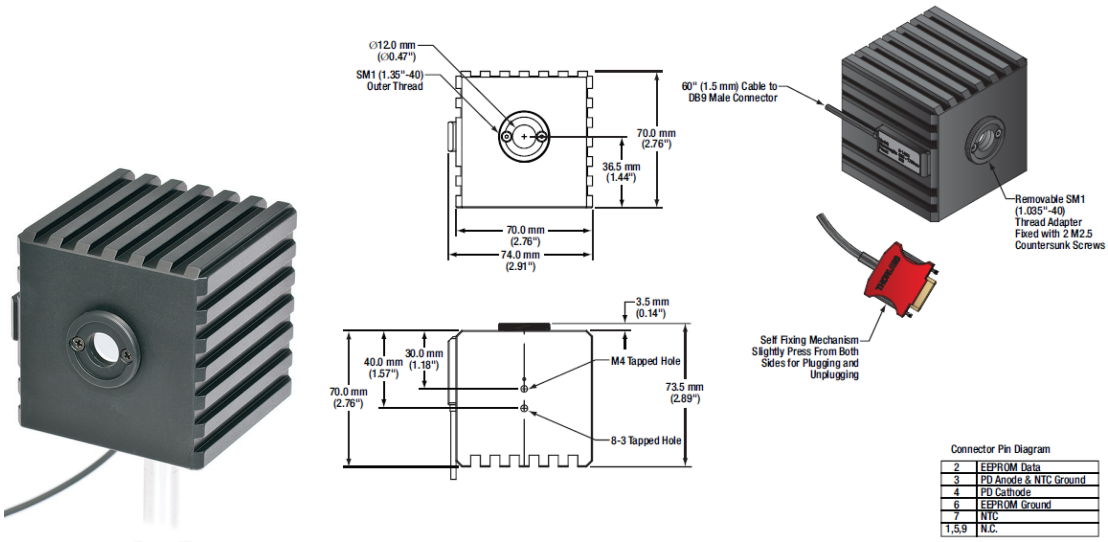

(a) (b)

Figure 2.4: S145C Integrating Sphere from Thorlabs: a) head; b) scheme.

estimate the power.

2.2. Comparison between Power Meters with respect to Wavelength Sensitivities

In general, the lasers used in laboratory were not built to have variable wavelengths. To understand the sensitivity of the power meters to λ variations, a laser with constant power and wavelength is therefore used and the wavelength setting of the photodetector instrument is changed. In this way, the responsivity of the instruments can be measured and the behaviour of the various sensors to wavelength variations can be confirmed. Thermal sensors should have a flat response (almost wavelength independent), whereas semiconductor sensors should have a bell-shaped response. Given that the instrument has variable responsivity depending

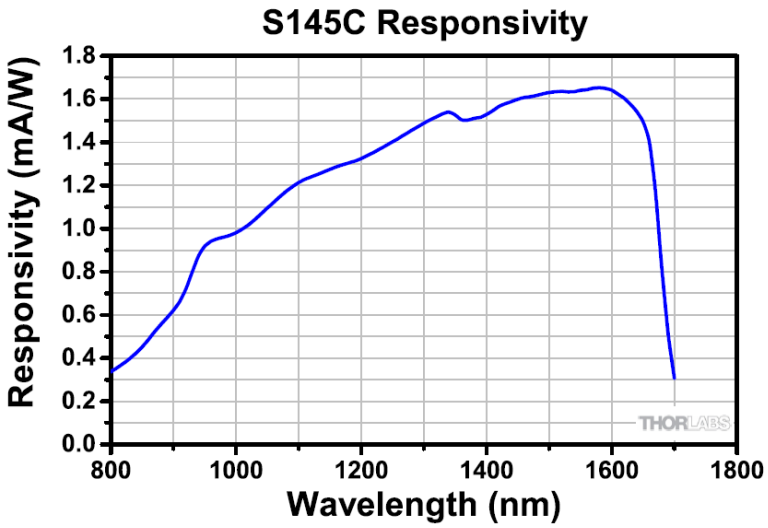

Figure 2.5: Typical responsivity graph of the S145C Integrating Sphere. From Thorlabs datasheets.

on λ, the estimated power is multiplied by a multiplication or scale factor (that we called K and is strictly related to the responsivity), different for each λ, in order to calibrate the instrument and show the correct power on the electronic device.

Indirect responsivity measurements were carried out in the laboratory for both the LM-1 power meter and the Integrating Sphere using the pump laser diode BL976-PAG700 with 4.55 mm collimator and $\lambda_{\text{laser}} = 976$ nm. The drive current was set at 395 mA resulting in a given value of output power (different value depending on the instrument used); this fixed power was used as a reference to calculate the multiplication factor K of the LM-1 power meter and the responsivity σ of the Integrating Sphere power meter.

2.2.1. K-factor Measurements on LM-1

The measurements started with the multiplication factor K of the LM-1 Coherent power meter, that is inversely proportional to the responsivity of the instrument. At $\lambda = 976$ nm the output power was 209 mW. This value, in our estimation, corresponds to $K = 1$ because it is the reference power from which we start the calculations. Then the wavelength selected on the electronic device was changed from 250 nm to 2500 nm and the output power measured changed as well. $\Delta\lambda$ is the spacing in wavelength between two measured powers, in our measurement. It was variable according to the λ variation possibilities of the electronic device connected to the power meter head and according to the needs of the measurement. At the end, all the measured powers were divided by the value of the power corresponding to the correct laser wavelength before mentioned ($\lambda_{\text{laser}} = 976$ nm, $P_{\text{out}}(\lambda_{\text{laser}}) = 209$ mW) according to:

$$K = \frac{P_{\text{out}}(\lambda)}{P_{\text{out}}(\lambda_{\text{laser}})} = \frac{P_{\text{out}}(\lambda)\,[mW]}{209\,[mW]}\,. \tag{2.1}$$

In this way the K factor was calculated and its diagram with respect to wavelength can be seen in the Figure 2.6. The response to wavelength variations is almost flat, which confirms the behaviour of thermal sensors.

2.2.2. Responsivity Measurements on S145C

The responsivity σ of a photodetector is the ratio of generated photocurrent and incident (or sometimes absorbed) optical power (neglecting noise

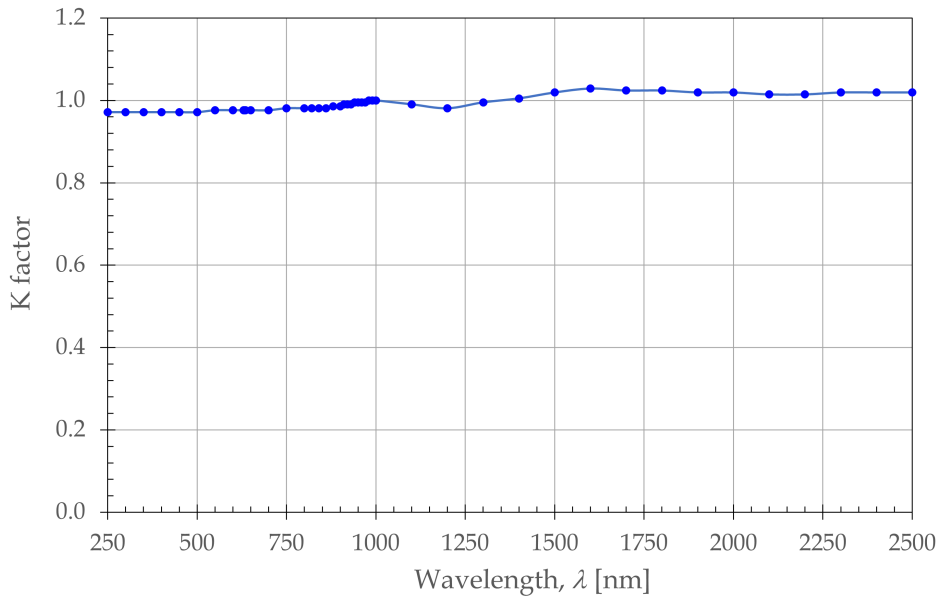

Figure 2.6: LM-1 K factor graph.

influences), as obtained in the region of effective response [11]. In the case of photodiodes, the responsivity is typically highest in a wavelength region where the photon energy is somewhat above the band gap energy, and declining sharply in the region of the bandgap, where the absorption decreases. It can be calculated according to:

$$\sigma = \frac{\eta\, e\, \lambda}{c\, h}\,, \tag{2.2}$$

where η is the quantum efficiency, e is the electron charge, λ is the wavelength of the incident beam, c is the speed of light and h is the Planck's constant. Thermal detectors usually have a responsivity with a weak wavelength dependence in a broad spectral range, in contrast to photodetectors like photodiodes where the responsivity typically drops sharply for photon energies (and corresponding wavelengths) around the

band gap energy.

A measurement was carried out in the laboratory estimating the responsivity of the S145C Integrating Sphere in order to compare it with the one given by Thorlabs. At $\lambda = 976$ nm the output power was 221 mW and the wavelength range selected on the electronic device was $800 \div 1700$ nm. $\Delta\lambda$ was 10 nm, except near the wavelengths of interest, where the wavelength spacing was finer and equal to 2 nm (this precise and fine spacing was made possible by the Integrating Sphere power meter, which is more advanced than the LM-1). At the end the responsivity was calculated for each wavelength and the unit of measure is [mA/W]. This is a focal point to explain, because in the literature the typical responsivity of a InGaAs photodiode has values around 1 A/W and not around 1 mA/W, as in the measurments carried out. This is because the photodiode is placed inside a sphere. It has been calculated in the laboratory that the area of the photodetector is about one thousandth of the total area of the diffusing sphere. Therefore, only one thousandth of the total power affects the photodiode, generating one thousandth of the photocurrent that would be generated if all the incoming power affected it. For this reason the measured responsivity is exactly one thousandth of the typical responsivity of a photodiode not placed inside the sphere.

From the datasheet provided by Thorlabs the radius of the photodiode is $r = 1$ mm and its circular area can be calculated according to:

$$area_{\mathrm{PD}} = \pi\, r^2 = 3.14 \times 10^{-6}\,[m^2]\,. \tag{2.3}$$

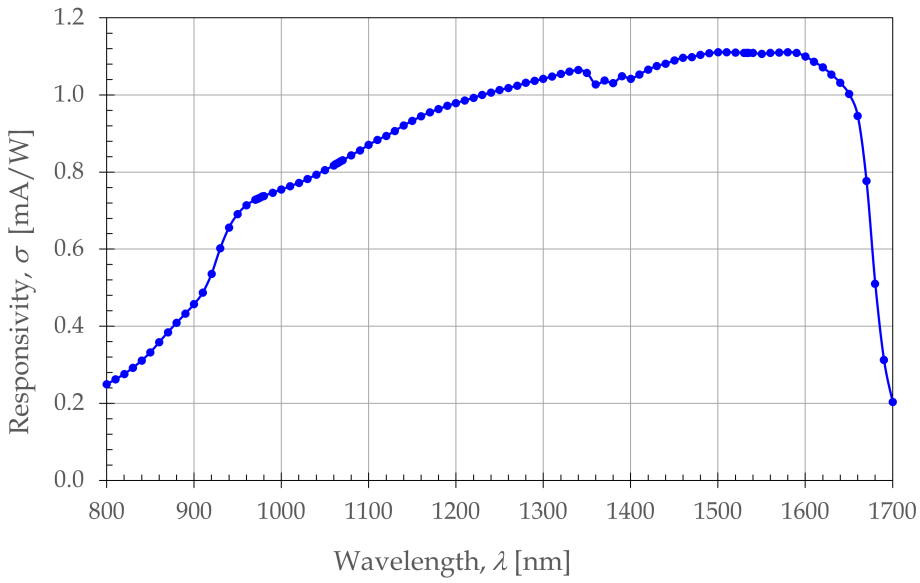

Figure 2.7: S145C Integrating Sphere responsivity measured in the laboratory.

The radius of the sphere was measured in the laboratory, considering it slightly smaller than the cube in which it is inscribed. The radius is $R \cong 32.5$ mm and its surface can be calculated according to:

$$area_{\mathrm{SPH}} = 4\,\pi R^2 = 0.033\,[m^2]\,. \tag{2.4}$$

The ratio between the areas, also equal to $(r/2\,R)^2$, gives a factor that is about 1000.

In the Figure 2.7 the measured responsivity σ with respect to wavelength is shown. The InGaAs photodiode inside the Integrating Sphere Power Meter does not have constant quantum efficiency for all wavelengths (nor constant energetic efficiency in transferring the energy of the single photon into a single photoelectron produced); therefore, even

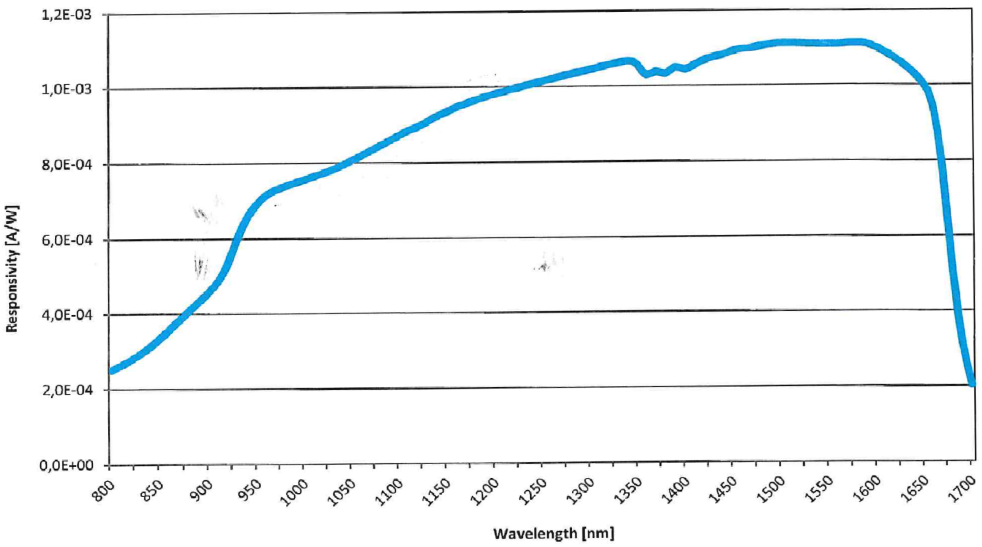

Figure 2.8: S145C Integrating Sphere responsivity measured by Thorlabs.

if the incoming power is constant, the sensor detects a lower or higher power depending on the laser wavelength, which will then be corrected by a different multiplication factor K for each lambda, in order to show the correct value on the display. The value of the K-factor is given by the ratio between the diode laser power detected by the Integrating Sphere at a given wavelength and the actual power at $\lambda_{\text{laser}} = 976$ nm (according to the Equation 2.1 but with $P_{\text{out}}(\lambda_{\text{laser}}) = 221$ mW). If we compare this curve to the one given by Thorlabs and shown in Figure 2.8 it can be seen that the curves are pratically identical (apart from the factor $K = 1000$ explained previously) confirming the responsivity behaviour of the InGaAs photodiode.

In order to show in another way the different behaviour of the two power meters with respect to wavelength variations, a comparison was made. Exactly as with the K-factor measurement for the LM-1 previously ex-

plained, a current was fixed using the driver of the 700 mW diode laser ($\lambda_{\text{laser}} = 976$ nm), then the power was measured with the LM-1 and the Integrating Sphere, varying the wavelength on the electronic device controlling the power meter. After this measurement, the current was changed and two more estimates were made. A total of three measurements were made with three fixed currents (and therefore powers):

1. $I = 216$ mA;
2. $I = 409$ mA;
3. $I = 626$ mA.

In the Figure 2.9 the comparison is shown. The darker lines correspond to the LM-1 power measurements, the lighter ones correspond to the S145C. In green and light green the current was fixed to 626 mA, in red and orange the current was 409 mA and then in blue and light blue the current was 216 mA. The selected wavelength was: $633, 900, 980, 1064, 1550$ nm for the LM-1; while the selected wavelength for the S145C was: $900, 976, 1064, 1550$ nm. It is clear that the response of the LM-1's thermal sensor is approximately flat, exactly as it was shown previously, while the response of the Integrating Sphere is not flat since the power (which should be fixed) changes a lot when λ varies. These behaviours are the exact consequence of the responsivity (variable) and the K-factor measured in the previous section.

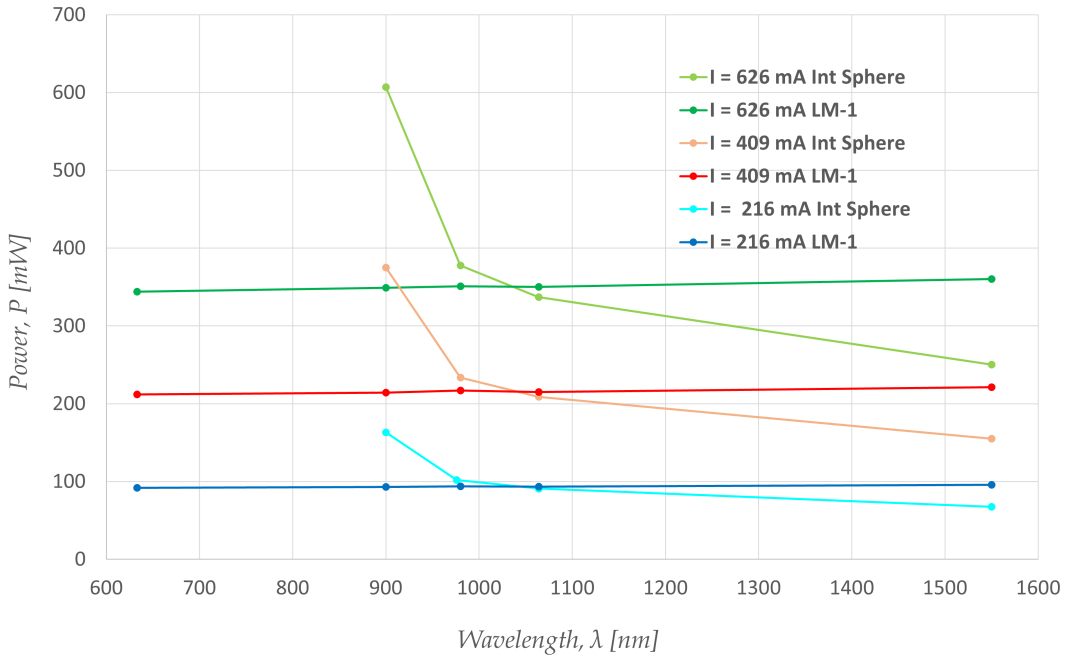

Figure 2.9: Comparison measurements between power meters with respect to wavelength variations.

3 | Knife-Edge Technique and Pump Lasers Characteristics

In this chapter the theory of the Knife-Edge technique is presented. Then measurements on the He-Ne laser using this method are exposed. Eventually the characteristics of the diode pump lasers are measured and illustrated.

This chapter is divided into the following sections:

3.1. Theory and Experimental Set Up

A simple low-cost design to measure the transverse spatial profile of a laser beam is the Knife-Edge technique. In this method, a beam-block realized by a sharp edge made from an opaque material (such as a knife or razor-blade) is line-scanned through the beam perpendicular to its optical axis while the transmitted power is monitored by a detector [12]. The sharp edge (we used a razor blade covered by an opaque material) is built on a mechanical holder with $x - y - z$ micrometer screws for the translation stage. Moving the screws on $x - y$ plane, the razor blade moves perpendicular to the Gaussian beam propagation direction, and it is possible to analyze point to point how much laser power is transmitted to the power meter sensor (the area of the power meter must be larger than the area of the laser beam cross section at the detection position). Considering the y-axis, the razor blade is moved upward from the lowest point of the holder, where the power is maximum, until the point in which the power is zero because the razor blade cuts the entire Gaussian beam. Once represented the experimental data on a $P_{\text{out}} - y$ diagram, a Gaussian fitting curve is superimposed on the points in such a way as to confirm the Gaussian shape of the beam and to reveal artifacts and bad measurements (if the points do not follow the fit curve perfectly). The fitting is performed by the program Microsoft Excel, also used for the graphical representation of data. At this stage, calculated a spot size $w(z)$, the procedure is repeated in other positions on the z axis in order to recreate the beam profile diverging from the waist on a $w(z) - z$

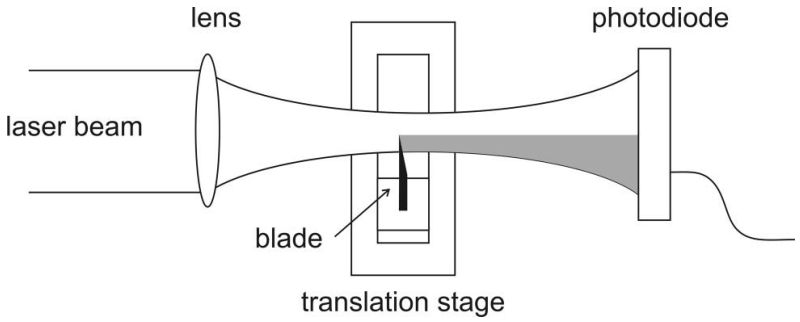

Figure 3.1: Simplified scheme of a spot size measurement using the Knife-Edge technique. From [4].

diagram. The goal of the Knife-Edge technique is to find the value of the spot size in the beam waist w_0. Since the position of the beam waist of our laser is in the cavity, it is not technically accessible using this technique. Using optics calculations it is possible to recreate the beam profile and calculate the spot size in the beam waist indirectly. In the Figure 3.1 a simplified scheme for the measurement of laser beam radius using the Knife-Edge technique. The blade moves on the y-axis while the beam propagates in the z-axis. The gray color area represents the shadow caused by the knife edge.

Let us first consider the intensity of a Gaussian beam:

$$I(x,y) = I_0 \exp\left[-\frac{(x-x_0)^2 + (y-y_0^2)}{w_0^2}\right], \tag{3.1}$$

where I_0 is the peak intensity at the center of the beam, located at (x_0, y_0), x and y are the transverse Cartesian coordinates of any point with respect to an origin conveniently chosen at the beginning of the experiment, and w_0 is the beam radius, measured at a position where the intensity decreases to $1/e^2$ times its maximum value I_0 [4]. Moreover, I_0

is:

$$I_0 = \frac{2\,P_0}{\pi\,w_0}\,, \tag{3.2}$$

where P_0 is the peak power. By setting the y-axis perpendicular to the plane of the optical table ($x - z$ plane) and parallel to the cutting direction of the blade, we know the expression for $P(y_c)$, which is the power recorded when cutting occurs at the cutting co-ordinate y_c:

$$P(y_c) = P_{\text{offset}} + \frac{P_0}{2}\left[1 - erf\left(\frac{\sqrt{2}\,(y - y_0)}{w(z)}\right)\right]\,, \tag{3.3}$$

where P_{offset} is the background optical power that has to be added as a offset, y_0 is the displacement, and erf is the standard error function. This is the equation that will be directly programmed in Excel for the Gaussian curve fitting on every $w(z)$ measurement. From the formula, we get $w(z)$ and for all the values obtained for w in relation to the distance z, the fit on the total graph with respect to z will be done through the equation:

$$w(z) = w_0\sqrt{1 + \left(\frac{z - z_0}{z_R}\right)^2}\,, \tag{3.4}$$

where w_0 is the spot size in the beam waist, $z - z_0$ is the distance from the beam waist, z_0 is the position of the beam waist, and z_R is the Rayleigh range. The Rayleigh range is the point on the z-axis in which the beam radius $w(z)$ is equal to $\sqrt{2}\,w_0$ and its expression is:

$$z_R = \frac{\pi\,w_0^2}{\lambda}\,. \tag{3.5}$$

Considering $z_0 = 0$ mm and combining this equation with the Equation

3.4, $w(z)$ can be written as:

$$w(z) = w_0 \sqrt{1 + \left(\frac{\lambda\, z}{\pi\, w_0^2} \right)^2}\,, \tag{3.6}$$

and in the far-field the beam divergence angle θ_d is related to $w(z)$ following the equation:

$$w(z) \cong \frac{\lambda\, z}{\pi\, w_0} = \theta_\mathrm{d}\, z\,, \tag{3.7}$$

furthermore for small θ_d:

$$\theta_\mathrm{d} \cong tan(\theta_\mathrm{d}) = \frac{\Delta\, w}{\Delta\, z} = \frac{\lambda}{\pi\, w_0}\,, \tag{3.8}$$

so:

$$w_0\, \theta_\mathrm{d} = \frac{w_0^2}{z_0} = {\theta_\mathrm{d}}^2\, z_0 = M^2 \frac{\lambda}{\pi}\,, \tag{3.9}$$

where the M^2 parameter express the quality of the Gaussian beams and denotes the ratio between the effective divergence and the ideal (diffraction limited) divergence. In other words, the M^2 specifies how much beam the divergence exceeds that of a "perfect" Gaussian beam. Large values of M^2 correspond to low spatial beam quality.

An important function for the fit is the standard error function erf seen in the Equation 3.3 and its expression is:

$$erf(x) := \frac{2}{\sqrt{\pi}} \int_{-\infty}^{x} \exp\left(-t^2\right) dt\,. \tag{3.10}$$

In order to perform the fit, the data were processed using Microsoft Excel, as said before. In this program it is not possible to use the standard error

function erf so, thanks to the relation between the error function and the distribution function of the normal distribution $\Phi(x)$:

$$\Phi(x) = \frac{1}{2}\left[1 + erf(y_c)\right] , \tag{3.11}$$

it is possible to use the Excel function $DISTRIB.NORM.N$ according to the Equation 3.3 but replacing the erf with $\Phi(x)$:

$$P(y_c) = \{P_0\left[1 - DISTRIB.NORM.N(h, h_{\text{half}}, w/2, TRUE)\right]\} + P_{\text{offset}} , \tag{3.12}$$

where h is the vector of positions (or heights) of the blade on the y-axis (considering $h = 0$ the first position of the measurement), h_{half} is the half of the maximum value in the h vector, $w/2$ is the half of the width of the curve and "TRUE" is a parameter that makes the Excel function cumulative. We put $1 - (...)$ before the distribution function because all of our measurements started from the maximum power and ended with the minimum powers so the curve had to be inverted and translated to the correct position, in order to be superimposed on the experimental data.

This function creates a theoretical fitting curve (similar to that of a normal distribution function) that represents how the power values measured in our knife-edges should be arranged. In this way, by means of a specific calculation (carried out by the "SOLVER" function) Excel will find the average height h_{half}, width w (towards which we will pay particular attention) and offset parameters that best approximate our data. By

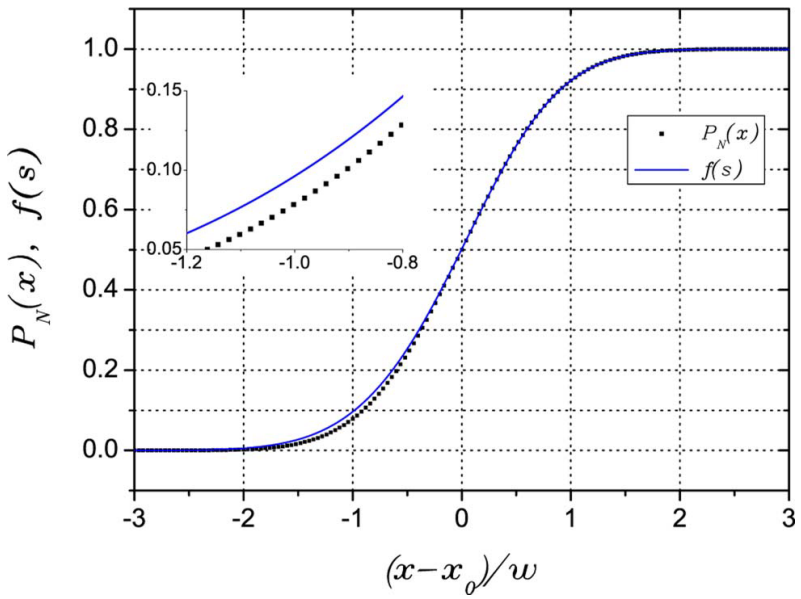

Figure 3.2: Example of fitting of experimental data with a normal distribution function. $P_{\mathrm{N}}(x)$ is the measured power, $f(s)$ is the fitting curve. The horizontal axis is normalized to the width pf the curve. From [4].

repeating this procedure for different distances from the laser origin, it is possible to reconstruct the trend followed by the laser spot size $w(z)$ as the propagation distance varies.

In the Figure 3.2 an example of a fitting of experimental data with a normal distribution function is shown.

3.2. Knife-Edge Technique on the He-Ne laser

In the laboratory the Knife-Edge technique was firstly applied to the He-Ne laser, using the LM-2 VIS power meter presented in Chapter 2. The wavelength of the He-Ne laser is equal to 632.8 nm so only the LM-1 and

the LM-2 VIS are able to detect properly this laser, while the Integrating Sphere has a wavelength range that starts from 800 nm. The goal was to measure indirectly the position and the spot size of the beam waist using the divergence angle (which can be calculated from more than three different $w(z)$ in far-field) and some formulas from optics [5]. Although the spot size of the beam waist and the divergence angle are parameters known from the laser datasheets, these estimates allowed us to confirm their values and at the same time to corroborate the goodness of the measurements made through the Knife-Edge technique.

One of the He-Ne laser best features is the very low divergence, from its datasheet in Figure 1.16 (Chapter 1) θ_{d} is equal to 0.48 mrad (we consider the half-angle). Since this angle is very small, the beam can be considered approximately collimated and so the beam waist position can be considered at $-\infty$. For this reason it was not necessary to calculate the beam waist position on the z-axis. We concentrated on the calculation of the spot size of the beam waist w_0. Furthermore a small divergence angle means that the far-field is far away from the tube, so, considering the size of the room and of the optical table, it was impossible to place the blade and make measurements at distances larger than $80 \div 90$ cm. The far-field is the portion of the field beyond $z_{\mathrm{far}} \geq 10 \cdot z_{\mathrm{R}}$ where the beam diverge linearly, so its divergence can be approximated by a straight line. From the Equations 3.5 and 3.6 we can see that the Rayleigh distance is inversely proportional to the divergence angle, so the smaller this angle, the greater the Rayleigh distance and therefore the further away the far field will be. From the He-Ne datasheet in Figure 1.16 (Chapter 1) we

can see that the beam diameter D is equal to 0.83 mm, so the beam radius, that we called w_0, is equal to 0.415 mm. Knowing that λ is 632.8 nm it is possible to calculate z_{R} according to the Equation 3.5, and the result is $z_{\mathrm{R}} = 0.855$ m. The far-field is beyond $z_{\mathrm{far}} \geq 10 \cdot z_{\mathrm{R}} \geq 8.55$ m, a distance too large for the table and room size.

The solution to this problem was this: considering $z = 0$ mm the position of the He-Ne tube exit, we placed a lens with focal length $f_1 = 150$ mm at $z = 100$ mm, in this way we created a second beam waist w_0', a new divergence angle θ'_{d} and so a closer far-field because of a new z'_{R} much smaller than the one of the He-Ne. Knowing these values and using optics formulas it was possible to recover the spot size of the beam waist of the He-Ne laser.

The last problem was the divergence of the beam after the focus in w_0'. The beam diverged a lot and became much wider than the LM-2 VIS sensor area. In order to solve this problem we placed a second lens that we called "collect lens" in such a way as to create a new focus and narrow the beam radius. We positioned the power meter in this focus location, since the scaled beam surface had become much smaller than the sensor area. A sketch of the beam propagation scheme with lenses and power meter position can be seen in the Figure 3.3 simulated with the program "Gaussian Beam.exe".

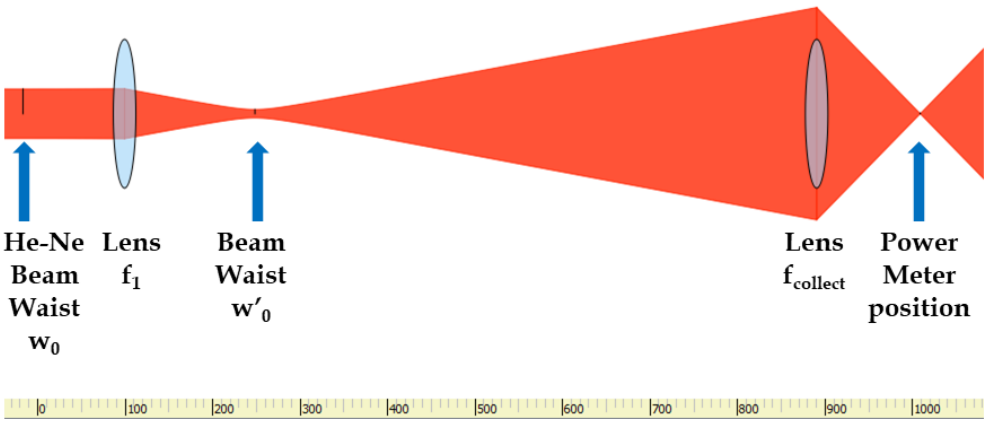

Figure 3.3: Simulation of the He-Ne beam propagation through the first lens $f_1 = 150$ mm placed in $z = 100$ mm and the second "collect" lens $f_{\text{collect}} = 100$ mm placed in $z = 891$ mm. From program "Gaussian Beam.exe".

3.2.1. Beam waist and Divergence Angle Measurements

The pratical steps for measuring the divergence angle and then the beam waist spot size was:

- measure the spot size of the beam waist w'_0 after the first lens using the Knife-Edge technique;
- measure the spot size $w(z)$ in more than three positions, on the z-axis, in far-field and/or far-far-field (15 times or more the Rayleigh distance);
- find the straight line that pass through the points in far-field and far-far-field;
- estimate the divergence angle θ'_{d} of the path after the first lens

through formulas or Excel regression function;

- compare the experimental data with theoretical data calculated with formulas;
- apply the formulas that relate θ'_{d} to the spot size of the beam waist w_0 of the He-Ne laser;
- compare w_0 and θ_{d} with the specifications present in the datasheets of the He-Ne laser;
- compare all the data with simulations of the program "Gaussian Beam.exe".

Considering $z = 0$ mm the position where the He-Ne laser starts (the exit of the tube), we placed the first lens with $f_1 = 150mm$ in $z = 100$ mm and used a piece of paper in order to spot the laser (that is in the visible wavelength range and does not need special phosphor maps). In this way we found the approximate position of the beam waist w'_0 ($z_{\mathrm{waist}} \cong 250$ mm) and started the measurements using the Knife-Edge technique. The number of points in which we placed the blade on the $x - y - z$ holder for the measurements was 14 in the near-field, 4 in the far-field and 3 in the far-far-field. We found a total of 21 different $w(z)$ that in the end we plotted in a single graph.

In the Figure 3.4 an example of a measurement of $w(z)$ in near-field is shown. The position is $z = 246$ mm, so extremely close to the beam waist. The red dots represent the measured powers varying the height of the blade, Δh is equal to 0.01 mm. The black line represents the Gaussian fitting curve calculated in Excel with the $DISTRIB.NORM.N$ function.

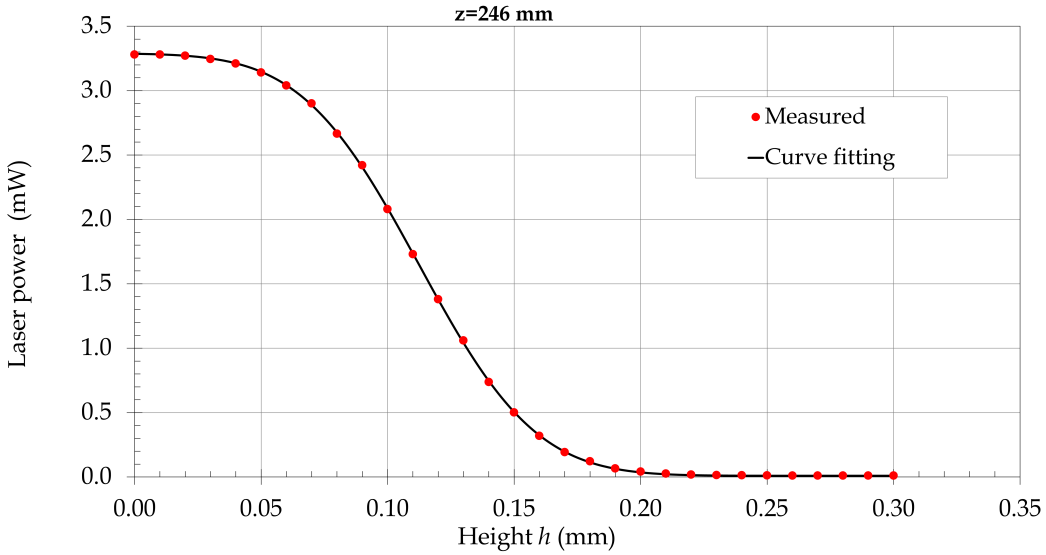

Figure 3.4: $w(z)$ measurement example in the position $z = 246$ mm (near-field). The red dots represent the measured powers varying the height of the blade. The black line represents the Gaussian fitting curve calculated in Excel. $\Delta h = 0.01$ mm.

The black theoretical line fits perfectly the trend of the experimental data, this means that the shape of the beam is perfectly Gaussian and that the measurement is good. The spot size $w(z)$ calculated is equal to 0.073 mm.

In the Figure 3.5 an example of a measurement of $w(z)$ in far-field is shown. The position is $z = 569$ mm and in this case Δh is equal to 0.1 mm. The spot size $w(z)$ calculated is equal to 0.9 mm.

In the Figure 3.6 an example of a measurement of $w(z)$ in far-far-field is shown. The position is $z = 813.5$ mm and in this case Δh is equal to 0.15 mm. The spot size $w(z)$ calculated is equal to 1.58 mm.

The spot size of the beam waist was equal to 72 µm and its position

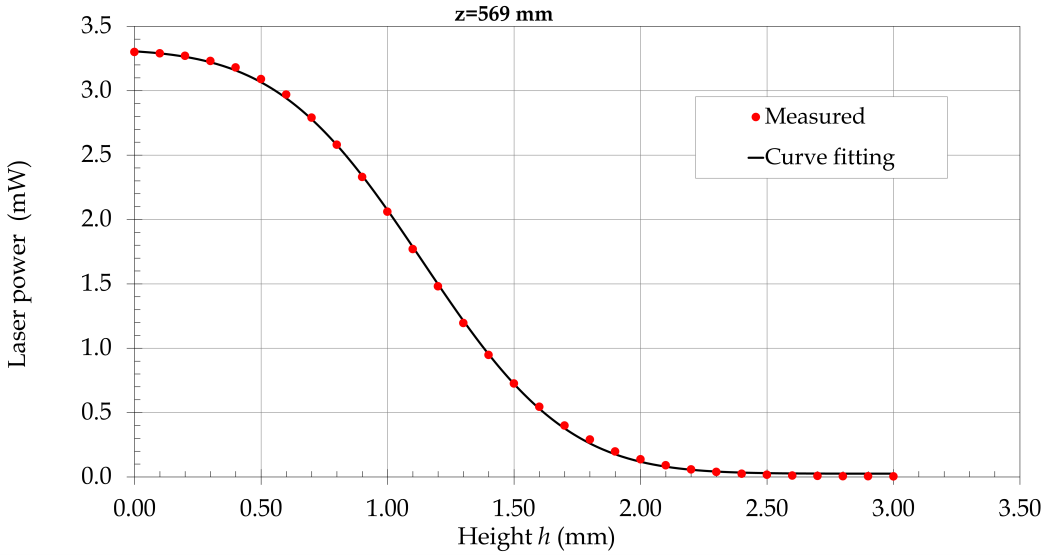

Figure 3.5: $w(z)$ measurement example in the position $z = 569$ mm (far-field). The red dots represent the measured powers varying the height of the blade. The black line represents the Gaussian fitting curve calculated in Excel. $\Delta h = 0.1$ mm.

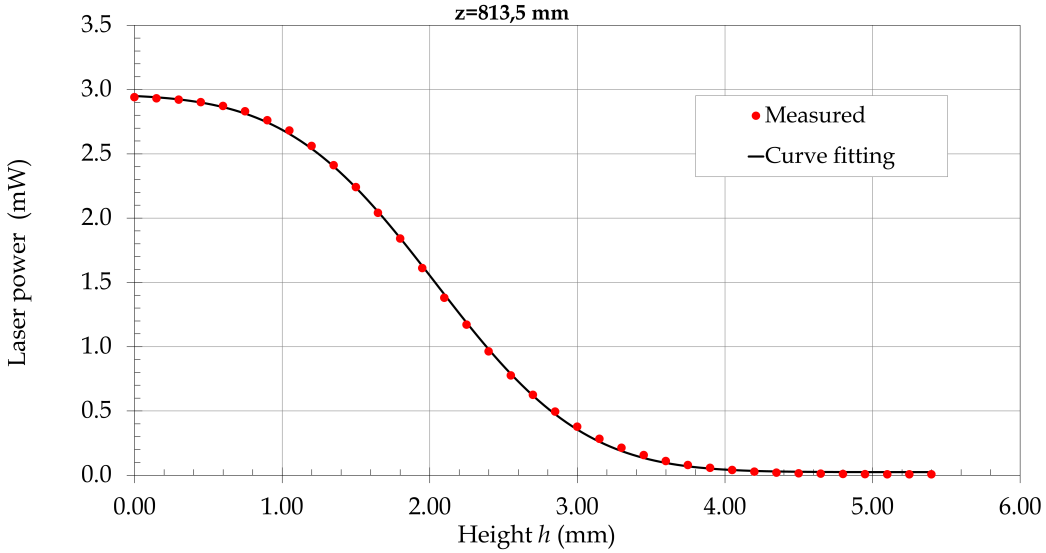

Figure 3.6: $w(z)$ measurement example in the position $z = 813.5$ mm (far-far-field). The red dots represent the measured powers varying the height of the blade. The black line represents the Gaussian fitting curve calculated in Excel. $\Delta h = 0.15$ mm.

was in $z = 249$ mm. At this point we collected all the measurement in one graph with respect to the z-axis. Using only the far-field data, we calculated the best straight line passing through the points; since they might not be perfectly aligned, we used the regression linear function available in Excel calculating also the equation of the line. The angular coefficient represents exactly the divergence angle of the beam θ'_{d}, that is equal to 2.8 mrad. Having the divergence angle it was possible to find the Rayleigh distance: $z_{\mathrm{R}} = 25.768$ mm, in this way the far field started from about 260 mm after the w'_0 position, so beyond $z \geq 509$ mm. Then we calculated the theoretical values of all the $w(z)$ (we called them $w_{\mathrm{th}}(z)$) using the Equation 3.6, in order to make a comparison with the experimental data. The formula has been modified to take into account the M^2 parameter in this way:

$$w(z) = w_0 \sqrt{1 + \left(\frac{M^2 \lambda z}{\pi w_0^2} \right)^2}, \tag{3.13}$$

Having the theoretical data available, we were able to use the function "SOLVER" in Excel so that it was possible to find the w_0, the $w_{\mathrm{th}}(z)$s and the M^2 that best approximate our data. The theoretical values of the spot sizes were very similar to those measured and the M^2 parameter found was 1.002, this meant that the beam had a perfect Gaussian shape.

In the Figure 3.7 the final graph containing all the measured $w(z)$ using the Knife-Edge technique is shown. The blue dots represent the experimental data and are connected by a red interpolating line. The red dots represent the theoretical values $w_{\mathrm{th}}(z)$. The black line represent the re-

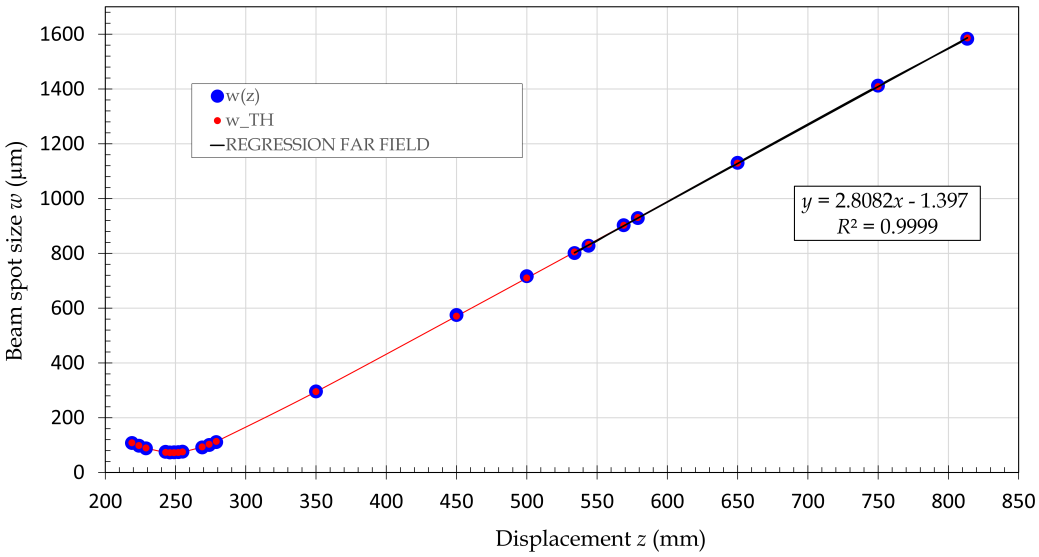

Figure 3.7: $w(z)$ measurements graph using the Knife-Edge technique.

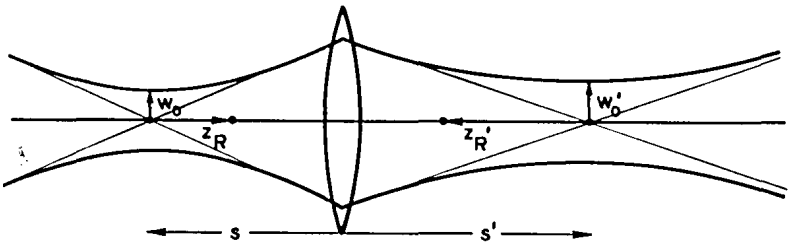

Figure 3.8: Geometry of the imaging of a Gaussian beam by a lens. From [5].

gression curve calculated with Excel using only the far-field data. On the right, the equation of the regression line of the far-field data is written.

Until this stage we found the position of the beam waist after the lens: $z = 249$ mm, $w'_0 = 72\,\mu$m and $\theta'_{\mathrm{d}} = 2.8$ mrad.

The next step was the calculation of w_0. In the Figure 3.8 the geometry of the propagation of a Gaussian beam through a thin lens is shown.

In our case the focal length of the lens is $f_1 = 150$ mm and the dis-

tance between the lens and the image beam waist w_0' is $s' = 149$ mm as measured before. Starting from the standard thin lens or mirror formula [5, 13, 14]:

$$\frac{1}{s} + \frac{1}{s'} = \frac{1}{f_1}\,, \tag{3.14}$$

where s, s' are the object and image distances respectively, it is possible to derive the magnification factor m according to:

$$m = \left|\frac{s'}{s}\right| = \frac{1}{|1 - (s/f)|}\,, \tag{3.15}$$

and after some calculations it is possible to write m as function of w_0 and z_R according to:

$$m = \frac{w_0'}{w_0} = \frac{1}{\{[1 - (s/f)]^2 + (z_\mathrm{R}/f)^2\}^{1/2}}\,. \tag{3.16}$$

Since we calculated the Rayleigh distances of the two paths before ($z_\mathrm{R} = 855$ mm) and after ($z'_\mathrm{R} = 25.768$ mm) the lens and knowing that the magnification factor m is related to these distances as:

$$m = \sqrt{\frac{z'_\mathrm{R}}{z_\mathrm{R}}}\,, \tag{3.17}$$

it was possible to determine m. Knowing from the measurements that w_0' was equal to 72 µm, using the Equation 3.16 we derived the spot size of the He-Ne beam waist w_0, equal to 0.415 mm, that is exactly the same of that in the datasheets.

The fact that the w_0 is confirmed tells us that the measurements made

with the Knife-Edge technique was perfect. In order to further confirm and visualize the measurements a program called "Gaussian Beam.exe" was used. This program simulates the beam propagation in free space with the possibility to add lenses and see how the beam behaves. In the Figure 3.9 the simulation with the data set in the program is depicted. We started with setting the λ equal to 633 nm, then we placed the first lens in $z = 100$ mm with focal length equal to 150 mm and the collect lens in $z = 891$ mm with focal length equal to 100 mm. At this point, one of the parameters (w_0, w'_0, s', θ_d or θ'_d) has to be chosen, so that all the others are calculated and set automatically by the program according to the theory of Gaussian beam propagation. If the parameters are correct, it does not matter which one we choose because the others will be calculated by the program accordingly. In our case the parameters were correct and confirmed by the program, as it is possible to see in the data shown in Figure 3.9. $w_0 = 0.42$ mm, $w'_0 = 72\,\mu$m, $s' = 149$ mm, $\theta_\mathrm{d} = 0.48$ mrad, $\theta'_\mathrm{d} = 2.8$ mrad. The position of the input beam is arbitrary because, as we said, the beam is approximately collimated.

3.3. Measurements on Diode Pump Lasers

In order to understand the pump laser characteristics, one of the most important plots we needed was the output power of the pump laser vs. the current given by the driver. The result of this measurement was the optical power vs. current characteristic, then compared with the data provided by the manufacturer Thorlabs. Theoretically the power, when

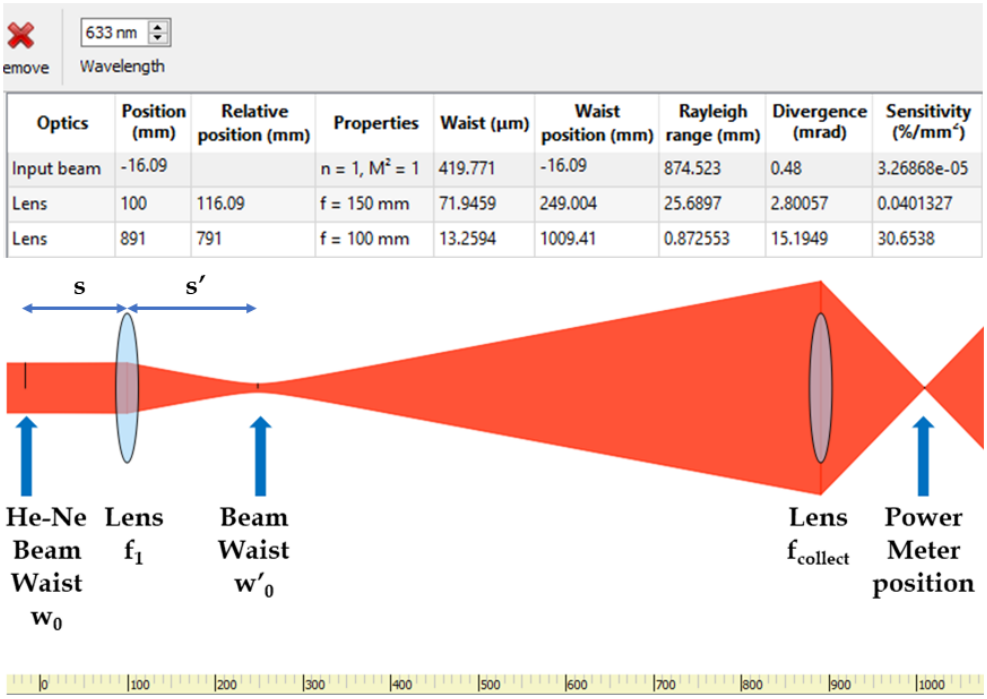

Figure 3.9: Guassian Beam simulation of the He-Ne beam propagation through the first lens $f_1 = 150$ mm placed in $z = 100$ mm and the second "collect" lens $f_{\text{collect}} = 100$ mm placed in $z = 891$ mm.

the threshold condition is achieved, should increase linearly according to:

$$P_{\mathrm{LD}} = I_{\mathrm{LD}}\, V_{\mathrm{LD}}\,, \tag{3.18}$$

where LD stands for laser diode, P_{LD} is the output power of the laser diode, V_{LD} is the forward voltage and I_{LD} is the current provided to the diode. The current was controlled by rotating the small screw present on the driver: clockwise the current increases, counterclockwise the current decreases. The ΔI is not fixed because it was very difficult to rotate the screw to achieve a certain derided current. Since it was not important that the spacing between the points was fixed, we collected the data anyway, with variable ΔI. We used a digital multimeter made by UNI-T to read the current during the measurements.

The LM-1 power meter for the 300 mW diode laser and the integrating sphere together with the LM-1 for the 700 mW laser diode were used to measure the optical power. Alignment of the laser diode fiber was carried out with the help of the He-Ne laser to ensure that the infrared beam was parallel to the optical table plane, and then the power meter used was manually placed in the best position, maximising the power for the same current. Measurements were made with and without the available collimators for both laser diodes.

Collecting the experimental data in a graph, a linear characteristic was obtained, with very small deviations. In the first area of the graph, the threshold condition has not yet been reached, so the power remains zero as the current increases. Above the threshold current (calculated

as the current that generates an output pump power equal to 1 mW), the laser starts to propagate and the power increases linearly. A linear regression curve was graphically superimposed to the data, representing the theoretical trend of the data. In all cases, the curve follows perfectly the collected data.

3.3.1. 300 mW Diode Pump Laser

The power-to-current characteristic of the 300 mW diode laser was obtained in two different cases by placing two collimators available in the laboratory on the fiber head, with focal length respectively $f_1 = 4.55$ mm and $f_2 = 8.06$ mm. The optical power measurement was obtained using the LM-1 power meter. From the theory we expected a linear characteristic. In the Figure 3.10 a graph representing the power measured varying the current provided to the driver is shown. The collimator with focal length $f_1 = 4.55$ mm was attached to the fiber head. The dotted black line represents the linear regression of the data, which perfectly follows the experimental data represented with blue dots. On the right the equation of the linear regression is presented and its angular coefficient represents the slope efficiency ($\eta_{\text{slope}} = \Delta P/\Delta I$) of the diode laser. In this case the slope efficiency is equal to 0.7115 W/A. The characteristic is linear, as expected, and the threshold current is about 48 mA. Since the maximum power is 300 mW, we stopped the measurement at a value of power smaller than this value, in order to avoid damages.

In the Figure 3.11 it is illustrated the same measurement as before but with different the collimator whose focal length is $f_2 = 8.06$ mm. The

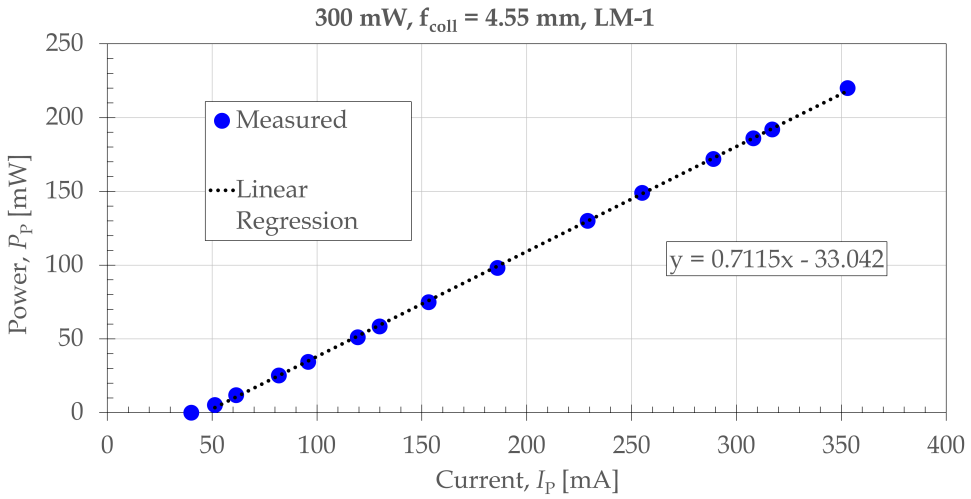

Figure 3.10: Power-to-current characteristic of the 300 mW diode laser with collimator $f_1 = 4.55$ mm.

angular coefficient in the equation of the linear regression tells us that the slope efficiency of the diode laser that in this case is equal to 0.7292 W/A. The characteristic is linear as expected and the threshold current is about 50 mA. Changing the collimator, the characteristic remained almost the same.

In the Figure 3.12 the power-to-current characteristic made by Thorlabs is shown in the blue line, as a comparison to the experimental data. The graphs are very similar, the threshold currents are almost the same and the typical values of the slope efficiency from the datasheet of the 300 mW diode laser in Figure 1.10 (Chapter 1) are in the range of $0.65 \div 0.76$ W/A. The η_{slope} measured are in this range but slightly below the typical value present in the datasheet. This is possibly due to damage from wear and tear or due to poor power estimation by the power meters used.

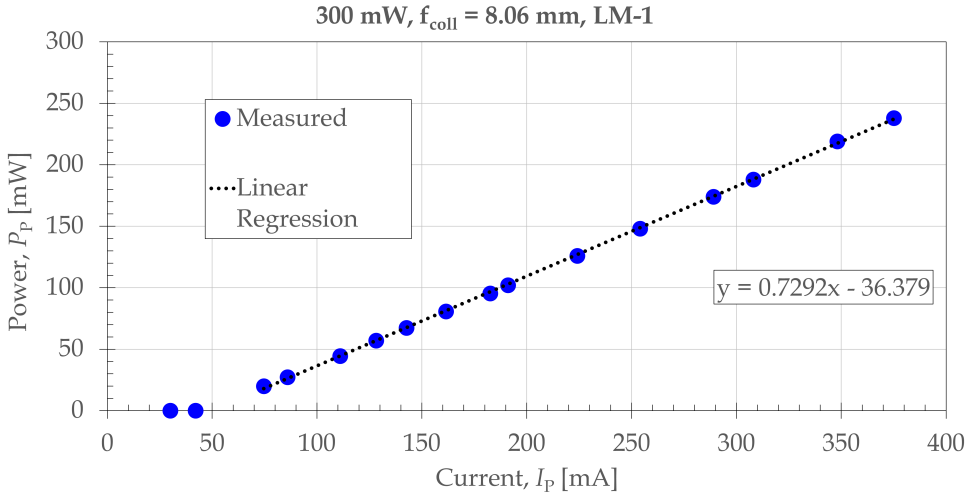

Figure 3.11: Power-to-current characteristic of the 300 mW diode laser with collimator $f_2 = 8.06$ mm. The blue dots represents the experimental data. The black dotted line represents the linear regression with its equation on the right.

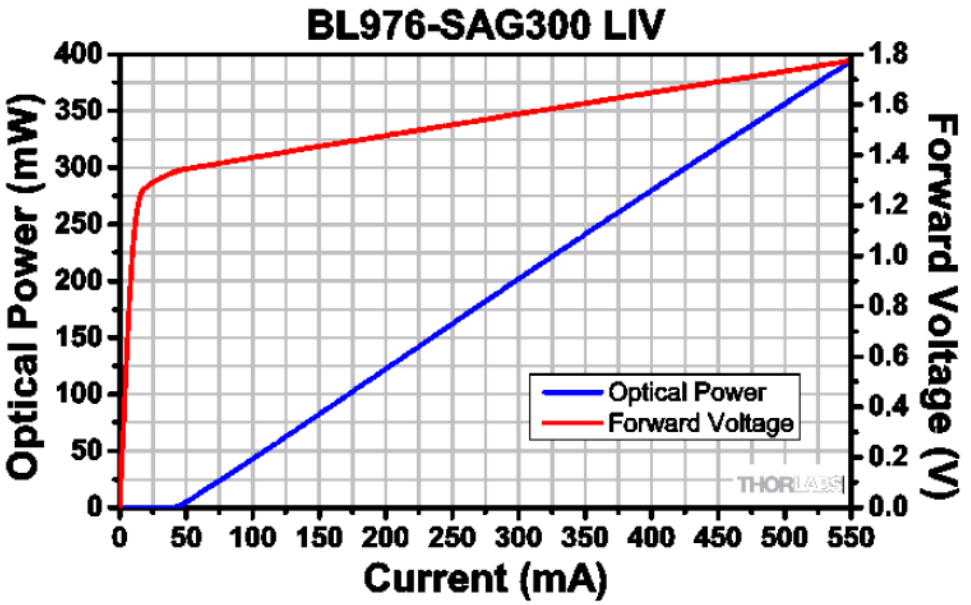

Figure 3.12: Power-to-current characteristic of the 300 mW diode laser measured by Thorlabs. From Thorlabs datasheet

3.3.2. 700 mW Diode Pump Laser

The power-to-current characteristic of the 700 mW diode laser was obtained in three different cases:

- without collimator using the Integrating Sphere power meter;
- with the collimator $f_1 = 4.55$ mm using both the LM-1 and the Integrating Sphere power meters;
- with the collimator $f_1 = 8.06$ mm using both the LM-1 and the Integrating Sphere power meters.

The first case is depicted in the Figure 3.13. Since the collimator was not attached to the fiber head, the power meter was placed right in front of the fiber in order to avoid power loss due to divergence of the beam, which can become larger than the sensor area. The characteristic is linear as expected, the threshold current is about 60 mA and the slope efficiency is equal to 0.6937 W/A. Exactly as said for the previous diode laser, since the maximum power is 700 mW, we stopped the measurement at a value of power smaller than this value, in order to avoid damages.

The second case is illustrated in Figure 3.14 with the presence of the collimator $f_1 = 4.55$ mm. In this graph a comparison between the two different power meter used is shown. The dotted black line represents the linear regression of the data collected with the Integrating Sphere power meter (whose equation is located above), the blue dots are the experimental data. The dotted burgundy red line represents the linear regression of the data collected with the LM-1 power meter (whose equa-

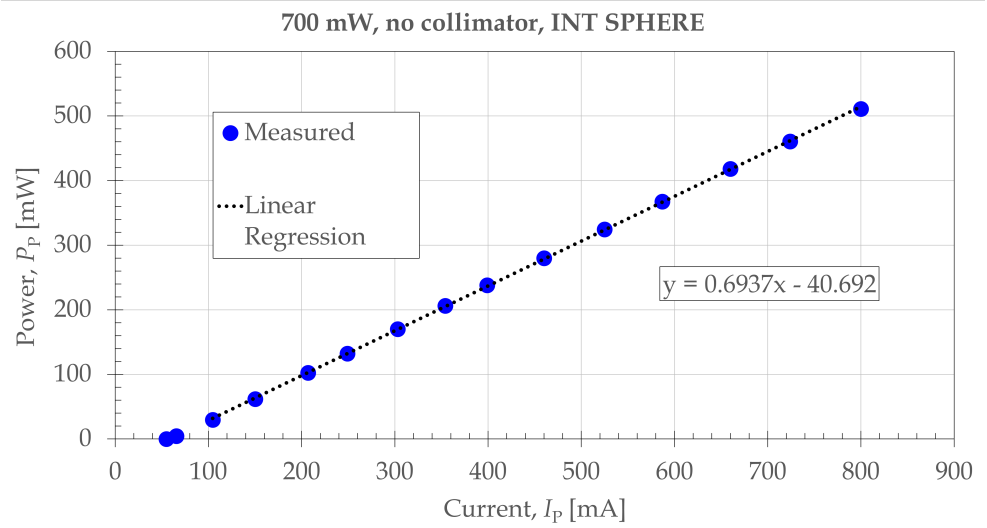

Figure 3.13: Power-to-current characteristic of the 700 mW diode laser without collimator.

tion is written below), the red dots are the experimental data. From the angular coefficients of the data it is possible to compare the two slope efficiencies, that are slightly different. This is because the Integrating Sphere measures incoming power better and more accurately.

The third case is illustrated in Figure 3.15 with the presence of the collimator $f_2 = 8.06$ mm. Also in this graph a comparison between the two different power meter used is shown. Even in this case, the slope efficiencies are slightly different for the same reason as before.

In the Figure 3.16 the power-to-current characteristic made by Thorlabs is shown in the blue line, as a comparison to the experimental data. The graphs are very similar, the threshold currents are almost the same and the typical values of the slope efficiency from the datasheet of the 700 mW diode laser in Figure 1.10 (Chapter 1) are in the range of $0.64 \div 0.68$ W/A. The η_{slope} measured are in this range only in the case of the measurement

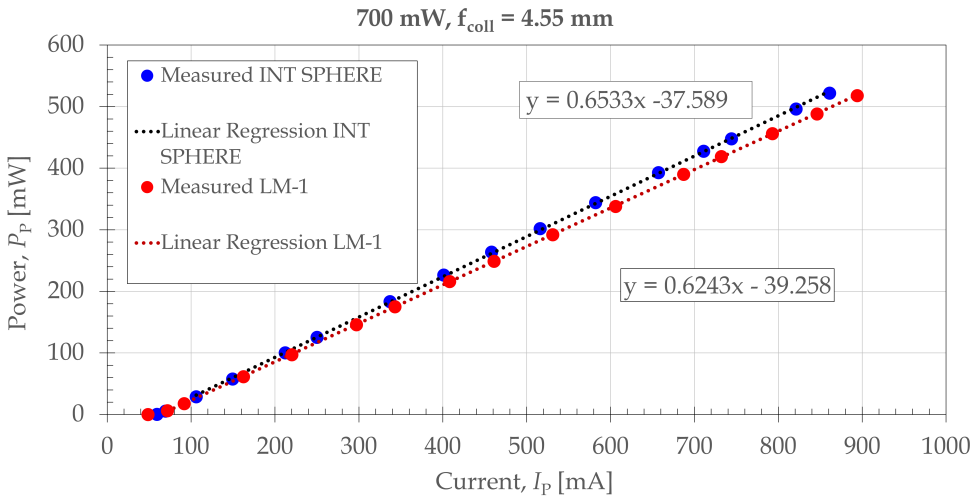

Figure 3.14: Power-to-current characteristic of the 700 mW diode laser with the $f_1 = 4.55$ mm collimator using the two different power meters.

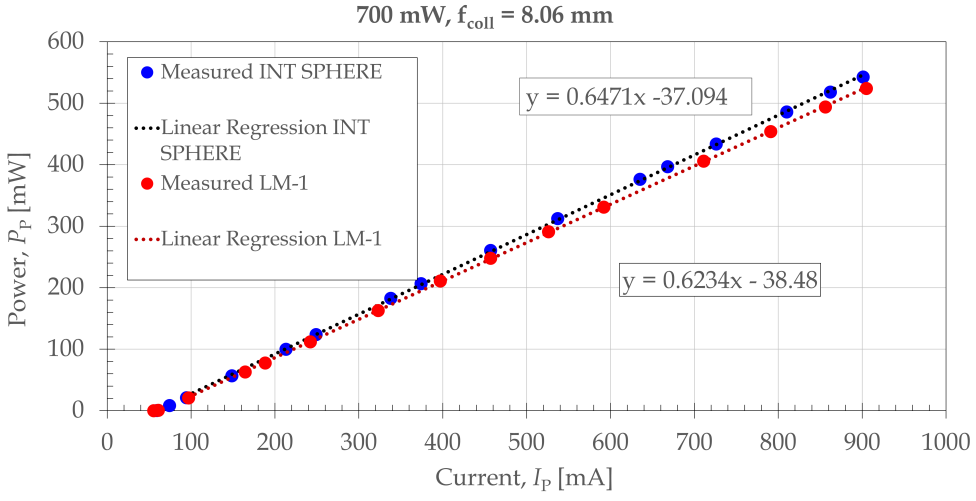

Figure 3.15: Power-to-current characteristic of the 700 mW diode laser with the $f_2 = 8.06$ mm collimator using the two different power meters.

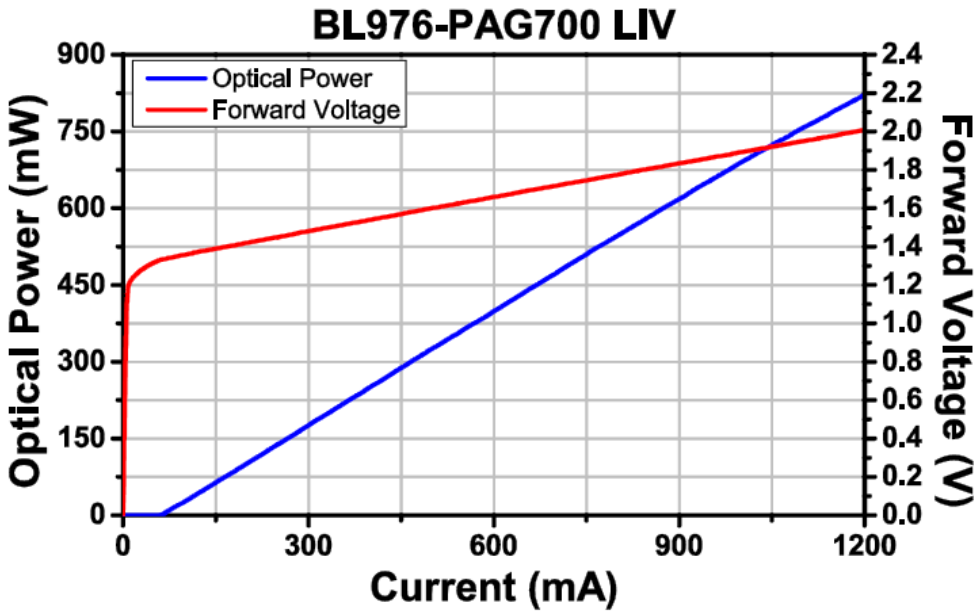

Figure 3.16: Power-to-current characteristic of the 700 mW diode laser measured by Thorlabs. From Thorlabs datasheet

collected by the Integrating Sphere. This is crucial and shows that the LM-1 is not ideal for estimations that include large values of power, close to the maximum power that can be measured with this instrument (1 W). In any case the characteristics measured does not follow perfectly the one presented by the manifacturer. This is due to the same facts showed for the 300 mW diode laser: probably wear and tear or poor measurements by the instruments.

Furthermore, the characteristic measured with the absence of the collimator, showed a larger value of slope efficiency with respect with those estimated after the collimators, allowing us to understand that these lenses produces a small loss of power.

4 | Yb-Er:glass solid state laser

In this chapter the measurements on the Yb-Er:glass laser are presented. First, the alignment and the setting of the components to turn on the lasing effect are exposed. After, discussions on cavity length and thermal lensing effect are illustrated. In the end of the chapter, measurements on the output power vs. pump power characteristic and beam waist measurements are shown.

This chapter is divided into the following sections:

4.1. Yb-Er:glass Laser Alignment

The first step in the actual construction of the Yb-Er laser is the alignment of the components. The alignment process requires the help of the visible red beam of a He-Ne laser, positioned in front of our components, and also of a suitable phosphor IR-detector card for non-visible beam detection (pump laser and Yb-Er:glass laser are out of the visible wavelength range). At the beginning we mounted the pump laser diode with the collimator $f_1 = 4.55$ mm on a holder and we translated it to have the red He-Ne laser beam in the center of the small lens, also tilting the holder in order to combine all the reflections with the He-Ne laser spot (with the help of a pin hole exactly as explained in the last section of the Chapter 1). Then we switched on the 300 mW pump laser and used the phosphor card to check the actual alignment between the He-Ne laser beam and the diode laser beam. We decided to use the 300 mW laser as pump because when we observed the 700 mW laser beam with the phosphor card, we realised that it was not perfect, it had an imperfection in the mode shape. This was a non-ideal condition for the pump laser, so we decided to use the less powerful of the two. During the project, a Professor of the Physics department resolved the problem by polishing the connector of the fiber and the tip of the fiber inserted in the connector itself, in order to remove a possible burning that modified significantly the spatial profile of the emitted radiation. The polishing was done by hands using appropriate cleaning cloths.

At this point, a lens with focal length $f_2 = 75$ mm was positioned at

an arbitrary distance ($\cong 4 \div 5$ cm, in practice) from the pump laser fiber, as the beam that had to be focused was collimated. The lens is plane-spherical, so care must be taken to place the curved side facing the direction of arrival of the pump beam (collimated, with $ROC \cong \infty$), in order to minimize optical aberrations. The alignment procedure was carried out as before, centering the red reflections of the He-Ne laser and then aligning the pump laser beam with the red beam using the phosphor card. After this, the active material was placed on a holder at 75 mm from the second lens, in order to have the beam focus inside the medium. Once again we translated and tilted the holder to center the He-Ne laser beam in the small area of the active material and to line up all the reflections with the red beam. The Yb-Er:glass is treated to have a highly reflective layer on one side, which is used as a flat input mirror. Once switched on the pump laser, the visible green fluorescence in the active material (effect due to spontaneous emission of visible photons from the - 2-photons absorption - excited atoms of the gain medium) was visible and the distance from the lens on the z-axis was changed in order to maximize this effect.

At this stage, the output mirror with $ROC = 50$ mm (whose properties are presented in the Chapter 1 in the "Resonant Cavity" subsection) was mounted on a mechanical holder with $x - y - z$ micrometer translators, at a distance between 49 and 53 mm as the cavity length should be (because $L_C \cong R_2$). Then the mirror was aligned and the reflections of the He-Ne laser was centered with the help of the $x - y - z$ translators. At this stage a last step was necessary: once switched on the pump laser,

its beam after the cavity appeared divided into two spots because of non-perfect alignment of the output mirror; using the $x - y - z$ screws and tilting the holder of the mirror we matched them. In the end we placed a high-pass filter with cutoff wavelength equal to 1400 nm right after the output mirror, in order to filter out the pump, and we checked with a phosphor card if the Yb-Er laser was on. The laser was on but it was necessary further micrometric translations in order to maximize the output power, corresponding to a better mode-matching between the pump and the laser. Done that, we changed the cavity length (moving the mirror position along the z-axis) in order to obtain a perfect TEM_{00} mode, checking it with the phosphor card. We realised that by shortening the cavity length, higher order transverse modes appeared. However, by increasing the length of the cavity, a TEM_{00} mode was revealed and remained spatially perfect, decreasing its intensity proportionally to the increase of the cavity length, until the switch off when the length became too long, reaching the instability condition of the resonator (the stability conditions of the resonator will be treated in the next section).

4.2. Cavity Length

The cavity length of a resonator can be calculated in a geometric way. An ABCD matrix, or ray transfer matrix, is a 2-by-2 matrix associated with an optical element which can be used to describe the element effect on a Gaussian laser beam [6]. This matrix completely characterizes the given optical element within the paraxial-ray approximation [15]. Once the matrices of the elementary optical elements are known, one can readily

obtain the overall matrix of a more complex optical system by subdividing it into these elementary components. This means that we can get the ABCD round trip matrix of a laser resonator, which is the overall matrix that fully describes the behaviour of an optical ray passing through the laser cavity, multiplying all the matrices corresponding to each single optical element of the cavity encountered by the laser beam in its round-trip way [15]. The determinant of each single matrix, representing an optical element of the cavity, is unitary: $(AD - BC) = 1$ and consequently the determinant of the overall ABCD round trip matrix is also unitary. The overall ABCD matrix, as already mentioned, is achieved by the multiplication of the ABCD matrices of the elementary components, noting that the order in which the matrices appear in the product is the opposite of the order in which the corresponding optical elements are crossed by the optical beam during its propagation. The cavity elements are: input flat mirror $R_1 = \infty$ (that is the flat interface of the active material), space propagation $L_{\text{am}} = 1$ mm through the active material with refractive index $n_{\text{am}} = 1.52$, space propagation L_{C} through air and output mirror $R_2 = 50$ mm. The resulting ABCD matrix is given by the following equation:

$$\begin{bmatrix} A & B \\ C & D \end{bmatrix} = \begin{bmatrix} 1 & 0 \\ -\frac{2}{R_2} & 1 \end{bmatrix} \begin{bmatrix} 1 & L_{\text{C}} - L_{\text{am}} \\ 0 & 1 \end{bmatrix} \begin{bmatrix} 1 & \frac{L_{\text{am}}}{n_{\text{am}}} \\ 0 & 1 \end{bmatrix} \begin{bmatrix} 1 & 0 \\ -\frac{2}{R_1} & 1 \end{bmatrix}. \tag{4.1}$$

A necessary condition for the correct functioning of the laser is its sta-

bility. In a purely geometric analysis, stability means that a ray injected into the optical system will stay at a finite distance from the axis even after many round trips. The properties of the resonator modes can vary strongly within a stability zone and also between different zones [6].

To this purpose it is necessary to calculate the maximum cavity length, L_C, for the laser to work in stability conditions. These calculations can be carried out by using the ABCD round trip matrix of the resonant cavity and imposing the following stability condition, as described in [15]:

$$\left|\frac{A+D}{2}\right| < 1\,, \tag{4.2}$$

from which two inequalities are derived. From one, the result can be neglected, since it specifies that the minimum cavity length is $L_C > 0.34$ mm (obviously this condition is always valid in our laser); while the other inequation is more important because its result shows us which is the condition to obtain the maximum resonator cavity length. In order to reach the limit condition of stability, it can be calculated as:

$$L_C < R_2 + L_{am}\left(1 + \frac{1}{n_{am}}\right)\,, \tag{4.3}$$

Substituting $R_2 = 50$ mm, $L_{am} = 1$ mm and $n_{am} = 1.52$ in the previous inequation the result is $L_C < 50.34$ mm, which is the maximum cavity length to maintain the stability of the resonator (without taking into to account any thermal lensing effect that will be described after). This is a theoretical result that has to be compared with the experimental

measurements.

We carried out two measurements of the cavity length range (within which the laser operates) with two different pump currents and hence at two different pump powers. The first with $I_{\text{pump}} = 243$ mA (that corresponds to $P_{\text{pump}} \cong 140$ mW), showed in the Figure 4.1; the second with $I_{\text{pump}} = 310.5$ mA (that corresponds to $P_{\text{pump}} \cong 180$ mW), represented in the Figure 4.2. These estimations were carried out measuring the output power of the laser (using the Integrating Sphere) while changing the position of the output mirror, rotating the z screw of its micrometric translator mounted on its mechanical holder.

Modifying the cavity length, the geometrical properties of the resonator change: the beam waist in the input mirror varies its spot size and position and so the mode matching does not remain the same. For this reason, in these measurements we will see the tranverse mode shape changing with the cavity length, showing also higher order modes.

The two graphs showed in the Figures 4.1 and 4.2 are different: the first reach a smaller output power and its cavity length stability range is shorter than the second one. Considering maximum output powers respectively equal to 13 mW and 19 mW we calculated the Full Width Half Maximum (FWHM) value of the curves, that are respectively ~ 0.35 mm and ~ 0.5 mm. Hence, the measurement carried out with higher pump power shows higher maximum output power and larger FWHM.

Both the curves show a peak where the power is at its maximum. On this peak and on the left side of the curve (where the cavity is shorter),

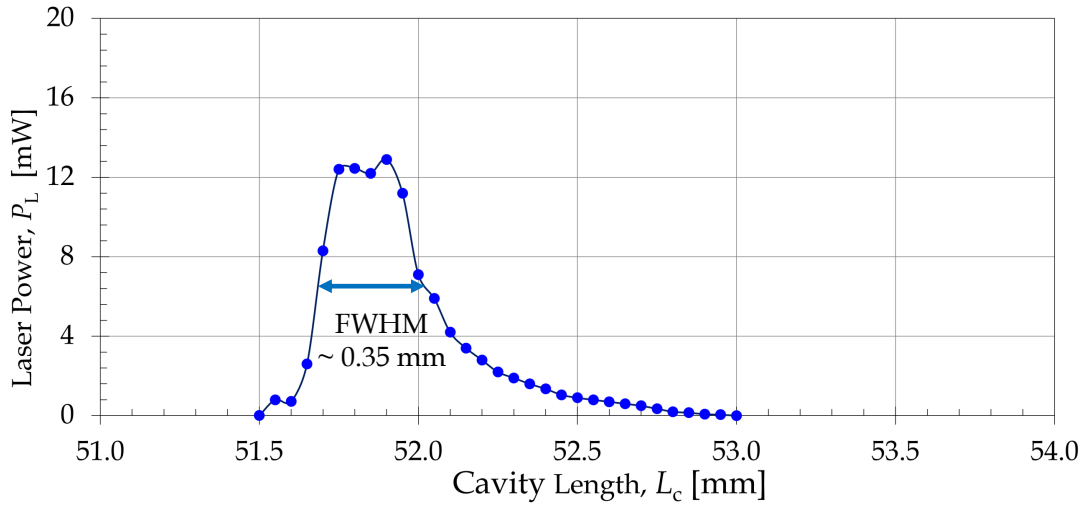

Figure 4.1: Output power vs. cavity length characteristic. $I_{\text{pump}} = 243$ mA.

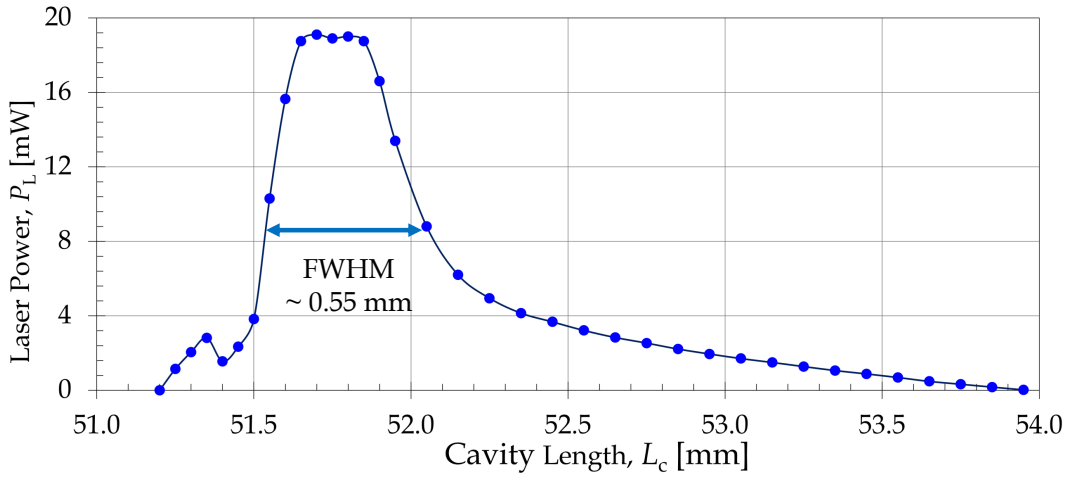

Figure 4.2: Output power vs. cavity length characteristic. $I_{\text{pump}} = 310.5$ mA.

observing the beam mode shape with the phosphor card, higher order transverse modes were present. On the right side of the curve, a clean TEM_{00} transverse mode could be seen with the phopshor card, remaining pure until the laser switch off, when the cavity became too long and the resonator was unstable, because the stability conditions, before mentioned, were not verified anymore. For this reason, in order to work with a perfect TEM_{00}, it is necessary to remain on the right side of the graph, with a cavity length approximately between 51.8 and 52.5 mm. This cavity length is bigger than the theoretical maximum L_C previously calculated (Equation 4.3: $L_C < 50.34$ mm). Furthermore, the change in pump power modified a lot the output power vs. cavity length graphs, not only regarding the maximum power achievable, but also in relation to the cavity length stability range, that depends on the resonator properties. This is probably due to the fact that a thermal lensing effect is present. The pump power heats the active medium, that acts as a this lens with focal length depending on the temperature, and so on the pump power. In this way, the thin lens modifies the parameters of the resonator, shifting or enlarging its stability range. The Equation 4.1 can be modified in order to take into account of the thermal lensing effect, adding to the multiplication a matrix that represents the thin lens in the active material. For this reason, the maximum L_C, calculated from the ABCD matrix, change its value [6]. The thermal lensing effect will be discussed deeply in the next section.

4.3. Thermal Lensing Effect

Thermal lensing is one of the most important effects that occur in propagating a high power laser beam in an absorbing medium.

The heat generated by longitudinal laser pumping causes a mostly transverse (but also longitudinal) temperature gradient in a solid material. Non-uniform temperature distributions have the effect of generating thermal stresses that, if too high, can irreparably damage a glass; in [16] it has been shown that it is precisely the resistance to thermal effects of the active medium that determines the maximum power obtainable from a laser. However, before sufficiently large pump powers can cause glass break, thermal effects can compromise the quality of the laser beam due to the induced thermal lensing and optical aberrations generated inside the active medium [6].

The thermal lens effect originates from non-radiative energy relaxation, that occurs in the active medium which is irradiated by a laser beam with a Gaussian intensity profile. Such effect is clearly observable when a high power laser beam propagates through an absorbing medium. In fact, a portion of the beam energy is absorbed by the material, which results in local heating of the medium and, consequently, in changing its local temperature. Since the refractive index of the medium is basically temperature dependent, but also depends on the glass type and on the wavelength, laser absorption results in the creation of a non-uniform refractive index profile in the active medium, which may also lead to a change in the laser beam radius and a related change in the optical

intensity of the laser beam on its axis [17]. The variation of the refractive index of the active medium, resulting from temperature effects, is indicated by dn/dT.

Moreover, longitudinal pumping is characterized by inhomogeneous heat distribution: the heat generated is more intense at the center of the pump (and also laser) spot because the beam intensity is stronger at that point. As a consequence of this, another phenomenon that must be considered is thermal expansion, where any material expands in reaction to being heated.

Both the variation in refractive index and thermal expansion, caused by the heat arising in the active medium of a laser cavity, contribute to the bulging of the glass end faces and consequently a lenslike optical element is formed in the glass. The increase of temperature causes stronger and more pronounced natural vibrations within the atoms. This increase in vibration pushes against the inter-molecular forces, allowing the atoms or molecules to become farther apart and the body to grow larger, i.e. less dense and hence typically with a lower refractive index. But the material expansion also turns out in a longer geometrical length of the medium crossed by the laser beam.

In our case study, since we are considering a Gaussian laser beam propagating through 1 mm of Yb,Er:glass, due to the active medium parameters, the effect is a focusing (positive) lens because a higher value of thermal expansion of this material overwhelms the negative coefficient of the variation of refractive index with respect to temperature.

It is possible to graphically represent the situation in which a lens is placed in the active material, as shown in Figure 4.3, by using the program "reZonator.

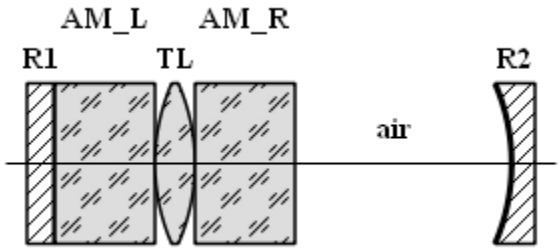

Figure 4.3: Scheme of the thermal lensing effect producing a thin lens in the active material. From "reZonator"

As a consequence of the formation of a thin lens in the active medium, in the case of a focusing lens, it is possible to have a second laser beam waist inside the cavity. In the case of a cold resonator, this waist matches the laser beam waist at the mirror R_1, since the active medium does not heat up and therefore the lens effect is not generated. With the presence of the thermal focal lens the second waist can be generated either just after the lens, so still in the active medium, or in the air section of the cavity, depending on the strength of the thermal lens effect: if $L_C \leq R_2$, the shorter the thermal focal lengths are, the more the second waist of the laser tends to move towards the output mirror R_2 in the air section of the cavity; on the other hand, if $L_C \geq R_2$, the second waist tends to move towards the opposite direction, i.e. towards the plane mirror, at shorter thermal focal lengths.

The Figure 4.4 is extracted from the study in [6], in which the thermal

lens f_t and the incident pump power are related and graphically illustrated. From this relation it can be found the value of f_t knowing the pump power provided by the diode later.

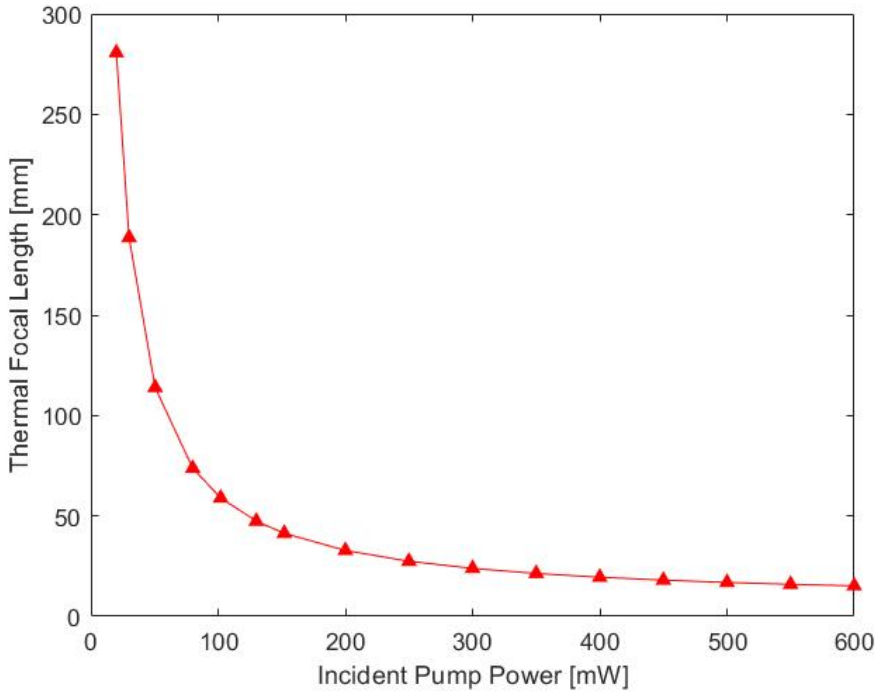

Figure 4.4: Thermal focal length with respect to incident pump power. From [6]

By using the program "reZonator" we consider the case with a fixed total cavity length $L_C = 52$ mm (including 1 mm length of the active medium), $R_2 = 50$ mm and $\lambda = 1550$ nm. In case of a cold resonator, i.e. at very low pump powers, the laser cavity is unstable. In fact, as derived before, the maximum length of a cavity in order to have a stable resonator is $L_C = 50.34$ mm.

We now consider incident pump powers for which the active medium

begins to heat up, generating thermal lensing effects that lead, in this case, to the resonator stability. In fact, analyzing the case with $P_{\text{pump}} = 200$ mW, which corresponds to a thermal focal length $f_{\text{t}} = 30$ mm, and with same L_{C} as before, differently from the previous case, now the stability conditions given in 4.2 are verified (because of the presence of the lens inside the active material). In the Figure 4.5, the "reZonator" simulation of the beam propagation through the cavity in this case is shown. The two dotted purple vertical lines indicate respectively the position of the thermal lens ($z = 0.5$ mm) and the end of the active material on the z-axis ($z = 1$ mm).

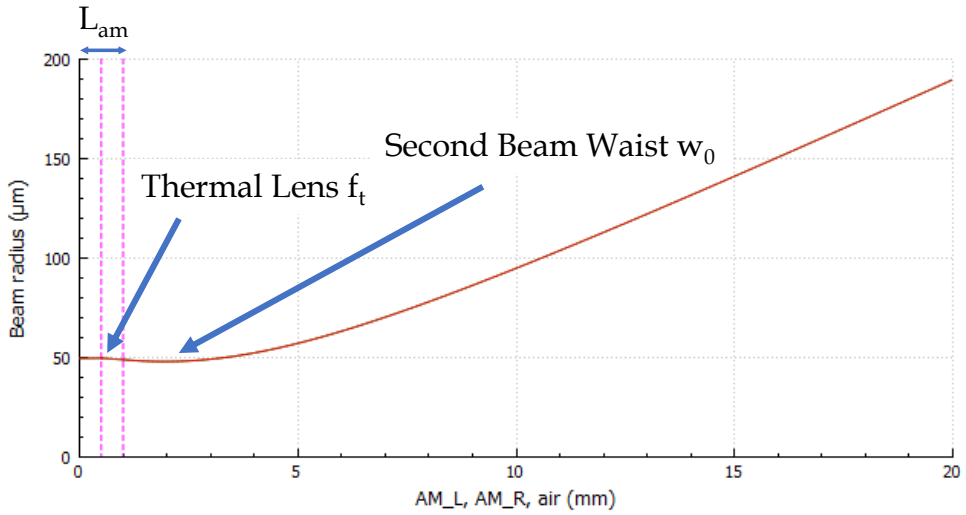

Figure 4.5: Simulation of beam propagation in a resonator with $L_{\text{C}} = 52$ mm, focal length of the thermal lens $f_{\text{t}} = 30$ mm placed in the center of the active medium (that is large 1 mm), output mirror $ROC = 50$ mm. From "reZonator".

The "second beam waist" indicated in the graph is the beam waist called w_0 that we will measure in the following sections, because it the one responsible of the beam divergence that is possible to measure from the

outside of the cavity.

We can say that since the best cavity length selected for our project are larger than 50.34 mm, the thermal lensing effect is always present (after the threshold pump power, hence when the Yb-Er laser is on) in our experiments and produces a lens in the active material that creates a second beam waist right after the input mirror. However, using the 300 mW pump laser, the thermal lens is not so powerful as if we used the other diode laser (with maximum output power equal to $\sim$ 700 mW) and it is hard to distinguish its effects from our possible small errors in the estimations and pratical measures. A change by 1 or 2 mm in the spot size or in the position of the beam waist can be surely the consequence of imperfect measurements of the spot sizes in far field, and hence of the divergence angle and so on. Small errors causes large changes in the final calculations. Much stronger effects of thermal lensing are visible with pump powers equal to 600 or 700 mW, when the heat in the active medium arises so much and modifies significantly the cavity parameters.

4.4. Output Power vs. Pump Power Characteristics

Proceeding with the characterization of the Yb-Er laser, we knew that an important property of every laser is the variation of the output power with respect to the variation of pump power. Also the slope efficiency η

of this characteristic is crucial and it can be calculated according to:

$$\eta = \frac{\Delta P_{\text{out}}}{\Delta P_{\text{pump}}}\,, \tag{4.4}$$

where P_{out} is the output power of the Yb-Er laser and P_{pump} is the pump power coming from the laser diode. Usually the efficiencies are expressed as a percentage, so the value from the formula must be multiplied by 100. Since while measuring the output power, we could only observe the current provided to the diode (using the multimeter connected to the laser current driver) and not the actual pump power, we derived it from the current, thanks to the measurements made in the Chapter 3.

Considering the pump power threshold $P_{\text{pump,th}}$ needed to switch on the solid state laser, the equation of the slope efficiency becomes:

$$\eta = \frac{P_{\text{out}}}{P_{\text{pump}} - P_{\text{pump,th}}}\,. \tag{4.5}$$

From the literature [18], a good range of values for the slope efficiency η for this kind of laser is $15 \div 30\%$.

We measured the output power vs. pump power of the Yb-Er:glass laser using four different cavity lengths, in order to see how the laser behaved changing one of its most important parameter. The tested cavity lengths were: 52 mm, 51.9 mm, 51.8 mm and 51.7 mm. For the power measurements we always used the Integrating Sphere as it was the best power meter available, as confirmed also by our previous experiments.

In the Figure 4.6 the output power vs. pump power characteristic with

a cavity length equal to 52 mm is shown. Having this length, a perfect TEM_{00} transverse mode came out from the cavity. Considering the graphs of the cavity lengths above (Figures 4.1 and 4.2), $L_C = 52$ mm is on the right side of the curve, where we have single mode but not maximized output power. The threshold pump power $P_{pump,th}$ is about 43 mW and after an initial deviation, the output power starts to increase linearly with respect to the pump, showing a slope efficiency η equal to the angular coefficient of the linear regression. In this case, in the linear region above, it is about 10.7 %, a result too small considering the range of values before mentioned.

From $P_{pump} \cong 130$ mW to $P_{pump} \cong 170$ mW the slope efficiency is about 19.2 %.

In the Figure 4.7 the output power vs. pump power characteristic with a cavity length equal to 51.9 mm is shown. The cavity length was shortened, the mode remained a TEM_{00} and the slope efficiency increased, since we went closer to the peak of power in the graphs 4.1 and 4.2. The threshold pump power $P_{pump,th}$ is about 45 mW and the slope efficiency increased, becoming about 15.7 %. The characteristic in its central part increases rapidly than before, with a η equal to 22.9 %.

In the Figure 4.8 the output power vs. pump power characteristic with a cavity length equal to 51.8 mm is shown. The cavity length was shortened again, the mode remained a TEM_{00}, the slope efficiency at high pump powers was approximately the same ($\eta = 15.4$ %) as before but what changed was the threshold pump power and the shape of the curve in the

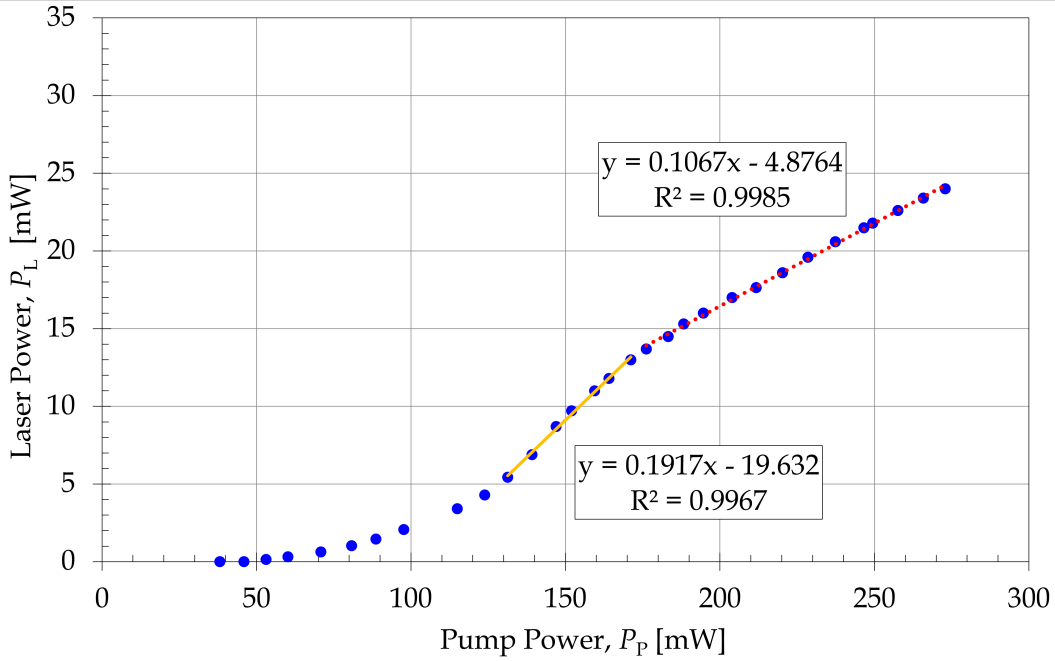

Figure 4.6: Output power vs. pump power characteristic. $L_C = 52$ mm.

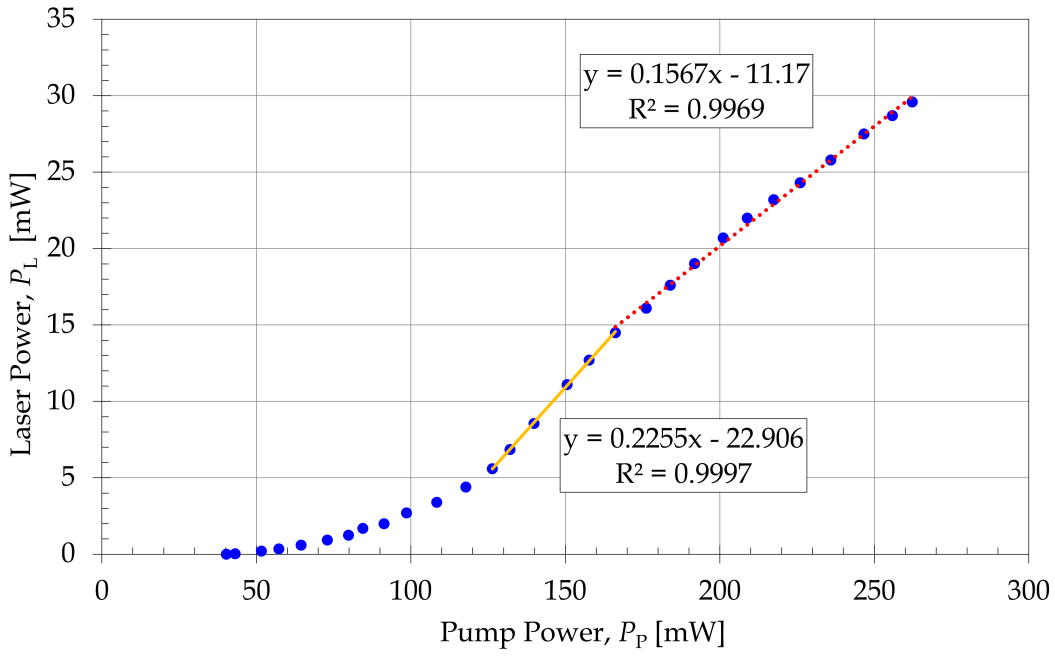

Figure 4.7: Output power vs. pump power characteristic. $L_C = 51.9$ mm.

central part of the graph. One can see that the output power increases more steeply and then returns to the same slope efficiency as before. The η of this steeper part of the characteristic is much higher than before and is equal to 26.7 %. The threshold pump power $P_{\text{pump,th}}$ is about 50 mW, so the laser switches on after, its output power increases faster but at the end approaches the same η as before.

In the Figure 4.9 the output power vs. pump power characteristic with a cavity length equal to 51.7 mm is shown, note that the y-axis scale is different from the other graphs and the maximum output power is set to 10 mW. Considering the graphs of the cavity length stability range in the Figures 4.1 and 4.2 showed in the previous section, we can understand that with this L_{C} we are in the left side of the curves, where the higher order modes appeared. In fact the transverse mode was not a TEM_{00} but presented some rings and changed its shape during the measurement, while increasing the pump power.

The characteristic is really strange: the power increases linearly only with low pump powers and then decreases and increases in a non-ideal way. This was probably due to the excitation of higher order modes with very large beam divergence and then larger spot size than the radius of the power meter sensor area. In this way the output power could not be measured perfectly. Furthermore, we noticed that increasing the pump power, more and more higher order modes appeared; also this could explain the strange shape of the characteristic.

In the end it was clear that, watching the graphs 4.1 and 4.2, the best

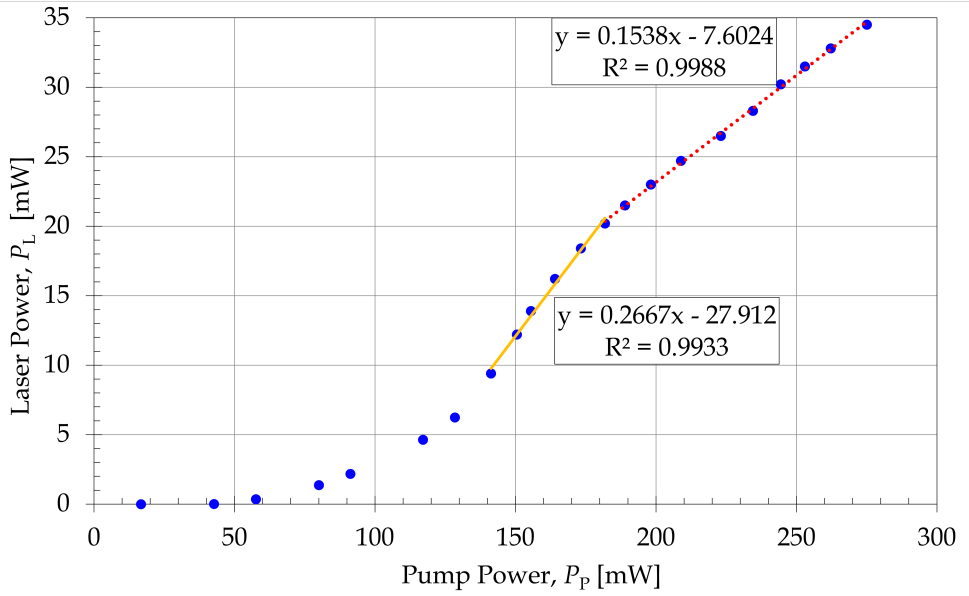

Figure 4.8: Output power vs. pump power characteristic. $L_C = 51.8$ mm.

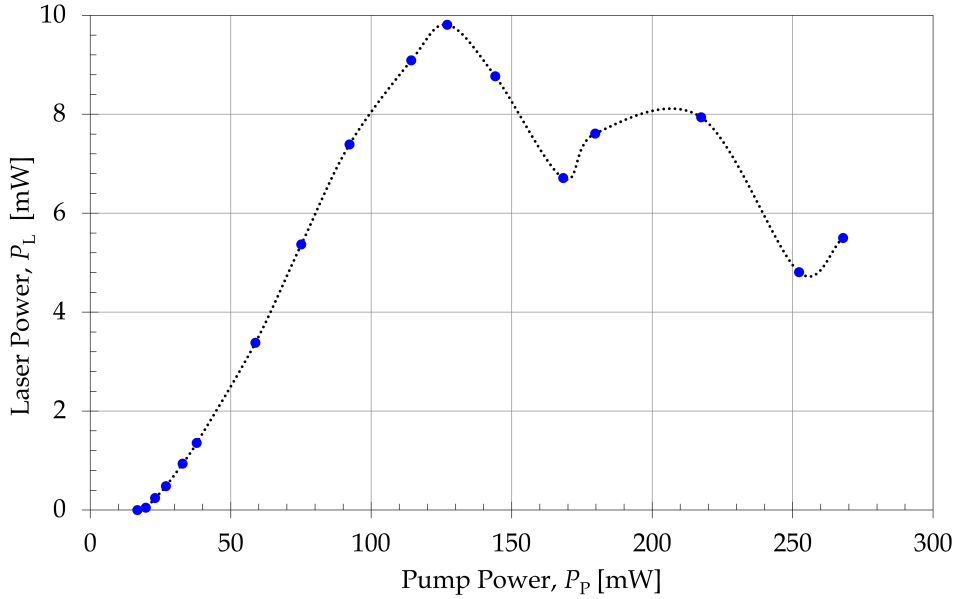

Figure 4.9: Output power vs. pump power characteristic. $L_C = 51.7$ mm. Note that the y-axis scale is different from the other graphs and the maximum output power is set to 10 mW.

cavity lengths were those close to the peak of output power, but on its right side, in order to avoid the excitation of higher order transverse modes.

4.5. Beam Waist Measurements with Knife-Edge Technique

In this section, the position z_{waist} and the spot size of the beam waist w_0 of the Yb-Er:glass laser are estimated. Exactly as has been done for the He-Ne laser in the Chapter 3, the w_0 is calculated indirectly from the divergence angle θ_{d} of the laser beam. In order to calculate θ_{d}, spot sizes $w(z)$ measurements at different distances in far field are made by applying the Knife-Edge technique. In the graph representing the spot sizes with respect to z, a linear regression is superimposed on the points and its angular coefficient represents the divergence angle.

We calculated the position and the spot size of the laser beam waist in three different cases:

1) $L_{\text{C}} = 51.8$ mm, $I_{\text{pump}} = 182$ mA and $P_{\text{out}} = 17.53$ mW;

2) $L_{\text{C}} = 52.2$ mm, $I_{\text{pump}} = 100$ mA and $P_{\text{out}} = 2$ mW;

3) $L_{\text{C}} = 52.2$ mm, $I_{\text{pump}} = 349$ mA and $P_{\text{out}} = 18.51$ mW after a lens $f_1 = 100$ mm in $z = 171.5$ mm.

For each case we measured more than three $w(z)$ in far field, we extracted θ_{d} from the angular coefficient of the linear regression passing through the points and then we calculated: z_{R}, according to the Equation 3.5, w_0,

according to the Equation 3.8 and z_{waist} (the position of the beam waist on the z-axis) thanks to "Gaussian Beam" simulations. Knowing that the beam waist should be on the input mirror R_1, the spot sizes measured $w(z)$ were confirmed with the Equation 3.7, valid only in far field. At the end we used the program "Gaussian Beam.exe", as it has been done previously for the pump lasers, in order to confirm our experimental data and calculations.

The last two cases were also a test to reveal the presence of the thermal lensing effect. We measured w_0 in the cases of low and high pump power in order to see if it changes proportionally to the heating of the active material. We couldn't reach high pump power because for this project we used the 300 mW pump laser.

An example of a $w(z)$ measurement carried out for the first case before mentioned, is represented in the Figure 4.10. The position of the blade was $z = 179.5$ mm (considering $z = 0$ mm the position of the input mirror of the active material) and the spacing between two output power measures, in height, was $\Delta h = 0.4$ mm. We used the Knife-Edge technique and we superimposed the Gaussian fitting curve, exactly as for the He-Ne laser in the Chapter 3. All the fitting were perfect hence the mode of the beam was TEM_{00} in all the cases.

Case 1. The first case is represented in the Figure 4.11 and the experimental data are shown in the Table 4.1, where z is the position of the the blade for the Knife-Edge, $w(z)$ is the spot size measured, Δz is the displacement between two adiacient $w(z)$, Δw is the difference in spot

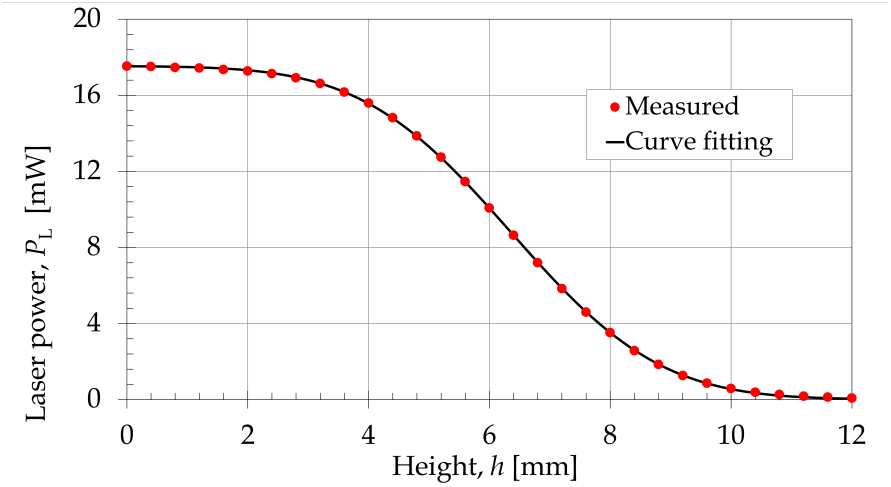

Figure 4.10: Example of a $w(z)$ measurement using the Knife-Edge technique. $L_C = 51.8$ mm, $I_{pump} = 182$ mA and $P_{out} = 17.53$ mW, $z = 179.5$ mm.

size between two adiacient $w(z)$ and θ_d is the divergence angle. The characteristics of the laser was: $L_C = 51.8$ mm, $I_{pump} = 182$ mA and $P_{out} = 17.53$ mW. θ_d is equal to 22.14 mrad, from the equation of the linear regression, z_R is equal to 0.99 mm (therefore the positions where we placed the blade for the estimations were in far field) and so from the formulas, w_0 become equal to 22.04 µm while its position is in the active material, in $z = 1$ mm. It is not perfectly on the input flat mirror probably because of the thermal lensing effect or because of small errors during the experimental measurements. All the results were confirmed by "Gaussian Beam" simulations.

$[mm]$ z	$[\mu m]$ $w(z)$	$[mm]$ Δz	$[\mu m]$ Δw	$[mm]$ θ_d
179.5	3893			
184.5	4001	5	107.396	21.47
189.5	4115	5	114.078	22.82

Table 4.1: Data of the Knife-Edge measurements on the laser with L_C = 51.8 mm, I_{pump} = 182 mA and P_{out} = 17.53 mW.

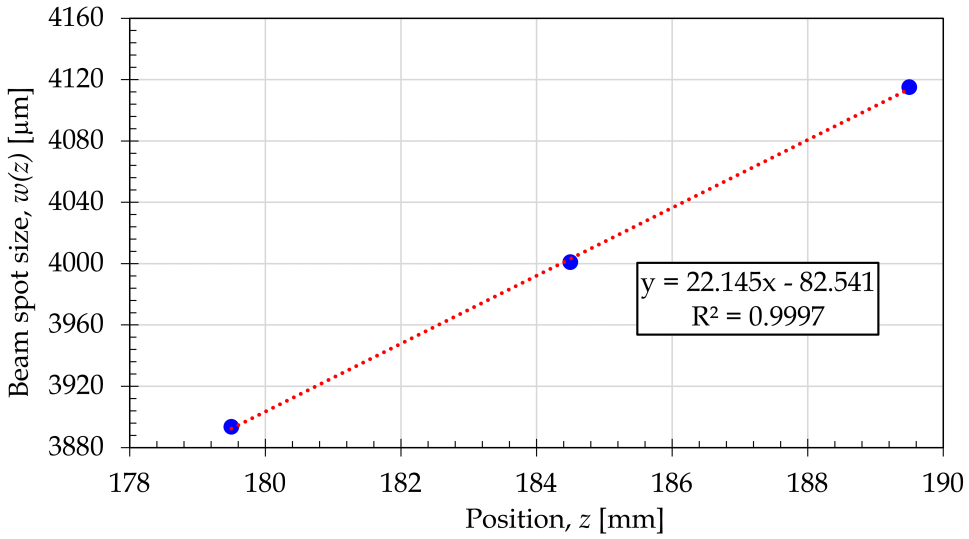

Figure 4.11: $w(z)$ measurements with linear regression and its equation. L_C = 51.8 mm, I_{pump} = 182 mA and P_{out} = 17.53 mW.

Knowing from the datasheet in the Chapter 1 that the mode field radius of the 300 mW diode laser fiber (the pump laser) is equal to 2.85 µm, it is possible to calculate the spot size of the beam after the collimator. Having that we can calculate the pump beam radius in the focus of the 75 mm lens in order to estimate the spot size of the beam waist of the pump laser in the active material and compare it with the one of the Yb-

Er laser. The result of the calculation is $w_{0,\text{pump}} \cong 50\,\mu\text{m}$. In order to have a perfect mode matching, the two beam waist must have the same spot size. In this case the mode matching is not ideal because the two spot sizes are quite different, one is almost twice the size of the other.

Case 2. The second case is represented in the Figure 4.12 and the experimental data are shown in the Table 4.2. The characteristics of the laser was: $L_\text{C} = 52.2$ mm, $I_\text{pump} = 100$ mA and $P_\text{out} = 2$ mW.

$[mm]$ z	$[\mu m]$ $w(z)$	$[mm]$ Δz	$[\mu m]$ Δw	$[mm]$ θ_d
164	1634			
170	1690	6	56.360	9.393
174	1733	4	42.634	10.66
179	1776	5	42.938	8.588

Table 4.2: Data of the Knife-Edge measurements on the laser with $L_\text{C} = 52.2$ mm, $I_\text{pump} = 100$ mA and $P_\text{out} = 2$ mW.

We tried to measure the spot size of the beam waist at low power in order to compare it with the next measurement, at high power, and see if the thermal lensing effect appears, modifying the spot size and the position of the beam waist (together with the beam divergence). θ_d is equal to 9.549 mrad, from the equation of the linear regression, z_R is equal to 5.35 mm and so from the formulas, w_0 is equal to 51.1 µm while its position is on the input mirror: $z = 0.1$ mm. All the results were confirmed by "Gaussian Beam.exe" simulations. In this case the mode matching is

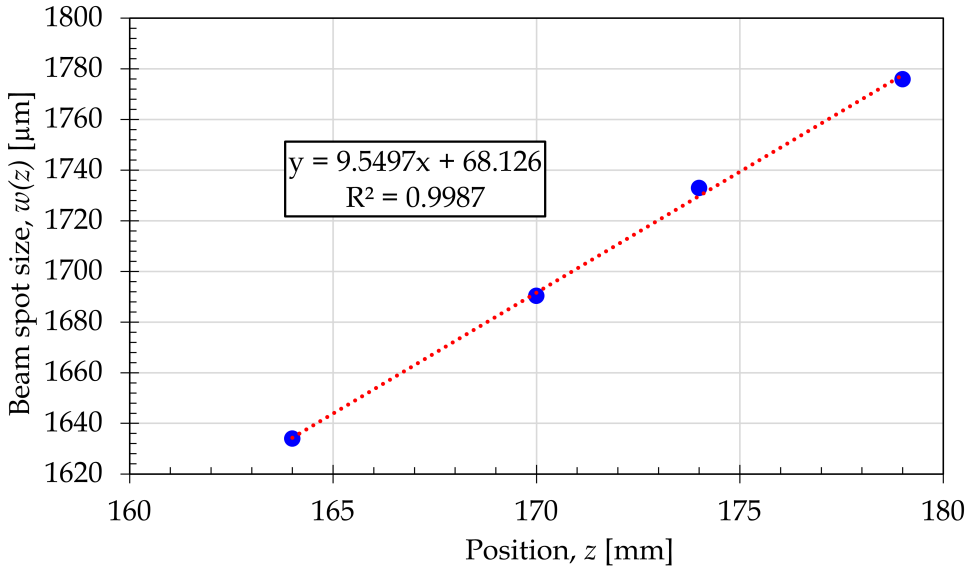

Figure 4.12: $w(z)$ measurements with linear regression and its equation. $L_C = 52.2$ mm, $I_{pump} = 100$ mA and $P_{out} = 2$ mW.

almost perfect, since the spot size of the beam waists of the pump and the Yb-Er laser are quite similar.

Case 3. The third case is represented in the Figure 4.13 and the experimental data are shown in the Table 4.3. The characteristics of the laser was: $L_C = 52.2$ mm, $I_{pump} = 349$ mA and $P_{out} = 18.51$ mW with a lens $f_1 = 100$ mm in $z = 171.5$ mm. Since we increased the power, we expected an increase of the Rayleigh distance due to the thermal lensing effect. Because of this, in order to be in far field we had to place the blade for the Knife-Edge too far away and the beam could have become too large to be measured by the small area of the power meter. It could have become even larger than a collecting lens placed after the positions of our measurements. For this reason we placed a lens with focal length $f_1 = 100$ mm in the position $z = 171.5$ mm, in this way a

new beam waist was created (we checked the approximate position of the focus with the phosphor card and we selected suitable positions for the Knife-Edge measurements). We exploited it measuring spot sizes with the Knife-Edge technique in four positions after the lens, we calculated the new Rayleigh distance (z'_{R}), confirming that the previous positions were in far field, the new divergence angle (θ'_{d}) together with the new beam waist spot size (w'_0) and position (z'_{waist}). Then, with the formulas applied in the Chapter 3 for the He-Ne laser, we calculated the real θ_{d}, z_{waist} and w_0 of the Yb-Er laser. It is clear from the Figure 4.13 that the spot sizes decrease with respect to z just because we were after the lens, and we were approaching the second beam waist, as can be seen in the simulation showed in the Figure 4.14. For this reason the second divergence angle became negative, knowing that it was important only its absolute value.

$[mm]$ z	$[\mu m]$ $w(z)$	$[mm]$ Δz	$[\mu m]$ Δw	$[mm]$ θ_{d}
182	1602			
207	1415	25	−187.549	−7.50
232	1248	25	−166.045	−6.64
257	1071	25	−177.582	−7.10

Table 4.3: Data of the Knife-Edge measurements on the laser with $L_{\mathrm{C}} = 52.2$ mm, $I_{\mathrm{pump}} = 349$ mA and $P_{\mathrm{out}} = 18.51$ mW after a lens $f_1 = 100$ mm in $z = 171.5$ mm.

The measured and calculated results are shown in the Table 4.4.

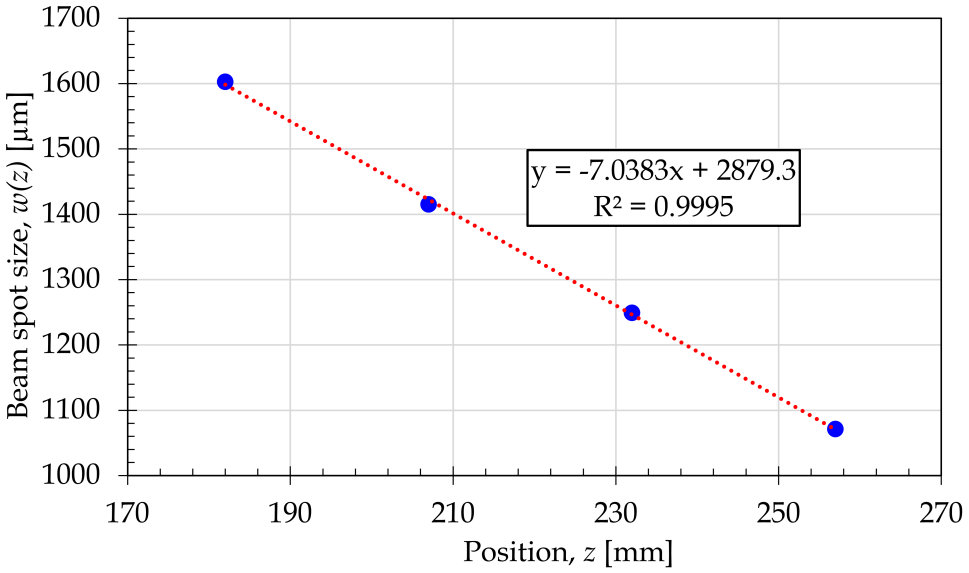

Figure 4.13: $w(z)$ measurements with linear regression and its equation. $L_C = 52.2$ mm, $I_{pump} = 349$ mA and $P_{out} = 18.51$ mW after a lens $f_1 = 100$ mm in $z = 171.5$ mm. Note that the $w(z)$ decrease with respect to z because the presence of the focusing lens placed before the measurements that created a new beam waist.

$[mrad]$ θ'_{d}	$[mm]$ z'_{R}	$[mm]$ z'_{waist}	$[\mu m]$ w'_0	$[mrad]$ θ_{d}	$[mm]$ z_{R}	$[mm]$ z_{waist}	$[\mu m]$ w_0
7.04	9.85	413.7	69.33	9.838	5.04	0.94	49.6

Table 4.4: Measured (after the lens) and calculated (before the lens) results of the third case.

In this last case the mode matching is perfect, since the w_0 of the laser is 49.6 µm and the one of the pump in the active material is about 50 µm.

In the Figure 4.14 the third case data and simulation from "Guassian beam" are shown. Above, the results of the simulation can be seen and compared with those calculated. They coincide almost perfectly.

The thermal lensing effect seems to appear because comparing the spot size of the beam waist in the last two cases, it becomes smaller and its position is not on the input mirror when we increase the pump power. It is about 1 mm inside the cavity (in the air between the mirrors), but this displacement is too small to confirm the presence of the effect, since the power provided to the active material is too low. In order to prove the presence of this effect, the 700 mW pump laser should be used, providing much more power and heating up significantly the active medium.

Optics	Position (mm)	Relative position (mm)	Properties	Waist (µm)	Waist position (mm)	Rayleigh range (mm)	Divergence (mrad)
Input beam	0.937874		n = 1, M^2 = 1	49.0275	0.937874	4.92592	9.95264
Lens	171.5	170.562	f = 100 mm	69.3126	412.532	9.84538	7.04

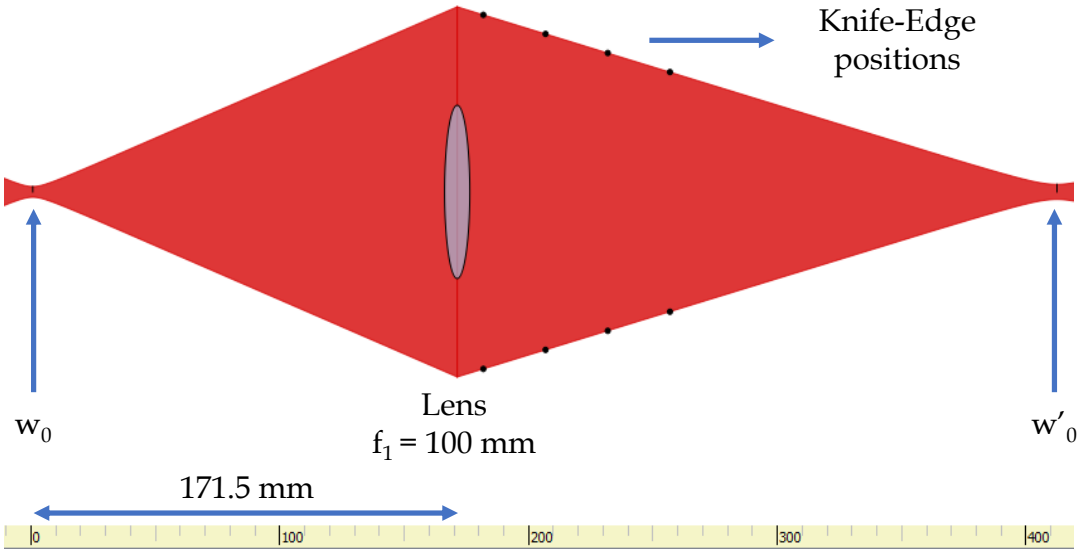

Figure 4.14: Data and simulation of the third case measurement. From "Gaussian Beam.exe"

5 | Relative Intensity Noise Measurements

In this chapter Relative Intensity Noise measurements on the pump laser diode and the Yb-Er:glass laser are presented. First the RIN theory is reviewed, then the instruments used together with the set up of the measurements are exposed. In the end the experimental results and the possible solutions for RIN reduction are illustrated and discussed.

This chapter is divided in the following sections:

5.4.2 Compact and Monolithic Laser Design.

5.1. RIN Theory

In order to optimize the laser performance, a goal is to reduce the Relative Intensity Noise (RIN), which is typical for a solid state laser like the Yb-Er:glass laser. The RIN describes the time instability in the power level of a laser and it is produced by cavity vibration, fluctuations in the laser gain medium, or simply by transferred intensity noise from the pump source. RIN typically peaks at the relaxation oscillations (RO) frequency (f_{RO}) of the laser and then falls off at higher frequencies where it becomes shot-noise limited. Typical values of relaxation oscillations frequency for solid state lasers are in the range from a few kHz to a few MHz [7]. The relaxation oscillations phenomenon results from the interplay between the population inversion and the intracavity laser intensity. It is present in any class-B laser, i.e. where the population inversion lifetime is longer than the cavity photon lifetime [19], as in the Yb-Er:glass laser.

According to "EN ISO 11554 : 2003" [20], the Relative Intensity Noise is defined as:

$$RIN = \frac{\langle \Delta P(t)^2 \rangle}{P_0^2}\,, \tag{5.1}$$

where P_0 is the average optical power (typically over a defined time of observation) and $\Delta P(t)$ represents the fluctuations of optical power. Optical power, P_{opt}, is detected with a fast photo detector (with i as the photo current), and thus the optical power fluctuations are transformed

into electrical power (P_{E}) fluctuations which are measured with an ESA (electrical spectrum analyzer). The detected electrical power (P_{E}) is proportional to squared optical power:

$$P_{\mathrm{E}} \propto i^2 \propto P^2{}_{\mathrm{opt}}\,, \tag{5.2}$$

so the RIN can be expressed through the corresponding electrical values:

$$RIN\,[1/Hz] = \frac{\Delta P_{\mathrm{E}}}{P_{\mathrm{E0}}}\,, \tag{5.3}$$

where ΔP_{E} is the overall noise, measured in power spectral density per Hertz and P_{E0} the average electrical power. Usually the RIN is measured in dB/Hz so:

$$RIN\,[dB/Hz] = 10\,log_{10}(RIN\,[1/Hz])\,. \tag{5.4}$$

5.2. Measurements Set Up

Our goal was to measure the Yb-Er:glass laser RIN at low frequencies (from a few Hz to a few MHz) in order to see if it was low enough to use this laser as a ϕ-OTDR source. It was measured in the laboratory both on the pump laser diode BL976-SAG300 and on the Yb-Er:glass laser. Regarding the Yb-Er laser RIN, we expect a more or less flat spectrum (knowing that the vibrations of every single component were present and could generate high peaks) with a peak at the relaxation oscillations

frequency (at about a hundred of kHz) after which the RIN should fall off (with slope $\cong -60$ dB/Hz per decade) reaching very small values (where it becomes shot-noise limited). Instead, from the pump laser diode we expect a flat RIN spectrum without high peaks. The measurement on the pump was done in order to compare its spectrum with the one of the solid state laser; in this way it was possible to see if the noise was transferred from the pumping process or if it was instead originated by the laser structure itself, for example from the cavity structure, from the vibrations of the components or from the energy-trasfer process in the active material [21].

For all the RIN measurements we used three different instruments: a photodiode, an oscilloscope and an electrical spectrum analyzer (ESA).

The photodiode available in the laboratory was a 125-MHz low noise photoreceiver made by New Focus (Model FS-1811. It contains an InGaAs/PIN photodiode followed by a low-noise transimpedance amplifier (transimpedance gain equal to 40 V/mA in the DC-coupled version) acting as a pre-amp with a compensating amplifier as the output stage. The wavelength range is $900 - 1700$ nm, the typical 3-dB bandwidth is 125 MHz (DC version), the output impedance is $50\,\Omega$ and the detector diameter is 0.1 mm. At 1550 nm the saturation power is $55\,\mu$W and the responsivity is 1 A/W. Since the saturation power the photodetector is relatively small, the maximum power of the detected beam had to be low to not damage the instrument. In order to stay in safe conditions, we connected the PD the an oscilloscope and we placed a $50\,\Omega$ resistance in parallel, in order to measure the exact voltage output when detecting a

laser beam. The Physics colleagues warned us to stay below 1 V, so as to not cause damage to the instrument.

The digital oscilloscope used was a RTB2004 made by Rhode & Schwarz. It had 4 input channels analog bandwidth (-3 dB) > 300 MHz, lower frequency limit (-3 dB) < 2 Hz, rise time (10 % to 90 %, calculated) < 1.15 ns, vertical resolution equal to 10-bit, up to 16-bit with high-resolution decimation mode and maximum realtime sampling rate equal to 2.5 Gsample/s

The spectrum analyzer used for the RIN estimations was a E4445A PSA Series made by Agilent (available thanks to the Physics Department colleagues). It had frequency range 3 Hz $\div$13.2 GHz (DC coupled) with 2 Hz resolution and resolution bandwidth (RBW) Range (-3.01 dB bandwidth) from 1 Hz to 3 MHz (10 % steps) 4, 5, 6, 8 MHz.

A computer was connected to the instrument thank to a GPIB-USB-B made by National Instruments; in this way it was possible to use a matlab code (also available thanks to the Physics Department colleagues) to control the spectrum analyzer from the PC and extract the RIN measurements, selecting the bandwidth of the analysis and the number of averages made by the instrument.

For correct RIN measurements it was necessary to input in the control program the average voltage (V_{ave}), that we measured thanks to the oscilloscope and the parallel 50 Ω resistance. Then we had to input the number of averages that the analyzer had to compute while measuring, this value initially was set to 10 for the whole bandwidth. The bandwidth

originally was set to 100 MHz from 1 Hz to 100 MHz but in the code it was divided into different frequency decades thanks to a cycle in which the integer incremental element was the exponent k of $f_{\text{start}} = 10^{k-1}$ and $f_{\text{stop}} = 10^{k}$. The exponent k varied from $k = 1$ to $k = 8$ hence the ranges was $10^0 \div 10^1$ Hz, $10^1 \div 10^2$ Hz ecc. until 10^8 Hz. For every acquisition bandwidth (hence in every cycle) 601 points was measured, equally spaced in frequency. In this way the frequency was analyzed in a logarithmic way, allowing us to plot the RIN in dB/Hz with respect to frequency, represented in logarithmic scale. The resolution bandwidth (RBW) was not the same for every frequency decade analyzed, it was modified by the Physics colleagues in order to avoid artifacts in the connection points between two adjacent acquisition bandwidths. From the first to the last frequency decade respectively, the RBW was set to: 1 Hz, 1 Hz, 8.2 Hz, 82 Hz, 820 Hz, 8.2 kHz, 82 kHz, 820 kHz.

In general, the spectrum analyzer takes a long time to measure the RIN in the low frequencies, because the measurement time is inversely proportional to the minimum frequency analyzed, and in particular to the requested RBW, furthermore the measurements in every range had to be repeated for the number of averages selected. Thus for faster measurements we modified the code and cut the first frequency range ($1 \div 10$ Hz) and the last two ($1 \div 100$ MHz). These were not so important ranges for our purposes, because we wanted to analyze the spectrum from the lowest frequencies until the ones immediately after the RO peak. In this way we could also increase the number of averages significantly. Our modified bandwidth span was from 10^1 Hz (10 Hz) to 10^6 Hz (1 MHz),

divided into 5 frequency ranges using the same cycle as before but with k varying from 2 to 6.

The RIN measurements were faster at high frequencies, so for these frequency ranges the number of averages could be also increased to 400 without enlarging so much the overall measurement time. Instead, as said before, the measurement was much slower at low frequencies, so the number of averages for these ranges should have to be kept small in order not to take the measure too long in time. For example, with 400 averages, the measurement time in the first range of frequency (from 10 Hz to 100 Hz) could have been 1 hour long. Therefore we decided to divide the spectrum into two parts, in order to have a much higher number of averages for the high frequencies and a suitable number of averages for the low frequencies. We selected 50 averages for the first three ranges (and decades) of frequencies, from 10 Hz to 10 kHz, and 400 averages for the last two ranges, from 10 kHz to 1 MHz.

For each measurement, it was estimated also the background level of RIN, that was plotted together with the RIN of the analyzed laser in order to see if any of the intensity noise peaks were due to the background noise. This background RIN was measured by switching off the laser and leaving the photoreceiver on and connected to the ESA.

5.2.1. DC block

A difficulty that arose during the experiments was the presence of a DC block in the spectrum analyzer input. This component is a capacitor

placed in series with the input signal and acts as a high-pass filter for the coaxial-cable systems; this element was necessary for correct RIN measurements, because it filtered out the direct components of the signals entering in the analyzer that could have caused damage. In particular, without DC block, the analyzer could have presented an overload of intermediate frequency oscillators, causing incorrect experimental measurements. The problem was that this component had cut-frequency around 100 Hz and hence it filtered out the low frequencies from our analyzed RIN spectrum, causing a loss of important information. These low frequencies are important because here we want to observe a flat spectrum with low RIN level, so as the Yb-Er:glass laser could become a suitable ϕ-OTDR source (since it has to measure vibrations that have frequency values located in the range of $10 \div 1000$ Hz).

In order to characterize the DC block we connected a Function/Arbitrary Waveform Generator, 80 MHz made by Agilent to the ESA and we generated a white noise signal. The peak-to-peak amplitude of the noise signal was 300 $\mathrm{mV_{PP}}$, the offset was 200 $\mathrm{mV_{DC}}$ and the V_{ave} measured with the oscilloscope was equal to 0.142 mV. We measured the RIN with and without the DC block at the spectrum analyzer input and, since it was only a comparison, we computed 20 averages for the whole bandwidth. In the Figure 5.1 the two RIN measurements are presented. The high-pass filter behaviour of the DC block can be seen in the graph 5.1b, while, in the graph 5.1a, the DC components are present and we can observe that the RIN level increases significantly at the lowest frequencies.

The cutoff frequency can be calculated as the frequency at which the

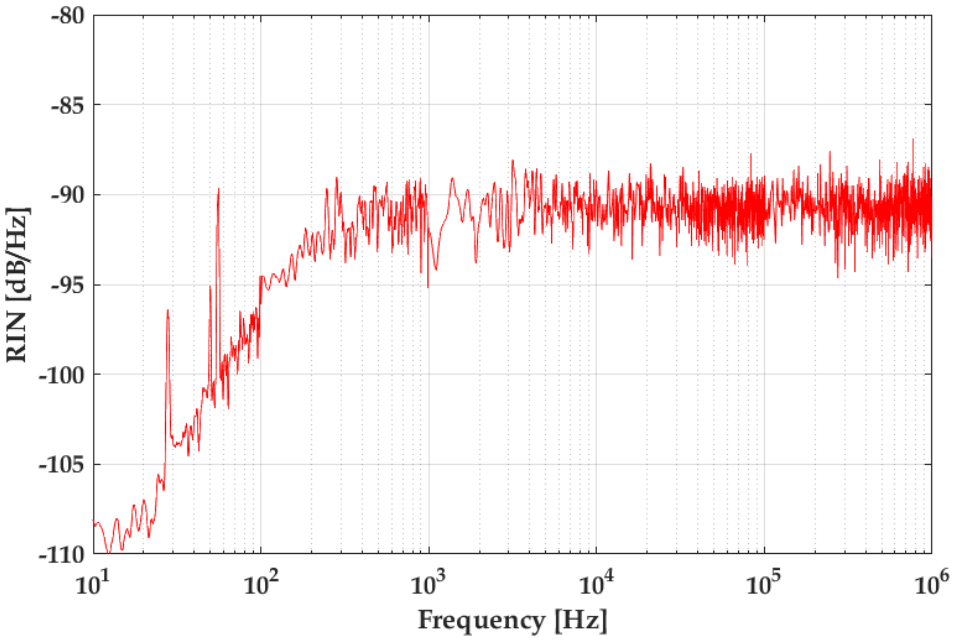

(a)

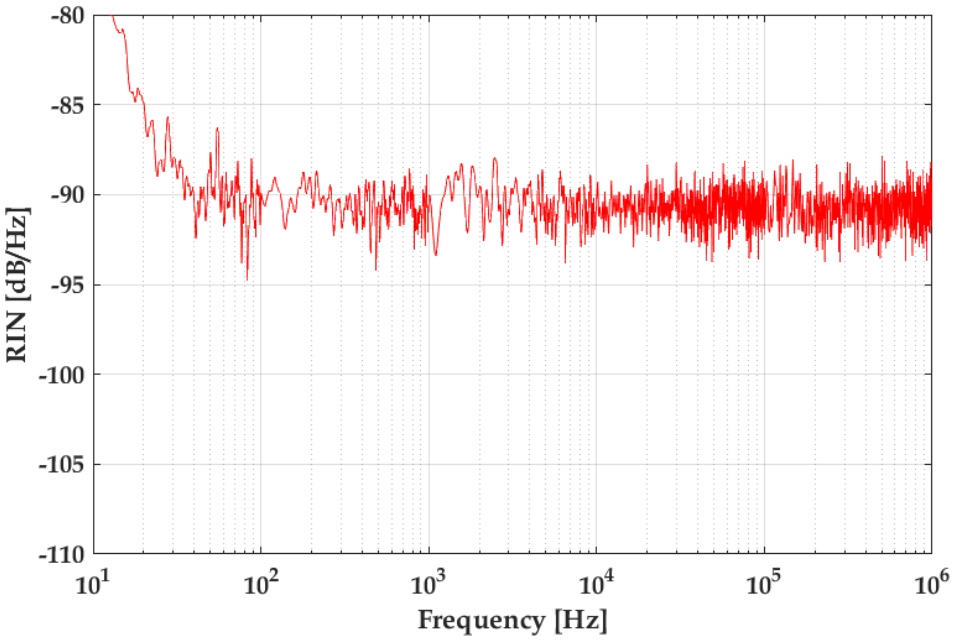

(b)

Figure 5.1: RIN measurements with electrical white noise (generated by the digital function generator) as input signal: a) with the DC block; b) without the DC block.

mean constant value of the noise signal (that should be constant over all the spectrum) decreases by 6 dB(because the RIN is calculated as a power ratio). Having an approximately constant mean value, in the high frequency part of the graph, that is about -90.7 dB/Hz, the point on the x-axis in which the RIN of Figure 5.1a is about -96.7 dB/Hz is $f_C \cong 100$ Hz. Knowing that, we can calculate the capacitance value C of the DC block according to:

$$C = \frac{1}{2\,\pi\,f_C\,R}\,, \tag{5.5}$$

where R is the input impedance of the ESA, which is equal to $50\,\Omega$. C turns out to be about $32\,\mu$F.

Analyzing the RIN of the white noise with the presence of the DC block in Figure 5.1a, we can approximately derive the slope rate from the RIN level at frequencies lower than the cut frequency. The slope is about 15 dB per decade (quite strange value for a first order RC filter). In the filtered region we can see three peaks at 28 Hz, 50 Hz and 56 Hz but we can say that they come from the background noise of the analyzer, as we will see in the next section, in which the background RIN will be illustrated in every measurement with a black line. 28 and 56 Hz peaks are "strange", they were not expected, while the 50 Hz peak is well known.

Using this analysis we extracted a DC block compensation curve that, summed to the RIN measured in the presence of the DC block, could compensate the filtered part of the measurement and let us appreciate

the RIN of the lasers without the attenuation on the low frequencies.

5.3. Numerical Results

As it concerns the RIN measurements on the pump and the Yb-Er:glass lasers, we placed the photoreceiver quite in the center of the beam, checking the voltage with the oscilloscope connected with BNC cables. Since the power was too high, we used some Neutral-Density filters in order to attenuate the power of the lasers without changing their spectral properties. Two ND-filters were available in laboratory: with 10 % transmission and with 1 % transmission.

For what concerns the pump laser, we placed a small cube beamsplitter right after the collimator, in order to perform measurements on the deflected beam of this IR beam without moving the laser diode from its perfectly aligned position as pump for the solid state laser. Then, we placed both the ND filters in series because the beam was collimated and all the power was enough concentrated in a small area, so we needed to reduce significantly the power entering in the sensor area of the photoreceiver.

For the Yb-Er laser, instead, we used only the 10 % ND filter because the beam was diverging and, at a reasonable distance, the power was distributed on a large area with respect to the one of the photodiode, having lower power entering the photoreceiver than in the case of the pump laser.

Using the oscilloscope and the parallel 50 Ω resistance, we checked the

voltage output of the photoreceiver and we tried to set the lasers in order to stay below 1 V, as said in the previous section. In every measurement, once the lasers and the ND filters were stable, we took note of the mean voltage as the V_{ave} parameter that we needed for the matlab code. Then we disconnected the resistance and we connected with BNC cables the electronic spectrum analyzer (with the DC block) to the photoreceiver, in order to start the RIN measurements.

5.3.1. 300 mW Pump Laser Diode

In the Figure 5.2 the RIN measurements on the 300 mW pump laser diode are shown. The red line represents the RIN of the pump laser, the black line represents the background RIN measured switching off the laser. We placed the two ND filters in series, as said before. The pump current was equal to $I_{\text{pump}} = 243mA$, and the V_{ave} measured with the oscilloscope was equal to 635 mV. From 10 Hz to 10 kHz we performed 50 averages and from 10 kHz to 1 MHz we performed 400 averages.

In the Figure 5.2a the RIN of the pump laser without DC block compensation is depicted. We can recognize the filtering behaviour of the DC block that attenuate the signal at low frequencies. Here we can see the peaks, present also in the graph 5.1a in the previous section, at 28, 50 and 56 Hz and we can confirm that they were generated by the background noise. In particular, the 50 Hz peak reaches a RIN level equal to -85 dB/Hz, a large value if we consider that the average value of the pump laser in this case is -103 dB/Hz. There is also another peak, still from the background noise, at 150 Hz ("strange" peak, we could not

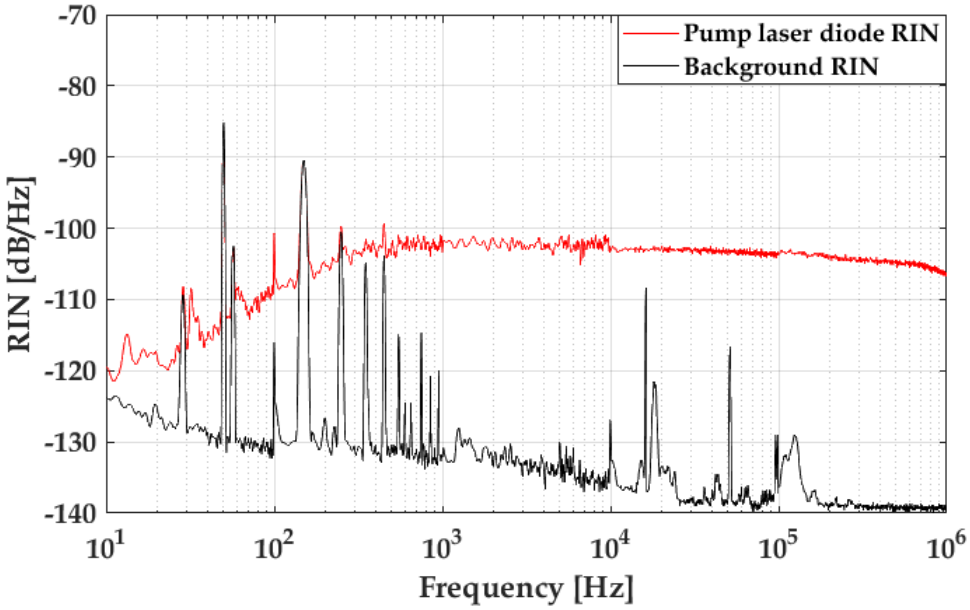

(a)

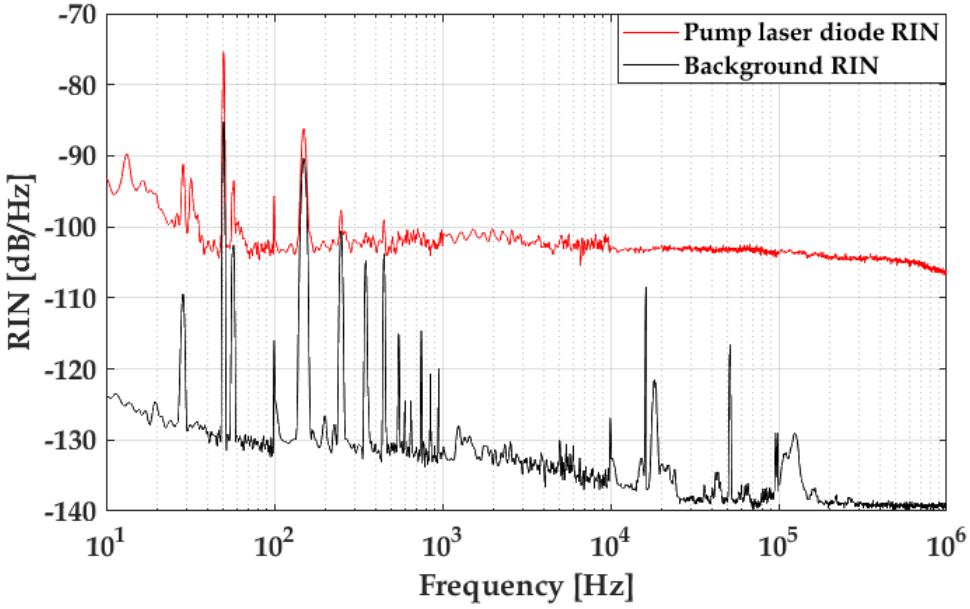

(b)

Figure 5.2: RIN measurements with the 300 mW pump laser as input signal: a) DC block filter not compensated; b) DC block filter compensated.

understand its meaning) that has maximum RIN value equal to -90.5 dB/Hz. At high frequencies instead, the RIN is more or less constant around -103 dB/Hz, as we expected. In the last part of the graph the spectrum level starts to decrease probably because of the filters inside the Electronic Spectrum Analyzer.

In the Figure 5.2b the RIN of the pump laser after the DC block filter compensation is shown. The spectrum becomes more or less flat but the peaks at low frequencies are still present, in particular the two at 50 and 150 Hz, that now reach higher value than before because of the compensation (that is an additional operation).

In general, the compensated spectrum appears much more flat and sufficiently good, since we know that the peaks are generated by the background noise of the instruments and/or of the environment and not by the pump laser analyzed.

5.3.2. Yb-Er:glass Laser

In the Figure 5.3 the RIN measurements on the Yb-Er:glass laser are shown. The red line represents the RIN of the laser, the black line represents the background RIN. We placed only the 10 % ND filter (for the reason explained previously), the pump current was equal to $I_{\text{pump}} = 243mA$, and the V_{ave} measured with the oscilloscope was equal to 384 mV. As for the pump laser, from 10 Hz to 10 kHz we performed 50 averages and from 10 kHz to 1 MHz we performed 400 averages.

In the Figure 5.3a the RIN of the Yb-Er laser without DC block com-

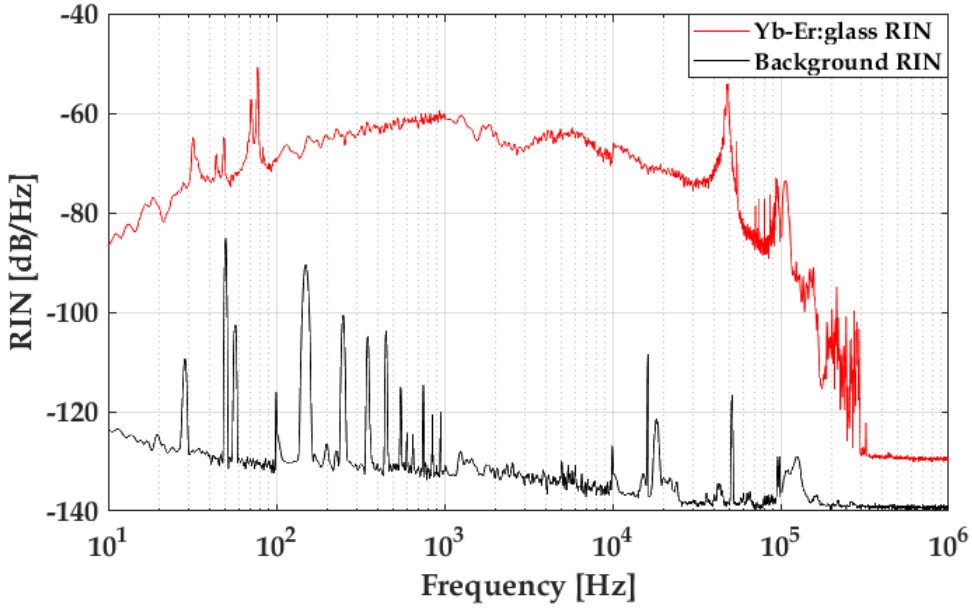

(a)

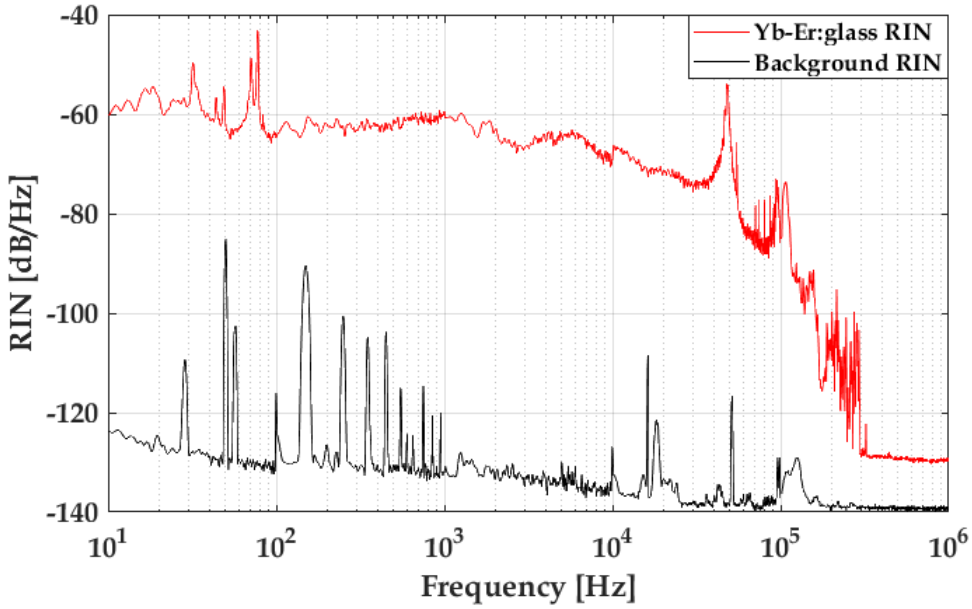

(b)

Figure 5.3: RIN measurements with the 300 mW pump laser as input signal: a) DC block filter not compensated; b) DC block filter compensated.

pensation is depicted. As before, we can recognize the filtering behaviour of the DC block that attenuate the signal at low frequencies. Here, the peaks in the background noise (black line) are obviously still present, but their RIN levels are too small with respect to the laser RIN and they don't affect the laser RIN measurement. The spectrum presents new peaks at 70 Hz and 78 Hz with very high RIN values that are definitely non-ideal. Increasing the frequency, the RIN fluctuates around $\cong -70$ dB/Hz until the relaxation oscillations peak at 48 kHz, where the maximum level is about -55 dB/Hz, a quite high value but lower than the peaks at low frequency. After this peak, the spectrum starts to fall off with slope $\cong -60$ dB/Hz per decade until -130 dB/Hz, as expected, but showing unusual fluctuations and peaks.

In the Figure 5.3b the RIN of the Yb-Er laser after the DC block filter compensation is shown. The spectrum become more or less flat before 1 kHz but the peaks at low frequencies are still present and now reach higher values than before because of the compensation.

In the Figure 5.4 the compensated RIN of the two lasers are represented in the same graph. The red line represents the Yb-Er:glass laser RIN, the blue line represents the 300 mW pump laser RIN, while the black line represents the background RIN.

In general, the compensated spectrum of the Yb-Er laser appeared not so good and it was definitely necessary a solution for the RIN reduction and the relaxation oscillations peak suppression (treated in the next section). In the case of lasers with direct pumping, such as in our case, the intensity

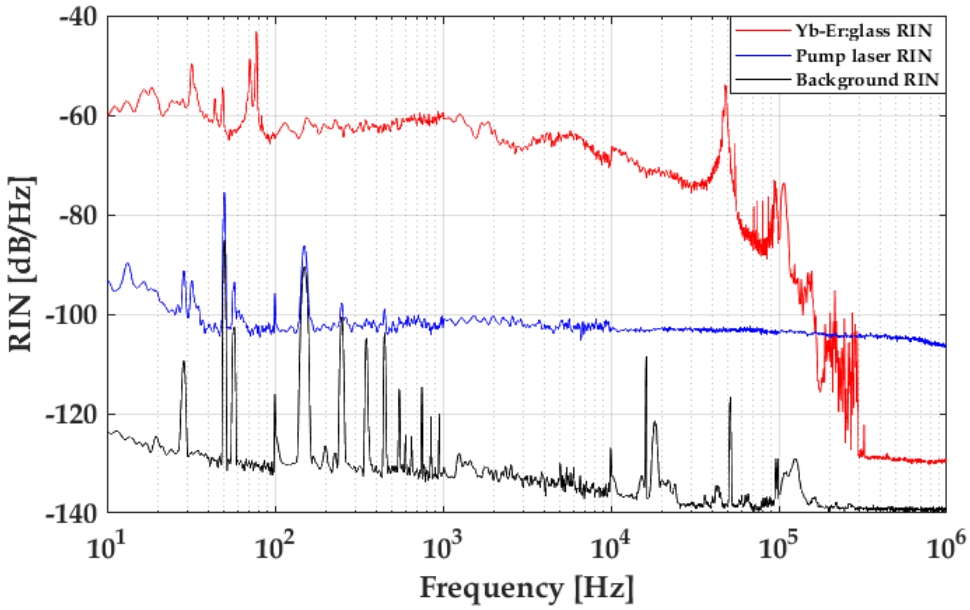

Figure 5.4: RIN measurments on the 300 mW pump laser and on the Yb-Er:glass laser with background. DC block filter compensated.

noise is mainly induced by pump power fluctuations. Conversely, in [22] it was demonstrated that in a codoped system, such as the Yb–Er laser, the main contribution to the RIN is the intrinsic spurious modulation of cavity losses [21]. Infact, from the RIN measurements previously presented it can be seen that the pump RIN does not affect the RIN of the solid state laser.

5.4. Future Developments

In this section, future developments for the improvement of the stability and the noise reduction of the Yb-Er:glass laser are presented.

5.4.1. Intensity Noise Reduction by Non-linear Absorber

An interesting solution for noise reduction consists in inserting an optical non-linear absorber inside the laser cavity. This has been proved to be very effective in reducing the intensity noise around the relaxation oscillations (RO) frequency using the process of two-photon absorption (TPA) in Yb-Er: glass laser [23]. When inserted into the laser cavity, TPA induces losses which are proportional to the local intensity, leading to a significant reduction of the intensity fluctuations exactly where they are stranger. It has been shown in [7] that an example of a non-linear absorber could be a silica (Si) plate inserted into the laser cavity in order to induce the desired intensity dependent losses through two-photon absorption. Moreover, this Si plate can be left uncoated to act as an intracavity etalon enabling the laser to be single-longitudinal mode, or it can be tilted at the Brewster angle to ensure single-polarization [6].

The Figure 5.5, taken from [7], reproduces two RIN spectra recorded for two different situations: without (1, blue line) and with (2, red line) the silica plate (of 40 µm thickness) into the laser. The RIN spectrum (1) exhibits a strong RO peak at about 40 kHz (considering a 49 mm cavity length). By contrast, the RIN spectrum (2) shows that the insertion of the nonlinear absorber close to the active medium, i.e. where the laser photons density is higher (depending also on the thermal lensing effect), leads to 33 dB reduction on the amplitude of the RO peak and the RO frequency ,once suppressed, shifts toward high frequencies (due

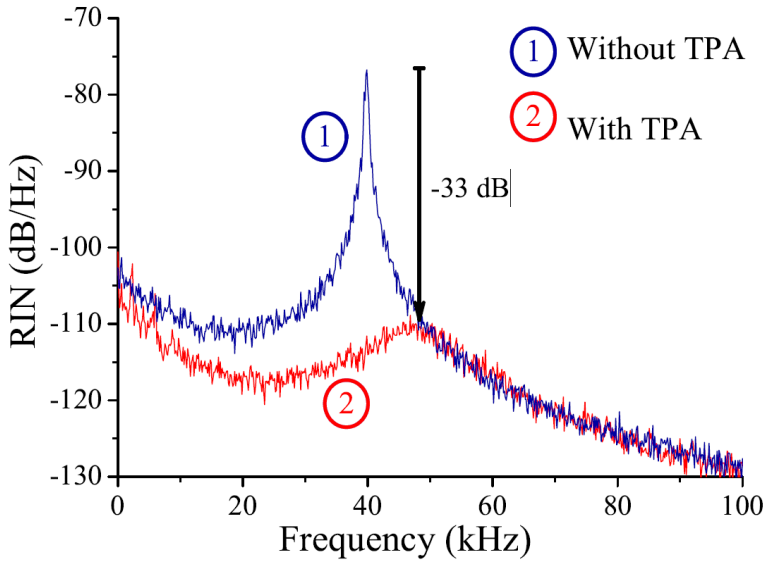

Figure 5.5: RIN spectra of the laser without and with an intracavity two-photon absorber (Silica plate).From [7].

to increased losses) although the pumping rate is unchanged.

The silica plate can be translated along the optical axis of the resonator in order to change the photon density within it. If the Si plate is close to the output mirror, that is where the laser beam is sufficiently wide, meaning a much lower photon density, the TPA effect becomes less effective. Otherwise, increasing the photon density in the Si plate (moving towards the active medium), while keeping a constant pumping rate, leads to a reduction of the laser intensity noise, but also to an increase of the relaxation oscillations frequency.

A more efficient solution was then found replacing the silica plate with a gallium arsenide (GaAs) plate, which leads not only to a significant amplitude reduction of the relaxation oscillations peak, but also without any frequency shift [7, 24].

5.4.2. Compact and Monolithic Laser Design

Although most solid-state lasers consist of a number of discrete elements (i.e. of a laser crystal or glass host, some laser mirrors, and possibly additional intracavity optical elements), there are some types of lasers which are monolithic. For monolithic lasers according to a strict definition, the whole laser resonator consists only of some "solid" pieces of crystal or glass without air gaps between optical elements. The resonator is then closed either with dielectric mirror coatings on the surfaces of the solid material (typically a glass or a crystal), or by using total internal reflection. Additional optical elements and useful components can be added within the laser resonator, provided that these elements are rigidly attached (glued or optically bonded) to the gain medium.

It has been demonstrated in [18], that the results, especially in terms of laser stability, for monolithic lasers are much better than for the same cavities with separate mirrors. The peak laser power was almost two times higher while the threshold pump power was significantly decreased. The laser cavity was made of a 2.5 mm long active rod with one plane and one concave spherical face, both faces being coated by multilayer coatings to form the resonator ends and pumped by a fiber-coupled 980 nm. Additionally, a monolithic cavity ensures higher stability with respect to mechanical vibration and thermal deformation of the resonator and the alignment of the laser is much easily achievable [25]. In fact, a compact monolithic cavity helps to overcome problems arising from mechanical vibrations, and, in particular, to reduce the relative intensity

noise (RIN) induced by external perturbations [24] and also frequency noise of the generated laser light.

Conclusions

In this thesis, the construction and the characterization of a Yb-Er:glass laser are exposed. This laser presents a great interest as a possible source for ϕ-OTDR system, as it has very good short-term wavelength stability and possibility of wavelength tuning. For this reason, its main characteristics were investigated in order to find the adequate laser structure, achieving the accuracy requirements for ϕ-OTDR. In particular, we studied the behaviour of the laser in terms of: output power vs. pump power characteristic, cavity length in different conditions, beam waist spot size and position, thermal lensing effect and relative intensity noise (RIN).

Firstly, we studied every single component of the laser structure together with the power meters used for the laser measurements. The responsivity of the power meters was measured and presented. Then, we performed experimental estimations on the pump laser diodes available, in order to find the best and most stable one. Once investigated and selected the pump laser, we proceeded to the construction of the solid state laser, with the precise alignment of every component thanks to a He-Ne laser. The Yb-Er:glass laser was switched on and its output power was maximized thanks to micrometric translations of its most important components. At this point we estimated the stability of the laser varying its cavity

length and pump power, provided by the laser diode. The Knife-Edge technique was presented and used for the beam spot size of the beam waist measurements, from which we revealed a thermal lensing effect in the active material.

In the end, the Relative Intensity Noise of the pump laser diode and the solid state laser was measured, comparing the results and discussing the spectra obtained.

A future development for a better stability of the Yb-Er:glass laser could be a monolithic structure, in which the whole laser resonator consists only of some "solid" pieces of crystal or glass without air gaps between optical elements. In this way, the stability could improve together with the peak power and the threshold pump power (that could decrease significantly).

A development for amplitude noise reduction is the insertion of a non-linear absorber in the resonant cavity. This has been proved to be very effective in reducing the intensity noise around the relaxation oscillations frequency using the process of two-photon absorption (TPA) in Yb-Er:glass laser. When inserted into the laser cavity, TPA induces losses which are proportional to the local intensity, leading to a significant reduction of the intensity fluctuations. An example of a non-linear absorber could be the silica (Si), but a more efficient solution could be found with a gallium arsenide (GaAs) plate, which leads to a significant amplitude reduction of the relaxation oscillations peak also without any frequency shift.

Bibliography

[1] Andrei Zhirnov, Alexey Pniov, C. Svelto, Michele Norgia, A. Pesatori, Gianluca Galzerano, P Laporta, Dmitriy Shelestov, and V.E. Karasik. Er:yb phosphate glass laser with nonlinear absorber for phase-sensitive optical time domain reflectometry. *Journal of Physics: Conference Series*, 917, 11 2017.

[2] Dr. Rüdiger Paschotta. Erbium-doped laser gain media, encyclopedia of laser physics and technology, 2008. URL `https://www.rp-photonics.com/erbium_doped_laser_gain_media.html`.

[3] Seppo Honkanen, Tomoko Ohtsuki, Shibin Jiang, S. Iraj Najafi, and Nasser Peyghambarian. High er concentration phosphate glasses for planar waveguide amplifiers. *Proc. SPIE 2996*, 1997.

[4] Marcos Araújo, Rubens Silva, Emerson Lima, Daniel Pereira, and Paulo De Oliveira. Measurement of gaussian laser beam radius using the knife-edge technique: Improvement on data analysis. *Applied optics*, 48:393–6, 02 2009.

[5] Sidney A. Self. Focusing of spherical gaussian beams. *Applied optics*, 1983.

[6] Yuri Iaconi and Emil Softic. *Pump and Laser Mode-Matching under*

Thermal Lensing in the Yb,Er:glass Laser: Study and Optimization. 2020.

[7] Abdelkrim El Amili, Gaël Kervella, and Mehdi Alouini. Experimental evidence and theoretical modeling of two-photon absorption dynamics in the reduction of intensity noise of solid-state er:yb lasers. *Optics Express*, 21(7):8773, apr 2013.

[8] Dr. Rüdiger Paschotta. Eye-safe lasers, encyclopedia of laser physics and technology, 2008. URL `https://www.rp-photonics.com/eye_safe_lasers.html`.

[9] M. Gold. Design of a long-range single-mode otdr. *Journal of Lightwave Technology*, 3(1):39–46, 1985.

[10] Zhihong Huang, James E. Carey, Mingguo Liu, Xiangyi Guo, Eric Mazur, and Joe C. Campbell. Microstructured silicon photodetector. *Applied Physics Letters*, 89(3), 2006.

[11] Dr. Rüdiger Paschotta. Responsivity, encyclopedia of laser physics and technology, 2008. URL `https://www.rp-photonics.com/responsivity.html`.

[12] Orlov, Sergej, Huber, Christian, Marchenko, Pavel, Banzer, Peter, Leuchs, and Gerd. Toward a corrected knife-edge-based reconstruction of tightly focused higher order beams. *Frontiers in Physics*, 8, 2020.

[13] Melles Griot. *Historic CVI Melles Griot Technical Guide.* Melles Griot, 2009.

[14] Francis A. Jenkins and Harvey Elliott White. *Fundamentals of optics / by Francis A. Jenkins and Harvey E. White.* McGraw-Hill New York, 2nd ed. edition, 1957.

[15] Orazio Svelto. *Principles of lasers.* Springer Nature, 5th edition, 2010.

[16] Y.-F. Chen. Design criteria for concentration optimization in scaling diode end-pumped lasers to high powers: influence of thermal fracture. *IEEE Journal of Quantum Electronics*, 35(2):234–239, 1999.

[17] Mladen Franko and Chieu Tran. *Thermal Lens Spectroscopy.* 03 2010.

[18] Stefano Taccheo, Paolo Laporta, Stefano Longhi, Orazio Svelto, and Cesare Svelto. Diode-pumped bulk erbium-ytterbium lasers. *Applied Physics B*, 63, 1996.

[19] D. McCumber. Intensity fluctuations in the output of laser oscillators. *IEEE Journal of Quantum Electronics*, 2(8):219–221, 1966.

[20] Toptica Eagleyard. Relative intensity noise of distributed feedback laser, application notes, 2008. URL `https://www.toptica-eagleyard.com`.

[21] Cesare Svelto, Stefano Taccheo, Elio Bava, and Paolo Laporta. Characterization of Yb-Er:glass lasers at 1.5 μm wavelength in terms of amplitude and frequency stability. *Measurements*, 26(2):119–128, January 1999.

[22] S. Taccheo, P. Laporta, O. Svelto, and G. de Geronimo. Theoretical

and experimental analysis of intensity noise in a codoped erbium-ytterbium glass laser. *Applied Physics B: Lasers and Optics*, 66(1): 19–26, January 1998.

[23] R. van Leeuwen, B. Xu, L. S. Watkins, Q. Wang, and C. Ghosh. Low noise high power ultra-stable diode pumped Er-Yb phosphate glass laser. In Michael J. Hayduk, Peter J. Delfyett Jr., Andrew R. Pirich, and Eric J. Donkor, editors, *Enabling Photonics Technologies for Defense, Security, and Aerospace Applications IV*, volume 6975, pages 144 – 152. International Society for Optics and Photonics, SPIE, 2008.

[24] T V Choban, A A Zhirnov, A O Chernutsky, K V Stepanov, A B Pniov, G Galzerano, V E Karasik, and C Svelto. ϕ-OTDR based on tunable yb-er:phosphate-glass laser. *Journal of Physics: Conference Series*, 1410(1):012108, dec 2019.

[25] Jaroslaw Mlynczak and Nabil Belghachem. Monolithic thermally bonded $er3+, yb3+ : glass/co2+ : mgal2o4$ microchip lasers. *Optics Communications*, 356, 12 2015.